Investigation of Plating Process Variability and Mechanism for Oxide Disruption in a Ni-Modified Fluxless Brazing Process for Aluminum Alloys

by

Colin Andrew Tadgell

A thesis
presented to the University of Waterloo
in the fulfillment of the
thesis requirement for the degree of
Master of Applied Science
in
Mechanical Engineering

Waterloo, Ontario, Canada, 2014

Author’s Declaration

I hereby declare that I am the sole author of this thesis. This is a true copy of the thesis, including any required final revisions, as accepted by my examiners.

I understand that my thesis may be made electronically available to the public.

Abstract

Dana Canada Corporation (DCC) have been innovative leaders in the design and processing of automotive components for over a century. A long standing method of achieving high quality aluminum brazed heat exchanger products is through its patented fluxless nickel brazing process.

Some of the lightest structural metals available to the automotive industry presently are aluminum alloys offering high thermal conductivity and excellent corrosion resistance. A major application of aluminum in automotive component manufacturing is in stacked channel heat exchangers used in fluid and emissions cooling. The use of aluminum alloys have allowed for more lightweight and, as a result, more fuel efficient vehicles.

These heat exchangers are commonly joined through brazing of a lower melting clad aluminum alloy which is applied over a structural core aluminum alloy with desired mechanical properties. A well-documented issue in the brazing process is the presence of an aluminum oxide and its effect on wetting of the molten clad surface. Commonly, the use of NOCOLOK® ($KAlF_6$, $KAlF_4$) flux in Controlled Atmosphere (CAB) furnace brazing, or Magnesium alloy additions in conventional Vacuum aluminum, are used to overcome this problem. A limitation with these traditional methods lies in the byproducts of the flux process, namely residual flux remaining on the surfaces of the parts being brazed; and higher process sensitivity and cost associated with vacuum aluminum brazing.

Dana Canada Corporation has developed a Ni-modified fluxless brazing process that has good operational robustness, while avoiding the problems associated with traditional fluoride salt fluxes, or magnesium getters in the case of vacuum aluminum brazing. This method ensures the mechanical perforation of the oxide prior to the desired brazing temperatures and ensures a strong coherent bond following the brazing process. The thermal and physical phenomena occurring at the aluminum braze sheet surface during brazing have been studied in work by Cheadle et. al [5] and Corbin et. al [30, 36, 67], however the effect of the plating process variation on resultant phenomena as well as oxide behavior at the metal/oxide interface have not.

For the purposes of confidentiality, the plating process variation is undisclosed. The effect of this process variation was the area of initial study for this thesis on the material melting and solidification braze kinetics. This was studied using a combination of microstructural and thermal analysis techniques.

Overall behavior of aluminum oxide during brazing of Ni-modified sheets was examined as well. The mechanism of disruption of this oxide is still not understood, though it has been speculated. Various methods of oxide growth and different oxide structures were grown on the Al surface of automotive braze sheets. Initial characterization of the near

surface oxide present on these aluminum alloy sheets was conducted using SEM, FTIR, and TEM. Nickel was sputtered onto the surface and they were subsequently examined using Optical microscopy, Differential Scanning Calorimetry (DSC) and SEM.

This research focused on two aspects: 1) The effect of plating process variability associated with deposition of the Ni layer on subsequent brazing and 2) the oxide disruption process during brazing. Both aspects of the research were studied using a combination of microstructural and thermal analysis techniques. For the oxide disruption research, various oxide thicknesses and structures were grown on the surface of the automotive braze sheet, sputtered with a Ni layer and examined using optical and electron microscopy and Differential Scanning Calorimetry.

Acknowledgments

I would like to express my deepest thanks to my research supervisor, Dr. Mary Wells, and industrial supervisors; Dr. Sooky Winkler, and Dr. Leo Colley for their guidance and support during this research project. I can think of no better people to help me land my academic footing. I would like to thank Dr. Wells for her constant enthusiasm, unwavering support, and dedication to seeing me succeed. Without Dr. Winkler I would not have even known of this opportunity, her constructive criticism and insight have helped me become a more organized, focused researcher. Thank you finally to Dr. Colley for your mentorship and for making me ask the right questions.

I am grateful to Dana Canada Corporation for seeing me through two fascinating and challenging research projects. In particular, I would like to thank Brian Cheadle for organizing this project, Feng Liang for his wealth of knowledge in science and chemistry, and Evelyn Lazo for her support in the lab during my time at Dana.

I would like to thank all those who supported me at the University of Waterloo, especially Mark Whitney whose expertise and knowhow helped me countless times throughout these last two years. I am also grateful for the company and support I received working with Dr. Massimo DiCano and Dr. Etienne Caron. Many thanks to the G2N facility, especially Dr. Richard Barber and Alireza Tari, for use of their sputtering and characterization equipment. The help and support I received from Dr. Stephen Corbin and his group was instrumental in some of my final conclusions and I would like to thank them as well.

Finally, I am thankful for the support from my family and friends who have helped me so much over the years. A special thanks to my parents Brenda and Scott, my sister Anne, my brother Eric, and my girlfriend Jen. You never questioned my dreams but only strengthened my beliefs.

“What is now proved was once only imagined.”

- **William Blake**

Table of Contents

List of Figures

List of Tables

1.0 Introduction

Over the past few decades, the desire for a more lightweight, energy efficient automobile has become apparent. Through the use of lighter metals in areas such as the frame, body, and internal components, improvements have been made to fuel economy and overall emissions [1]. One such improvement lies in the use of aluminum alloys for heat exchangers in automotive components. Aluminum is lightweight, easily formable, and offers an excellent thermal conductivity for this application [2].

1.1 Brazing Sheets and Practical Use in Automotive Applications

Aluminum alloys are widely used for heat exchange devices in automotive applications due to their low density, good thermal conductivity and, finally, sufficient mechanical strength and corrosion resistance [3]. The primary method to manufacture automotive heat exchangers, such as engine and transmission oil coolers, is through furnace brazing of a stacked assembly of multi-layered aluminum sheet.

In the case of automotive furnace brazing, each individual Al braze sheet is a multilayered structure consisting of a core and clad. Typically the clad is on one or both sides of the braze sheet surface and consists of an Al-Si alloy at or below the eutectic composition of 12.6 wt% Si (e.g. AA 4343, AA 4045, AA 4047). The core is usually an alloy with an Al-Mn composition (e.g. AA 3003). Owing to its composition (i.e. a higher Si content), the clad has a lower melting temperature than the core of the sheet [6].

The manufacture of these braze sheets is done through roll bonding of a clad ‘sandwiched’ 3XXX series core. This process creates new surface area through tension in the rolling direction, which exposes the underlying surface metal as aluminum oxide is fractured. Fragmented oxide, as a result of the rolling process, is commonly found embedded further in from the near surface microstructure [7][8].

DC casting methods are used for the manufacture of 3XXX and 4XXX ingots, after which, the ingots are individually hot rolled to their respective percentage of the gauge thickness. They are then layered together and hot rolled again. These two hot rolling stages allow diffusion of constituents and ordering to form stable dispersoids. This also allows proper dispersion of silicon in the clad layer, which improves liquid mobility upon melting [9]. From here a combination of cold rolling and intermediate annealing (600-690K) are used to reach the desired thicknesses and temper [10][11].

1.2 Brazing Process for Heat Exchanger Manufacture

The most common application of brazing of aluminum alloy sheets in automotive technology is for manufacturing heat exchangers, such as radiators or oil coolers. Typical construction of these heat exchangers is through the assembly of tube, or plate, and fin based components, seen in Figure 1.1. This diagram shows the process before and after the brazing of aluminum braze sheet. A typical braze sheet consists of a core layer and clad layer. The core layer determines the desired mechanical properties of the entire braze sheet as it comprises 80-90% of the entire thickness [14]. The clad layer is a modified layer which is alloyed so that it melts at a lower temperature than the core. This allows the clad layer to melt in a braze process while the core remains intact.

Heat exchanger braze sheet is usually comprised of a 3XXX series aluminum alloy core and a 4XXX series clad layer. This arrangement can be single sided or double sided depending on the required geometry. A typical combination for a double side sheet would be 4343/3003/4343 or 4045/3003/4045 [14][15]. The core material is alloyed with additions of copper and manganese for strength, hardness, and corrosion resistance. The clad layer is predominantly aluminum and silicon. Additions of silicon lower the melting point of the alloy and improve wettability of molten clad [12][15].

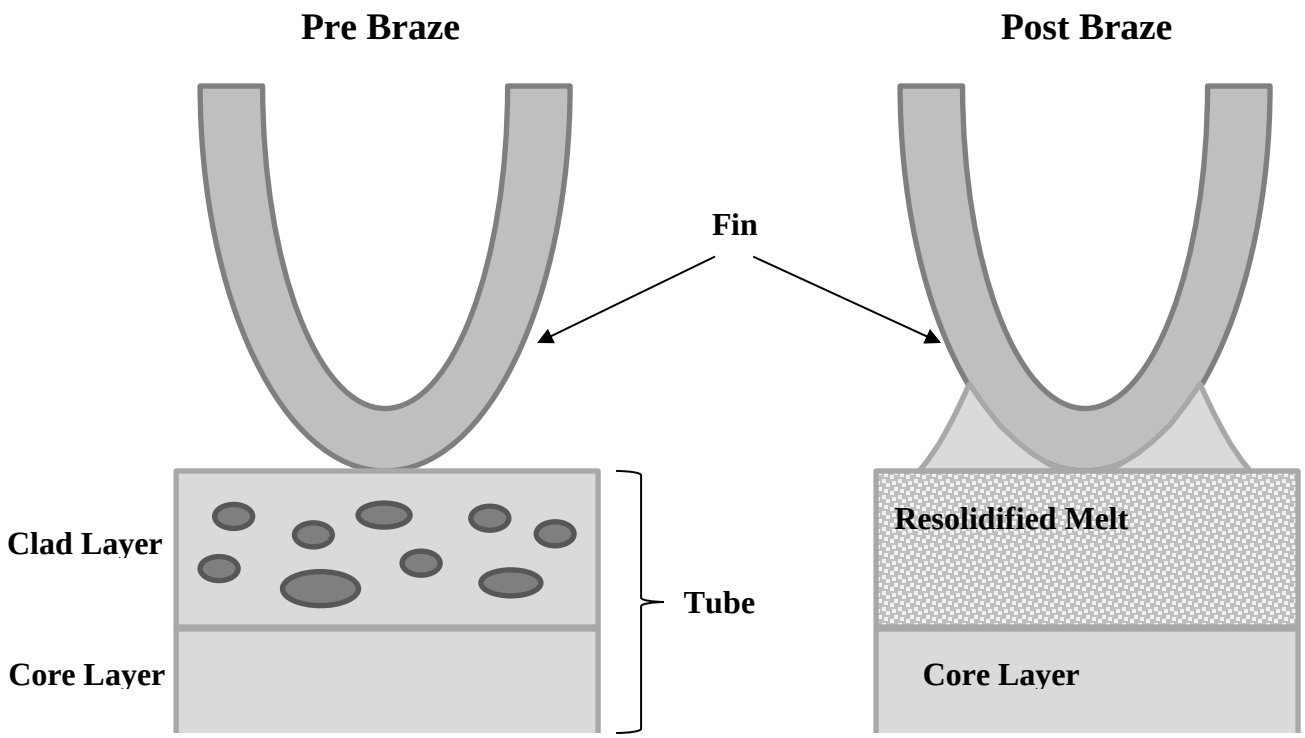

Figure 1-1 - Braze Sheet Cross Section and Resultant Microstructure Before (left) and After (right) Brazing

Aluminum naturally passivates in open air forming an ever present oxide layer. This oxide layer protects the metal from corrosive environments by acting as a barrier between the two. This oxide also acts as a barrier to wetting [15][17]. Aluminum oxide will behave like an outer skin upon melting of the clad layer; this can be viewed from the surface under a hot stage microscope (See Figure 1.2).

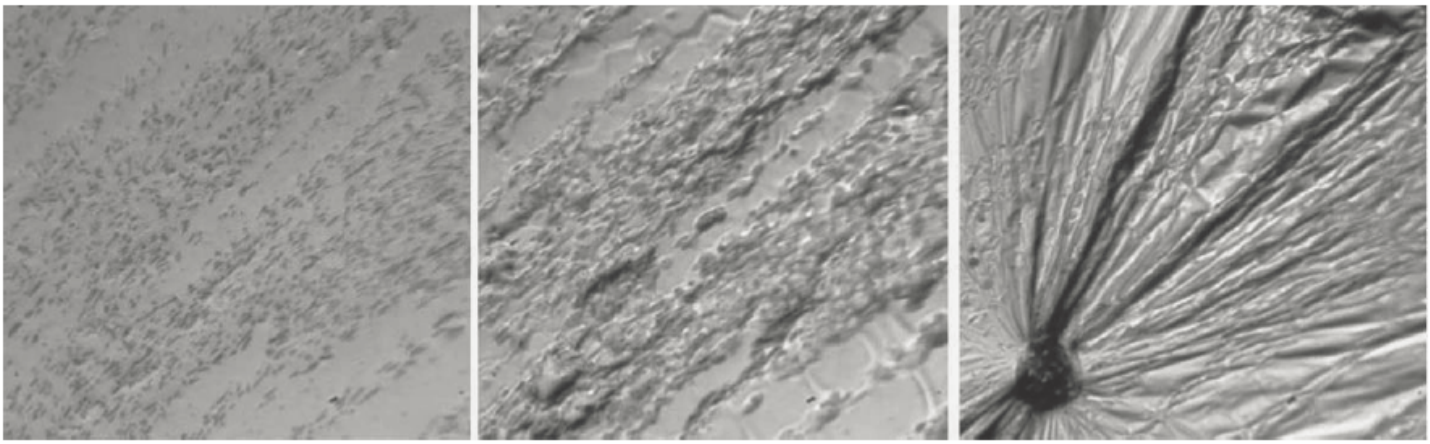

Figure 1-2 - Hot Stage Microscope Overview Imaging of Aluminum Alloy 4343 Approaching and During Melting [15]

Therefore, it is necessary to remove this oxide layer at areas of joining prior to brazing. One method is via conventional flux brazing methods which uses inorganic $KAlF_6$ compounds to chemically remove the oxide layer before melting of the clad. Flux brazing, which uses a Controlled Atmosphere Brazing (CAB) furnace, is rapid; but is limited in terms of cleanliness due to flux residues and requires added initial capital investment for the application of flux and management of the flux particles for operator health and safety. Another method would be via vacuum brazing, which utilizes Al braze sheet materials with magnesium additions in a high vacuum environment to disrupt the oxide layer. This fluxless process is clean (no residues), but is slow and more expensive due to high energy costs. A third and perhaps more attractive method, is via Dana's proprietary fluxless brazing process. This process utilizes an electrolytically deposited Ni-based braze promoter that reacts exothermically with Al to disrupt the oxide layer during brazing in a CAB furnace. In comparison to traditional flux and vacuum brazing processes, Dana's fluxless brazing technology is capable of producing parts that are both clean and at high throughputs in a cost effective manner [5][14][15][16].

Ni-promoted brazing, is a process developed and used by Dana Canada Corporation (DANA) [4][5]. In this process the clad sheet is coated with a Ni braze promoter. During heating, the Ni plating initiates an exothermic reaction with the aluminum substrate which breaks down the oxide layer, allowing molten filler metal-to-metal contact. However, key scientific questions still remain to achieve improved fluxless brazing including: how the oxide becomes destabilized and the influence of plating variability on the melting and solidification kinetics operative in this class of furnace brazing, which is the primary subject of study of this thesis. Use of a modified nickel layer as a method of fluxless brazing has been a patented process of Dana Canada Corporation and in commercial use for several decades [12]. This technique avoids the use of typical industrial fluxes (such as potassium floroaluminate) or additions of unnecessary constituents (such as magnesium additions in fluxless brazing) [13][14]. Dana's proprietary modified nickel layer functions as a braze promoter. It disrupts the naturally occurring aluminum oxide layer on the Al braze sheet surface and promotes wetting and flow of the molten filler metal into the surfaces to be joined via capillary action during brazing [15][16].

1.3 Problem Statement and Objectives

The work presented in this thesis is part of an ongoing research and development project initiated by Dana Canada Corporation involving faculty from both the University of Waterloo and Dalhousie. The primary objective of the overall project is to understand i) the oxide disruption mechanism as it relates to oxide and nickel thickness, and also the presence of surface silicon, and ii) the influence of varying plating process parameters on the melting and solidification kinetics of Al braze sheets in Dana's proprietary fluxless nickel brazing process

To achieve these goals, extensive testing was conducted in characterizing the braze sheets and in simulating the braze cycles which they typically are exposed to. Single side clad 4045/3003 Al braze sheets with various electrolytically deposited Ni braze promoter on the clad surface which was provided by Dana. For reasons of confidentiality, these sheets were labelled simply as A, B, and C. Small discs were punched from different locations on these sheets and run through different thermal cycles using Differential Scanning Calorimetry (DSC). DSC is a thermal measurement technique which allows monitoring of the heat flow of a sample. The sample is put through different thermal cycles, and events such as melting, intermetallic/phase formation, and solidification can be monitored and measured. Thermal cycles of interest included typical CAB heating, isothermal holds, halted testing to examine the interaction of the clad/nickel interface, and cyclic testing to investigate isothermal diffusion of the liquid layer.

Specimens run through DSC were then examined using optical and scanning electron microscopy (SEM). Using energy dispersive x-ray spectroscopy, various phases formed from aluminum, nickel, and silicon were documented. SEM imaging of the surface of the braze sheets was also taken before and after DSC testing to differentiate samples A, B, and C.

Following thermal and microstructural characterization of the process variations, a method for better understanding the surface aluminum oxide layer was formulated. Initial testing involved increasing the overall knowledge of the oxide layer and what layers could be

grown. Emphasis for the grown oxides was on creating oxides that simulated the natural oxide forming on a typical brazing sheet but at increased thickness values to attempt to provide a discriminating ability to test oxide disruption by Ni during brazing. Methods for growth included chemical, thermal, and electrochemical. The samples used in the oxide growth experiments were similar to the brazing sheet used to create samples A, B, and C.

Initial characterization of the oxide layer was conducted using Focused Ion Beam Scanning Electron Microscopy (FIB-SEM) and Chem-SEM. FIB-SEM allowed a cross section to be cut out from a sample using a focused ion beam. This had the advantage of avoiding any damage that might occur to the oxide through other sample preparations. Chem-SEM provided measurement of oxide ratios and provided sample compositions as a result of the oxide growth experiments. From this, a correlation curve was created which allowed direct comparison of the Chem-SEM oxygen concentrations to direct FIB-SEM/TEM results.

Following this work, an experimental design was created that would examine the effect that different oxides would have on the nickel layer reaction. For this study, nickel of varying thicknesses was deposited onto specially prepared Al braze sheets with laboratory grown oxide layers using sputtering equipment available at the G2N facilities at the University of Waterloo. The sputtered nickel samples were then characterized using DSC, Optical, and SEM techniques.

2.0 Literature Review

2.1 Brazing Process

Brazing is a process where a filler metal is heated above its melting temperature and allowed to solidify into a joint between other metals. It is predominantly controlled through the use of alloying and diffusion. It differs from soldering by the higher melting temperatures (above 450°C) of the filler metal. Often in brazing a flux is used to help remove the surface oxide from the parent materials and ensure a strong metallurgical bond is formed between the parent material and braze material. The filler metal is heated above its melting temperature whilst in a protective environment (typically through use of a flux or controlled atmosphere) to provide the best conditions for brazing [18].

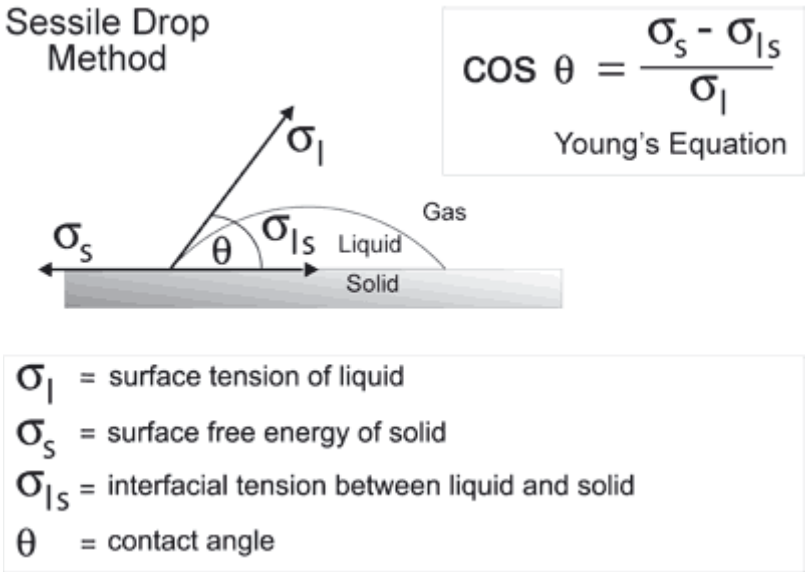

Figure 2-1 - Sessile Drop Method and Young's Equation [18]

Key parameters in the brazing process involve surface energy and tension. These properties can be illustrated in the sessile drop experiment (shown in Figure 2.1) where knowledge of the surface energy of the liquid in atmosphere (σ_l) and the surface of the metal to the atmosphere (σ_s) can be used to find the relative surface energy between the liquid and solid. In a similar way, the filler metal is liquid and 'wets' on the surface of the metal to be joined. The contact angle of the droplet on the surface indicates the wettability of the liquid, where $\theta<90^o$ indicates wetting of the liquid on the surface. Wetting can be improved by decreasing θ through proper selection and alloying of the filler metal and solid,

removal of aluminum oxide, dust and water from the surface, and control of pressure and temperature in the process [18].

An important effect in brazing joint formation is capillary action in pulling molten clad into the joint cavity. This helps ensure that no voids, or gaps, are present and that the joints remain liquid/gas tight while under heavy pressures. This drawing action phenomenon is the result of two combative forces; the adhesive forces of molten clad to the surface of the joint and the cohesive forces felt within the clad itself. Common factors affecting capillary forces are the mutual surface tensions of the base metal, molten clad, flux, and the present atmosphere, in addition there are other dynamic considerations such as viscosity, vapor pressure, and metallurgical reactions between the base/filler metal [15][19].

Common methods of brazing include torch brazing, vacuum brazing, and controlled atmosphere brazing (CAB). For creating high performance aluminum brazed components for use in the automotive and aerospace industry, either a CAB or vacuum process is typically used. These two important furnace brazing processes can be distinguished by the method used to destabilize the surface oxide layer from the braze sheet. In the so-called NOCOLOK^{TM} [6] or CAB [20] process the clad sheets are heated within a controlled atmosphere (usually high purity N_2) in the presence of a flux. The flux is an inorganic compound of $KAlF_6$. The role of the flux is to dissolve or destabilize the oxide layer and allow the molten filler, or clad, metal-to-metal contact.

Vacuum brazing involves getter alloy additions in the clad and core in the presence of a low vacuum (~$3x10^{-5}$ Torr). The most commonly used getter addition is magnesium in concentrations ranging from 0.25-1.5 wt% in the clad layer. During heat up, magnesium migrates to the surface of the oxide and forms either MgO crystallites, or a spinel form $MgAl_2O_4$ (see Figure 2.2). These precipitates continue to grow to some critical size which disrupts the oxide and allows for molten clad flow. Typically vacuum brazing is conducted in a batch, or semi continuous furnace which can make it less than ideal for high volume production. [21]

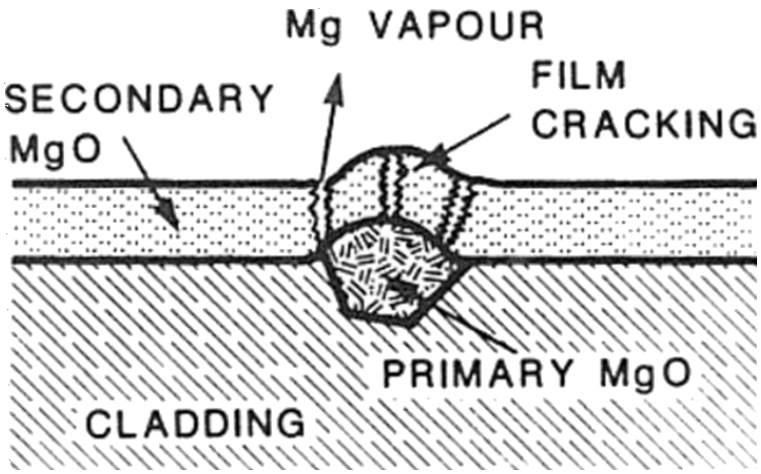

Figure 2-2 - Mechanism of Oxide Disruption in Cladding during Vacuum Brazing [21]

In CAB furnace brazing, the joining surfaces are typically fluxed, the filler metal is positioned, and the parts are assembled and fixtured. From here they are placed on a conveyor belt which feeds the parts through a three stage process. The assembly is usually heated in a pre-heated oven to drive the moisture or alcohol out of the flux. The assembly is then fed into a furnace, which is at the desired brazing temperature, and usually remains there for a desired time after it has reached the brazing temperature. The brazing temperature is chosen such that it is above the liquidus temperature of the filler metal composition but below the solidus temperature of the base alloy to be joined. A subsequent cooling chamber is used to allow time for capillary action to form a solid joint.

2.2 Aluminum Braze Sheet Composition and Microstructure

A large contribution to the final product in brazing lies in appropriate alloy additions. In the case of automotive brazing sheets, the typical sheet layout involves the sandwiching of aluminum alloy with desired mechanical properties referred to as the core layer. This layer typically occupies around 80% of the sheet and is of the 3XXX series (high manganese and iron) content. The 3XXX sheet is sandwiched between 4XXX series aluminum alloy (high Si content). The high silicon in 4XXX series aluminum alloy lowers its melting point below the 3XXX series and to be used in the brazing process. Typical aluminum alloys used in this application are ASTM AA 3003, 4343, 4045 [2].

Table 2-1 - Composition of Common Aluminum Alloys in Braze Sheet [2]

Aluminum	Si	Fe	Cu	Mn	Mg	Zn	Ti
3003	0.6	0.7	0.05-0.2	1.0-1.5	-	0.1	-
4045	9-11	0.8	0.3	0.05	0.05	0.1	0.2
4343	7.5	-	-	-	-	-	-

Of the constituents outlined in Table 2.1, both silicon and manganese have a limited solubility in aluminum whereas copper and magnesium have an extended solubility within solid aluminum. A brief discussion of each alloying element is necessary before continuing to understand its effect on the alloy and subsequent processing of the alloy.

Silicon is responsible for good castability and the ability to solidify in castings without hot tearing by imparting high fluidity and low shrinkage [22]. In fact silicon drastically reduces the cracking tendency of Al-Cu-Mg alloys [2]. As stated silicon has a limited solid solubility in aluminum (approximately 1.65 wt%), however, as the Al-Si phase diagram shows in Appendix A, silicon forms a eutectic with aluminum at much higher levels (around 12 wt%) [22]. Because of this silicon containing alloys undergo very little thermal contraction due to a relatively large volume fraction change. Small amounts of magnesium allow a silicon containing alloy to be heat treatable, however the converse is not true [2]. Silicon also acts as a grain growth inhibitor.

Additions of copper to the aluminum alloy increase its strength and hardness, but also lower the corrosion resistance of the alloy [22]. The increased hardness improves machinability of the alloy. Traditionally, copper was added in excess values of 10%, such aluminum alloys have since replaced copper with silicon for strength hardness additions. Following heat treatment, copper containing alloys will show lowered elongation with increased tensile and yield strength [2].

Magnesium has an extended solubility in aluminum of around 17.4% [2], as indicated in the phase diagram in Appendix A. However, its maximum value in wrought alloys is 5.5%. Magnesium alone in an aluminum matrix will form highly anodic precipitates along the grain boundary in the form of Mg_5Al_3 and Mg_5Al_8 [2]. Manganese is added to allow a more uniform

precipitation of Mg in the matrix and so that less Mg is needed for a given increase of strength. Figure 2.3 shows this increase in strength given certain percentages of Manganese for an Al-Mg-Mn alloy.

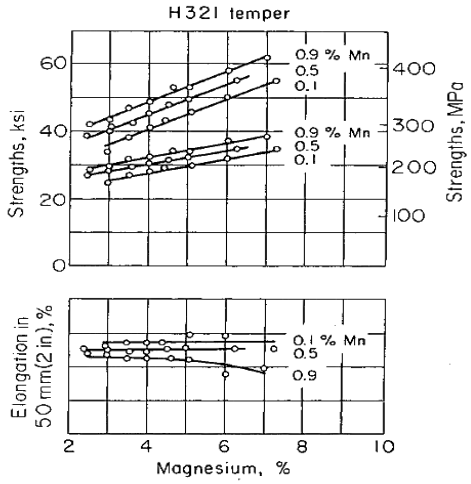

Figure 2-3 - Effect of Magnesium and Manganese on Aluminum Alloy Strength and Ductility [2]

Nickel has a low solid solubility in aluminum and becomes present as an insoluble intermetallic (Al_3Ni, Al_2Ni_3, AlNi) and is added to Al-Cu/Al-Si alloys to reduce thermal expansion.

The major constituents of AA3003 are manganese and iron and yield its dominant phases, $(Mn,Fe)Al_6$ and $Al_{12}(Fe,Mn)_3Si_5$. In the as cast structure, the former phase is most prevalent; however, subsequent heat treatment will cause a transformation by a delayed peritectic reaction to the latter. Cast AA3003 alloy forms equiaxed dendrites upon solidification which subsequently grow to form a globular dendritic microstructure. Manganese becomes supersaturated in these primary dendrites and precipitates as a dispersoid during homogenization (heat treatment) [2].

The as-cast 3003 microstructure shows $(Mn,Fe)Al_6$ and $Al_{12}(Fe,Mn)_3Si$ at the dendritic interstices, see Figure 2.4a. The $(Mn,Fe)Al_6$ phase has a needle-like structure with a hollow rhombohedral cross-section. The darker phase consists of precipitated $Al_{12}(Fe,Mn)_3Si$. This phase becomes more dominant upon homogenization of the alloy, see Figure 2.4b. This phase in the presence of increased silicon becomes $Al_{15}(Fe,Mn)_3Si_5$ is more commonly referred to as α-Al(Mn,Fe)Si phase which is cubic in structure [2][3].

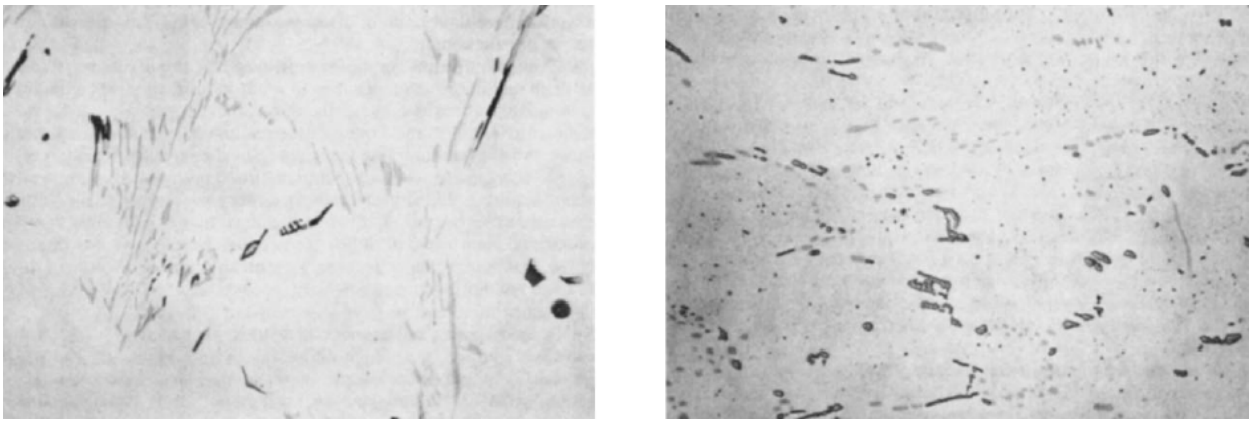

Figure 2-4 - (a) As-cast AA3003 ingot showing distribution of predominantly $Al(Mn,Fe)_6$ (light phase) and $Al_{12}(Fe,Mn)Si$ (dark phase), (b) Homogenized AA3003 where $Al_{12}(Mn,Fe)Si$ has become more prevalent (455X) [15]

The as-cast phases of AA4XXX alloys are elemental silicon and $Fe_2Si_2Al_9$. Most AA4XXX are termed hypoeutectic Al-Si alloys, meaning their composition of silicon lying below that of the eutectic composition (12.6wt%). Solidification of the as-cast structure begins with the formation of primary α-aluminum dendrites, followed by the Al-Si eutectic reaction; see Figure 2.5a. Homogenization of AA4043, shown in Figure 2.5b, leads to rounding and coalescence of the silicon phase while having little effect on the iron within the alloy. Small additions of manganese have been shown to shift the formation of β-AlFeSi phases to a less detrimental α-AlFeSi phases in terms of mechanical properties [2][22][23].

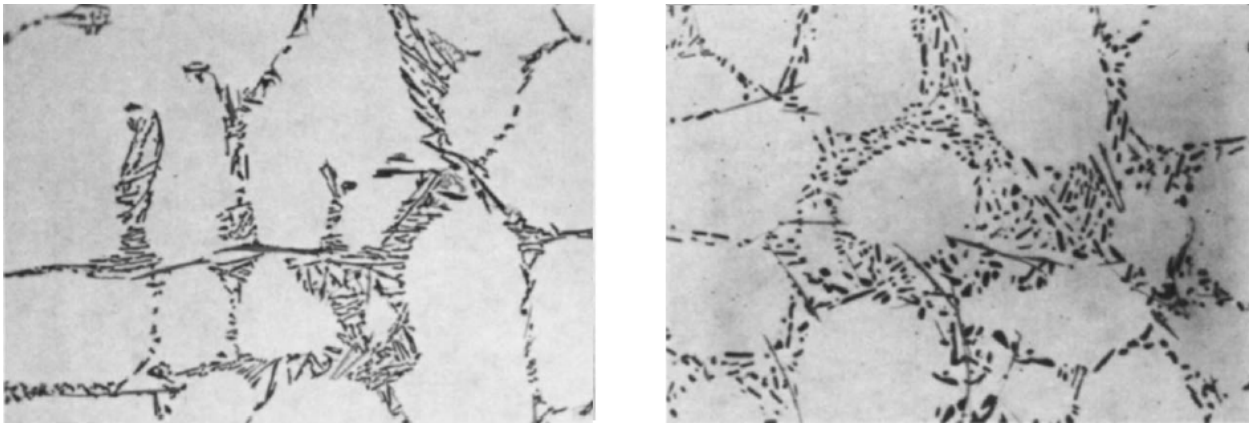

Figure 2-5 - (a) As-Cast AA4043 showing primary aluminum dendrites with α-$Al_9Fe_2Si_2$ (light phase) and Silicon (dark phase) at the interstices, (b) Homogenization of AA4043 showing coalescing and spheroidization of silicon particles (455X) [15]

2.2.1 Heat Treatments of Braze Sheet Aluminum Alloys

Typical heat treatments for the 3XXX series are full annealing (O), solutionizing and natural aging (T4), and solutionizing and artificial aging (T6). Full annealing reheats the alloy above its recrystallization temperature and removes effects of strain hardening from previous processes. Some strain from dislocations is relieved during the process and subsequently there is nucleation and growth of new dislocation free grains. It is worth noting that a slow cooling rate is necessary to minimize distortion and to maintain a stable solid solution [2].

T4 and T6 both involve solutionizing the alloy. This is done below the eutectic temperature and held to allow solid state diffusion as well as solutes within the aluminum matrix. Once finished, the sample is rapidly quenched to create a supersaturated alloy. T4 involves an aging process that is held at room temperature for a few days to several weeks. T6 temper is artificially aged at elevated temperatures, typically around 200°C [2].

Work hardening is used extensively to produce strain-hardened tempers of non-heat treatable alloys. A combination of strain hardening and partial annealing is used to produce the H28, H26, H24, and H22 series of tempers. The products are strain hardened more than is required to achieve the desired properties and then are reduced in strength by partial annealing. These tempers range from quarter hard to full hard, depending on the designation, with H24 (half hard) being a common temper for braze sheet.

2.2.2 Microstructural Changes Following Brazing

Figure 6 illustrates the microstructure of a contact point between two clad sheets before and after brazing [3]. During brazing the molten clad layer wets and spreads over the surface of the core material forming a fillet structure at the edge of the contact point between two sheets (i.e. Fig. 2.6b). As discussed previously, during brazing the molten metal clad layer redistributes itself due to surface tension forces. This creates three distinct regions in the joint. The fillet region is where most of the clad material flows, creating a liquid reservoir. Away from the fillet and contact point is the so-called “residue” region [24]

where much of the clad liquid has been depleted due to flow into the fillet. Liquid depletion also occurs at the contact or lap region, below the fillet shown in Figure 2.6. The microstructures in the fillet, residue and lap regions are different due to their different liquid content and solidification conditions. In the DANA process, the Ni plating metallurgically combines with the molten clad, altering its composition and influencing the as-solidified microstructure in the fillet, residue and lap regions. The formation of a band of dense precipitates (BDP) is discussed in section 2.2.4.

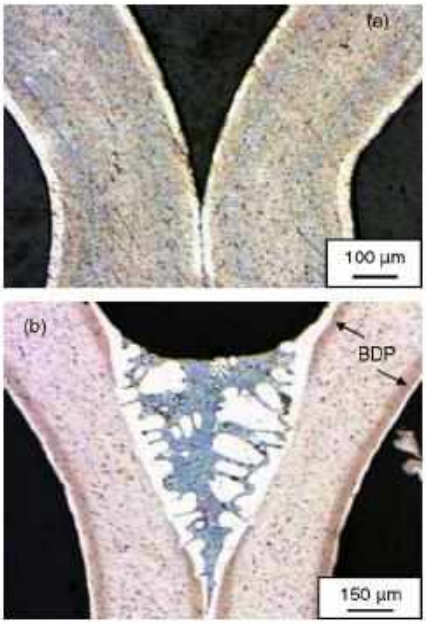

Figure 2-6 - Optical metallography showing a metallographic section before (a) and after (b) brazing for AA3003 sheets lined with AA4343 braze material [19]

In order to ensure the integrity of the bond, the effects of processing variables on the quality of the joint must be understood. The volume and composition of liquid metal produced during brazing will determine the quality of the joint formed, including the size and shape of the fillet, and the microstructure in the fillet, residue, and lap regions [25][26]. In turn, joint quality will determine the overall mechanical strength of the honeycomb-like heat exchanger structure while the surface microstructures in the joint and residue areas will determine the overall corrosion resistance and thermal conductivity of the structure. Therefore liquid volume and composition (including the solidification behaviour of this liquid layer) play a critical role in the performance of Al based automotive heat exchangers [26][27].

2.2.3 Diffusion of Silicon and Manganese

The cladding consists almost entirely of aluminum and silicon. These two constituents form a simple binary eutectic with limited solubility of Al in Si (or Si in Al) in solid solution. Appendix A shows the phase diagram of the Al-Si system. The melting temperature of the aluminum can be lowered from its pure state (659.7°C) to the eutectic temperature of 577ºC with the addition of 12.6 wt% silicon [28]. A hypoeutectic system is commonly used in clad manufactured with 4XXX series aluminum between 7.5-12 wt% silicon [2]. Upon cooling, the molten clad forms a network of primary aluminum and needle-like silicon. It has been shown that in reality the 3-D network of these solidified silicon particles is flake-like in nature [14]. Upon resolidification the hypoeutectic cladding forms into primary α-aluminum and aluminum silicon eutectic, shown as the white and blackish phases respectively in Figure 6b. Silicon is said to coalesce into needles, more accurately flakes as shown in Figure 2.7. An established phenomenon of the brazing process of 3XXX/4XXX sheets is the counter-diffusion of silicon and manganese from the clad to core and core to clad [29][30].

From a diffusional standpoint, a close approximation is the diffusion process across a plate boundary which is described by Fick's Laws: $J = \frac{dC}{dt} = -D\frac{\partial C}{\partial x}$ and $\frac{\partial C}{\partial t} = D\frac{\partial^2 C}{\partial x^2}$

Where J is the amount of solute moving through a unit area, and C is some concentration level at a given distance into the plate, x. Both these equations assume small values of C and small differences in C along the length of the plate. For cases where this is not satisfied, the equation becomes $\frac{\partial C}{\partial t} = \frac{\partial C}{\partial x}(D\frac{\partial C}{\partial x})$.

All of these equations apply only to a microstructural scale and do not apply in consideration of atomic/thermodynamic considerations. The diffusion coefficient D is temperature sensitive and related to the defect energy of the crystal lattice and the energy of diffusional motion $D = D_o e^{-\frac{Q}{RT}}$ [31]. Here Q is the activation energy to promote diffusion, D_o is a temperature-independent pre-exponential, T is the given temperature, and R is the gas constant.

The diffusion of silicon and manganese is easily understood through Fick's first law. High concentrations of silicon in the presence of temperature and time will move to areas of low

concentration such as the core. The same is true for manganese moving from the core to the clad. These elements begin diffusing at much higher rates during ramp up and peak brazing temperatures. Literature has shown that this diffusional motion is not so easily described by Fick's second law, neither is the diffusion coefficient of silicon established in reference books applicable [32].

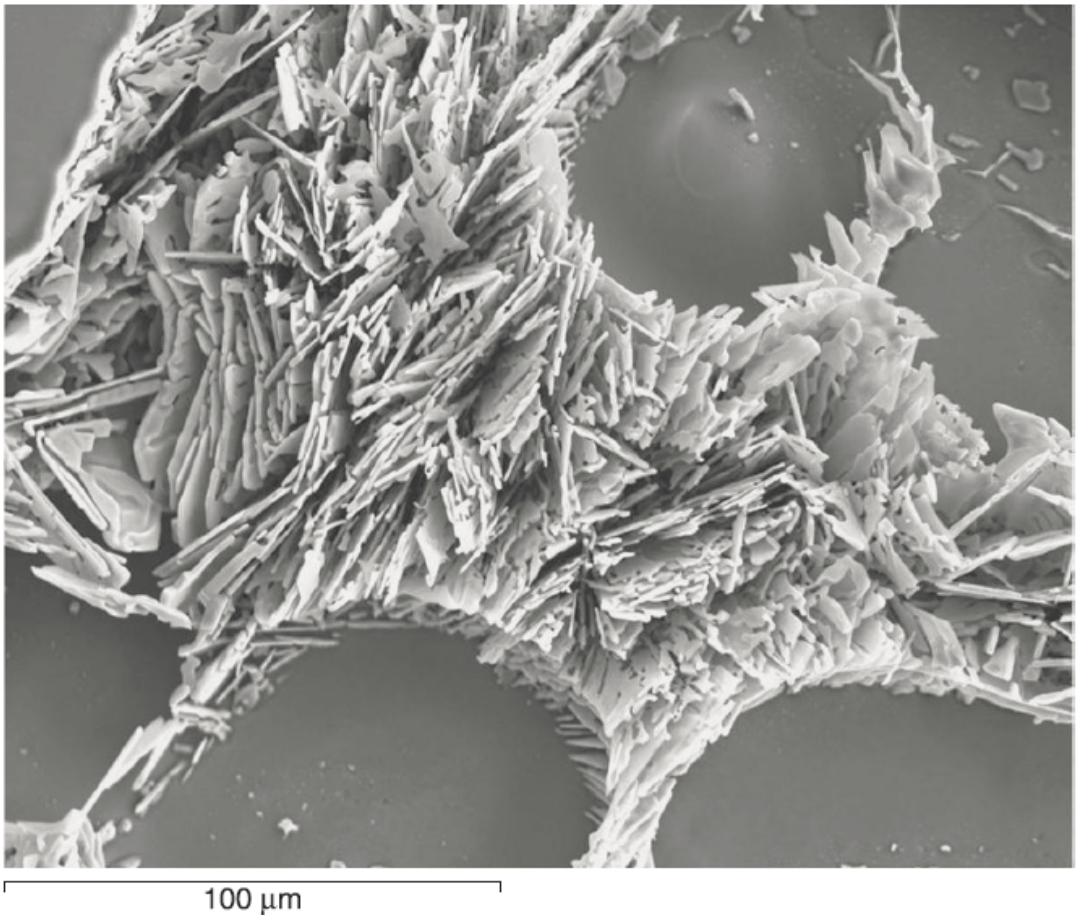

Figure 2-7 - SEM image of exposed eutectic area of a brazed joint [14]

Through use of an electron probe micro analyzer (EPMA) and application of Fick's second law as a first approximation, the particular diffusion rate of silicon across the clad core interface via bulk and grain boundary diffusion has previously been measured. The rates of diffusion, D, at 793K and 893K were given to be 3.4×10^{-13} m^2/s and 2 - 2.8×10^{-12} m^2/s respectively [32]. The diffusional rate increases with temperature as dictated by,

$$D = D_o e^{-\left(\frac{Q}{RT}\right)}$$

The diffusion of silicon through braze sheet is a known 'diffusion from a distributed source' problem. The core is assumed to be a slab of pure Al and the clad a mixture of Al and Si where the concentration of Si is constant over time, t, at the interface. Allowing the initial concentration of Si to be C_o which is uniform in the clad and not present at all in the core region (forming a metallurgical bond along the interface without any mixing)[30-32]. It can be shown that this problem observed over a thickness, y, resolves to the integral,

$$C(y,t) = \frac{C_o}{\sqrt{\pi}} \int_{-\infty}^{y/2\sqrt{Dt}} \exp(-\eta^2)\, d\eta \;\; where\, \eta = \frac{y}{2\sqrt{Dt}}$$

$$C(y,t) = \frac{C_o}{2}\left[1 + \mathrm{erf}\left(\frac{y}{2\sqrt{Dt}}\right)\right] = \frac{C_o}{2}\left[\mathrm{erfc}\left(\frac{-y}{2\sqrt{Dt}}\right)\right]$$

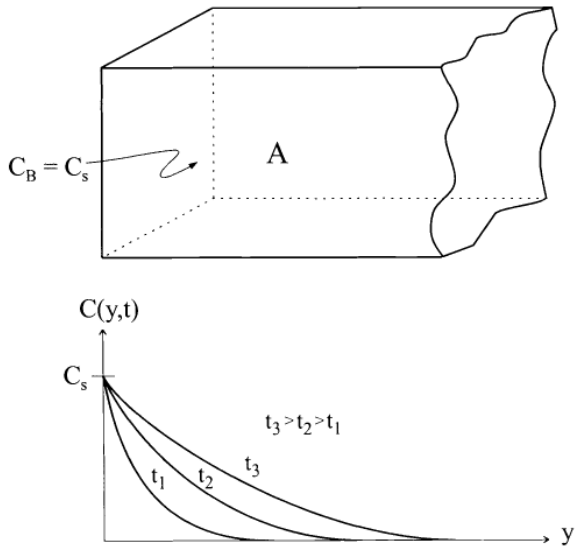

Figure 2-8 - Concentration profile of silicon and manganese diffusion across the clad/core interface [27]

Figure 2.8 shows the concentration profile for increasing times at a constant initial surface (clad) concentration and diffusion coefficient [31]. A similar inverted curve would describe the diffusion of manganese into the clad region. While not a perfect description of silicon diffusion, due to local effects and a changing diffusion coefficient, the concentration profiles have been shown to mesh well with experimental work [30][32].

There are several factors which affect this rate of diffusion locally across the interface. These include molten liquid penetration, subsequent core erosion into the molten clad and liquid suppression leading to the creation of a residue zone. The residue zone is the region of resolidified clad that remains on the surface of the core that was not moved by surface tension to the fillet joint. This remainder as stated above consists of primary α-Al and Al-Si eutectic [30][32].

With continuous exposure to high temperatures above melting, the braze sheet will undergo

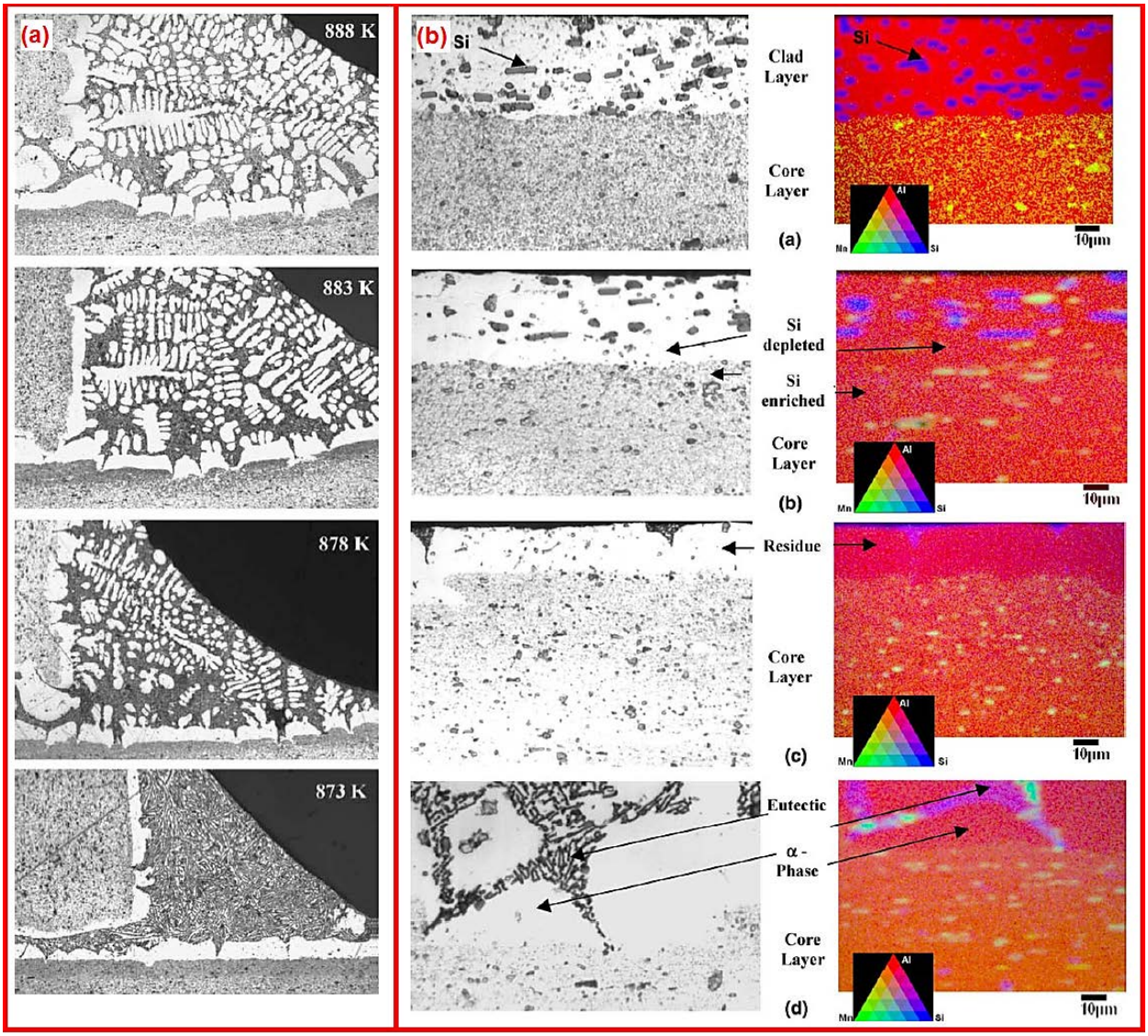

Figure 2-9 - Multiple temperature holds of braze sheet joint demonstrating increased silicon depletion by increasing presence primary aluminum dendrites at higher temperatures [27]

isothermal diffusional solidification. This is a result of the aforementioned silicon uptake from the cladding to the core via solid state diffusion and diffusion in the molten clad state. Solid state diffusion, though present at low temperatures, becomes significant at elevated temperatures, and can lead to Si depletion suppressing liquid formation if held too long, see Figure 2.9. A large portion of silicon diffusion has been shown to occur during melting of the clad layer where silicon diffuses, and segregates as Si-rich phases, along primary α-Al grains. The outcome of this bulk diffusion of silicon is the formation of a depleted zone in the clad and a silicon rich zone in the core [30][32].

2.2.4 Long Life Alloys and Band of Dense Precipitates

The counter diffusion of manganese and silicon creates a diffusion zone where new intermetallics form, termed the band of dense precipitates (BDP). The BDP can be seen following brazing, or near brazing, temperature treatment below the clad layer. The formation involves the decomposition of $Al_6(Mn,Fe)$ intermetallics in the core into a cubic α-Al(Mn,Fe)Si phase, see Figure 2.10. BDP thickness is improved from dissolution of the core into the cladding which provides significant manganese enrichment. The thickness of this region was found to be on the order of 20-60μm [2][29][33].

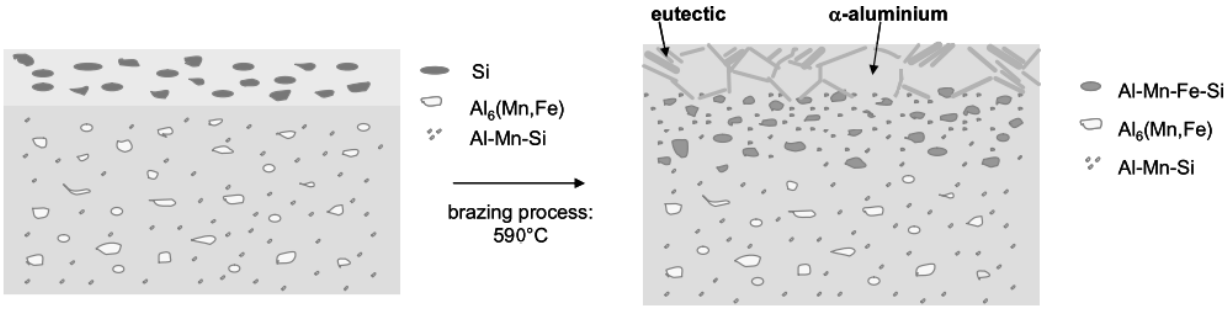

Figure 2-10 - Diagram outlining microstructural changes before and after brazing [34]

Formation of the BDP layer is relatively new to braze sheet technology and is inherent of 'long-life' alloys which have been shown to offer enhanced corrosion protection. The precipitates within the band are preferentially corroded to the core, and because of this the core is left intact when the sheet is exposed to corrosive media [2][29][33].

2.3 Fluxless Brazing through a Nickel Modified Layer

The use of a nickel braze promotion layer was first proposed by K.F. Dockus in the 70's as a new method of fluxless brazing [35]. At the time, this layer was an alternative to vacuum brazing which used a magnesium getter to destabilize the surface oxide under low pressure. In literature, the process is outlined as using an electrolytically deposited nickel layer on the surface of the aluminum braze sheet [35][36]. At a certain temperature, prior to melting during brazing, the nickel layer reacts with the aluminum exothermically due to the formation of intermetallics. This exothermic action has been proposed as the method by which the oxide layer is disrupted and molten clad is able to flow [5].

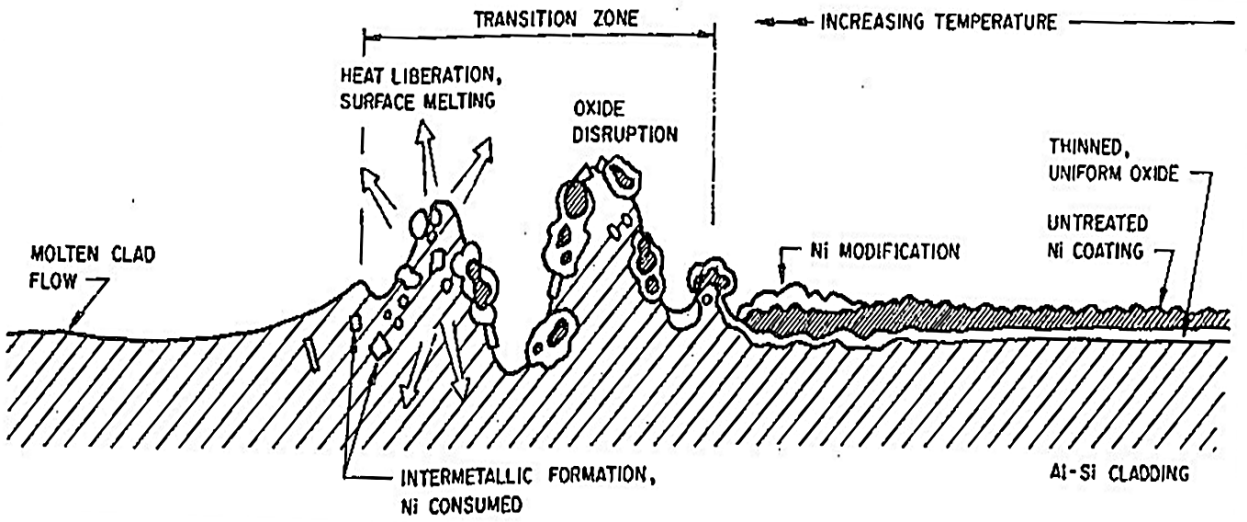

Figure 2-11 - Proposed Method of Oxide Disruption by Nickel Braze Promotion Layer [5]

The nickel braze promotion layer has been studied in literature before and the heat and pressure emitted from intermetallic formation are attributed as the cause of bond promotion, see Figure 2.11 [5]. The diagram starts from the right with the deposited nickel resting above the natural braze sheet oxide layer. As temperature and time are increased, there is an observed modification in the nickel layer which has been verified under SEM and optical microscopy [5][36]. The intermetallic phases documented are Al_3Ni_2 and Al_3Ni phases which lead to a surface roughening which will be discussed later in this section.

Cheadle and Dockus observed cut as-received braze sheet placed inside a glass tube furnace. Samples exposed to temperatures up to 550°C showed no change in appearance. As mentioned previously, a modification of the nickel layer was observed at 560°C where coarsening of the surface became evident. This initial intermetallic formation was thought to take place underneath the nickel layer through possible Ni/Al diffusion. The point of oxide disruption and molten clad flow was designated ~570°C where extreme localized surface roughening carried fragments of nickel which transformed to Al_3Ni_2 intermetallic clusters. From here melting progressed across the thickness and all of the nickel coating and Al_3Ni_2 intermetallic transforms to Al_3Ni [5].

The heat of formation of aluminum nickel intermetallics is an important characteristic of the nickel braze layer and one that is quantifiable under calorimetry. These heats of formation are well known in literature and are summarized in Table 2.2. Experimental values were found using Direct Reaction Calorimetry (DRC) and calculated values were done using semi empirical models. When a reference state for solid nickel and solid aluminum was applied, the enthalpy of formation for Al_3Ni_2 and Al_3Ni were -57.9 ± 1.1kJ mol^{-1} and -43.2 ± 1.1kJ mol^{-1} respectively [37].

Table 2-2 - Experimental and Calculated Values for Molar Enthalpies of Formation of Aluminum Nickel Intermetallic [37]

	Molar Enthalpy of Formation (kJ mol^{-1})	
Compound	Experimental	Calculated
Al_3Ni_2	-58.83 ± 1.1 -57.6 ± 1	-43.0 -52.0 -59.1 -61.9
Al_3Ni	45.06 ± 1.1 -37.7 ± 1	-28.0 -35.5 -37.6 -39.9

Another important aspect of the nickel layer is the interaction with silicon in the clad layer, see Figure 2.12. The Al-Si-Ni ternary system has been calculated and documented by Klaus et. al. The application of a small uniform nickel layer on the surface of a relatively large slab of aluminum silicon means that we can expect low concentrations of nickel relative to the other constituents. Also, the clad layer is roughly 10% Si which helps to

pinpoint phase formation to the regions of (Al_3Ni_2) and (Al_3Ni) depending on local levels of nickel concentration. Finally, brazing temperatures are held below 600°C further isolating the paths of phase formation within a small isotherm in the bottom left of the diagram. The main phase outlined in this region, E1, is given as L = (Al) + (Si) + (Al_3Ni) with a eutectic temperature of 565°C [38]

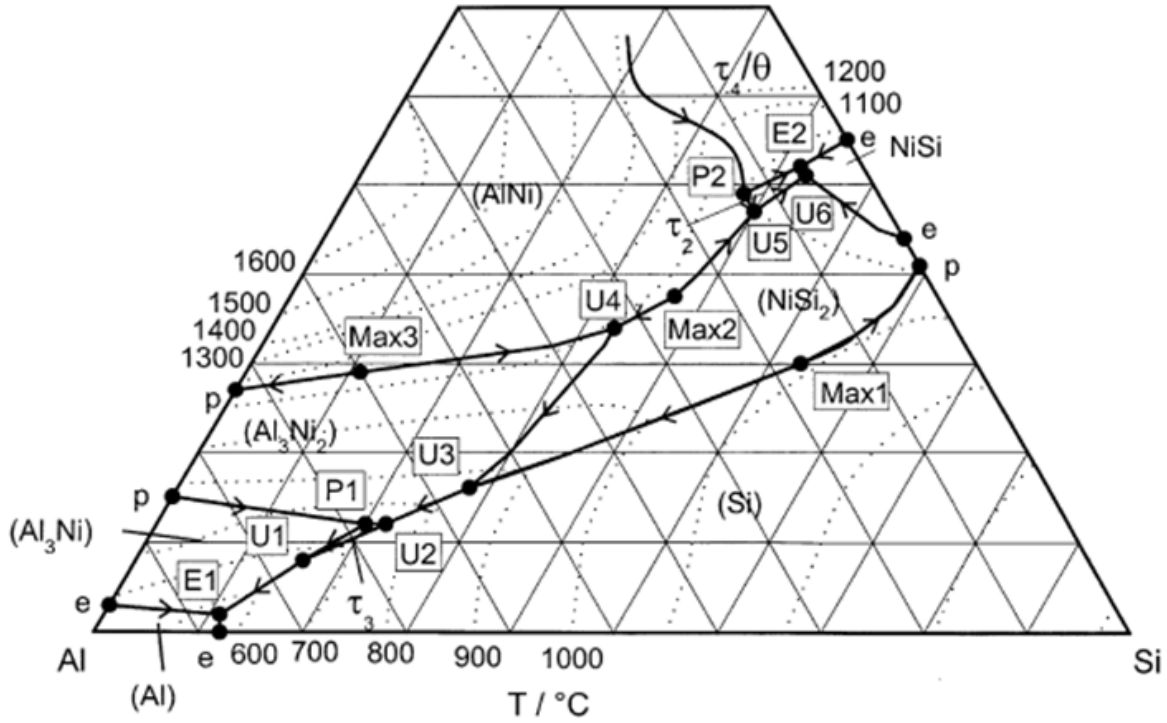

Figure 2-12 - Al-Si-Ni Ternary Phase Diagram [38]

With even a small amount of Ni in contact, this is a tremendous amount of heat that can be released at discrete locations across the surface. DSC traces conducted previously have demonstrated this with exothermic reactions of 8-15 J/g with only fractions of a milligram coated over the aluminum surface shown later in Chapter 5. This heat probably has an effect on disruption of the oxide but will not come close to the melting point of alumina (~2000°C) [39]. Alumina is a hard substance as well, possessing a Mohs hardness of 9 out of a possible 10 (diamond being the hardest). However, typical amorphous alumina found naturally on the surface or made artificially through heat or electrochemical methods possess hardness around three times lower [40]. This oxide is still quite brittle and when subjected to very little, if any, plastic deformation cracking can occur such that discrete regions of aluminum can come into direct contact with the nickel.

Therefore, it is more likely that the oxide is somehow distorted mechanically which leads to perforation and exudation of molten clad. This hypothesis can be reinforced by examining changes in atomic structure from solid aluminum and nickel to these intermetallics, see Figure 2.13. The formation of the more prominent Al_3Ni leads from a face centred cubic structure found in solid aluminum (blue atoms) and nickel (red atoms) to an orthorhombic D_{20}Pnma crystal lattice [41]. The lattice parameters for these structures are outlined in Table 3.

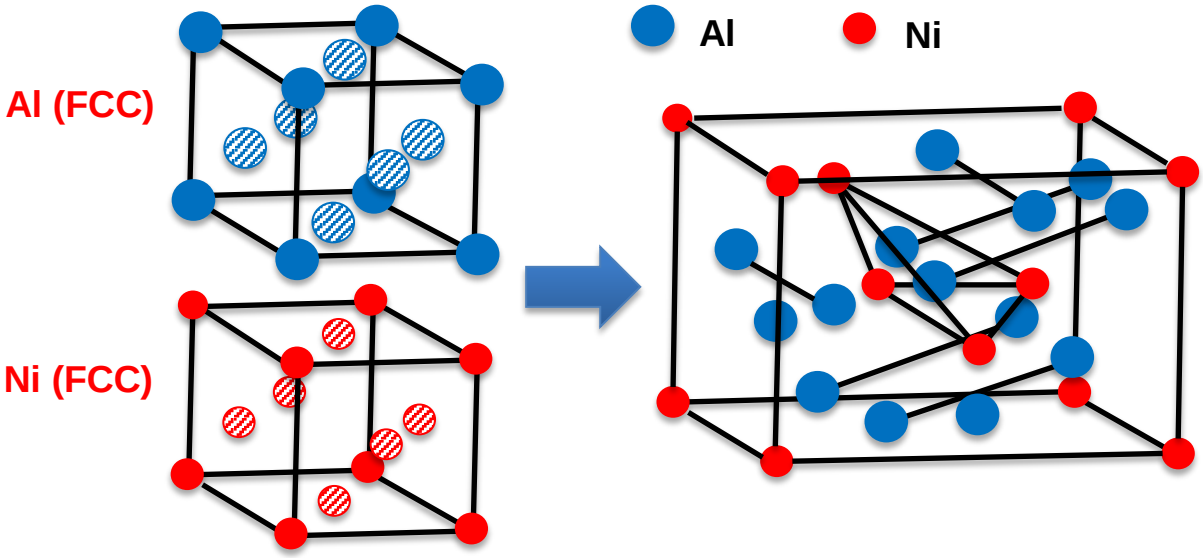

Figure 2-13 - Change in Crystal Structure from Solid Aluminum and Nickel to Al_3Ni [41]

A substantial increase in volume (roughly four-fold) occurs during the phase transformation to Al_3Ni. This dynamic increase is thought to be the major contributor to both disrupting the oxide and roughening the surface. With a ratio of one nickel to three aluminum, a large portion of aluminum is consumed at the near surface. As a consequence, the nickel aluminide intermetallic will work its way into the clad layer and create a layer of Al_3Ni roughly 3-4 times that of the original nickel layer, see Table 2.3.

Table 2-3 - Crystal Lattice Parameters of Solid Aluminum, Nickel, and Al_3Ni [41]

Crystal Lattice Parameters (Å)	Al (FCC)	Ni (FCC)	Al_3Ni (D_{20}Pnma)
a	4.05	3.52	6.615
b	4.05	3.52	7.336
c	4.05	3.52	4.812
Volume	66.43 Å^3	43.61 Å^3	233.52 Å^3

Following the disruption of the oxide layer and exudation of the molten clad onto the modified braze sheet surface, all the remaining nickel on the surface becomes immersed in molten clad. There have been numerable studies of combining aluminum and nickel in multilayers, powders, or solid/liquid states for the purpose of intermetallic synthesis and study [42-44]. Studies in multilayers have shown the growth of Al_3Ni is a two stage process where initially growth of the intermetallic progresses laterally from isolated nucleation sites along the Ni/Al interface and then proceeds to consume all aluminum [42].

Kyriakopolous et al. immersed solid nickel coupons into molten aluminum at temperatures between 700-900˚C for thirty seconds to a minute [43]. This reactive solidification was done to establish whether nickel dissolution in aluminum occurs as the rate limiting extent of the reaction, or that the opposite is true (ie. aluminum dissolution in nickel). It was found that liquid aluminum eats away the nickel and forms intermetallics which grow unstable at the interface and partition away, see Figure 2.14a. Another interesting observation in this work was that aluminum oxide can inhibit the formation of intermetallic Al_3Ni (Figure 2.14b) [43]. This reinforces the postulation of some method of diffusion for nickel or aluminum across the oxide layer proposed by Cheadle and Dockus [5].

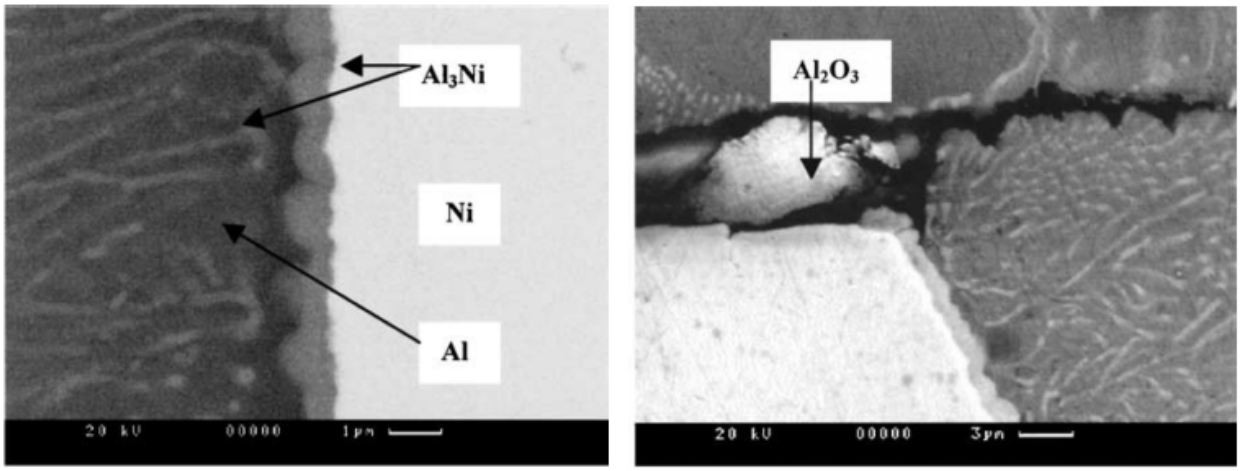

Figure 2-14 - (a) SEM image of the Formation of Al_3Ni Intermetallic at the Interface of Solid Nickel and Molten Aluminum, (B) Aluminum Oxide Inhibiting Intermetallic Formation at the Interface [43]

2.4 Aluminum Oxide

The primary challenge in aluminum sheet brazing lies in the removal of a tenacious aluminum oxide layer on the faying surface of the clad layer surface, which can prevent wetting and free flow of the clad. Molten aluminum and solid nickel interfaces have also shown that aluminum oxide can act as a barrier to the intermetallic reaction necessary to disrupt it [43]. The method by which this layer is disrupted and later displaced is vital in further understanding the fluxless nickel modified brazing process.

Aluminum generally has excellent corrosion resistance in natural atmospheres and aqueous environments due to its unique ability to naturally passivate. A thin layer of oxide passivates on any exposed aluminum surface and protects it from further oxidation. Aluminum alloys are not as well protected due to the galvanic effect of constituent additions [45]. Both exhibit a natural oxide layer in neutral pH range, which for pure aluminum is ~4-8.5, as shown in

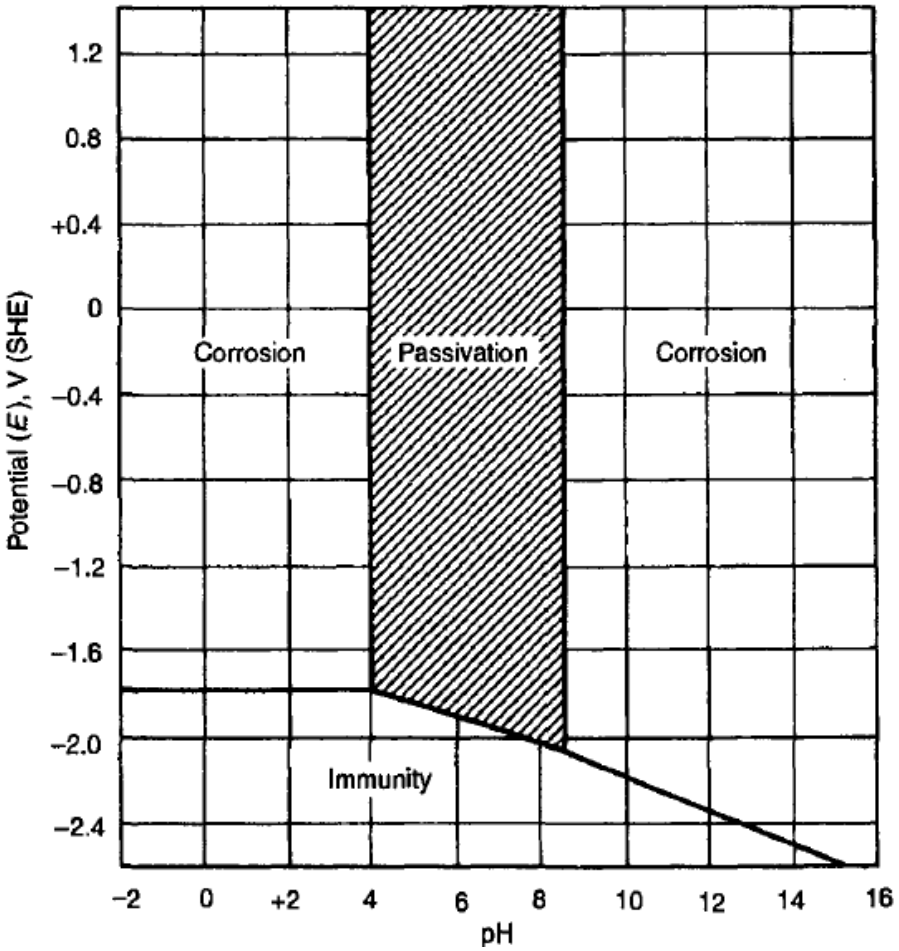

Figure 2-15 - Pourbaix Diagram of Pure Aluminum [45]

Figure 2.15.

Figure 2.16 outlines the configuration of the formed aluminum oxide layer into two distinct layers. First a dense, compact layer of uniform thickness grows from the exposed aluminum surface called the barrier layer. Following this uniform layer, defects in the oxide/aluminum surface lead to the formation of pores along the surface of the barrier layer. This is known as the porous layer. The combination of these two layers is typically found to be on the order of 10 nm; however aluminum alloys may have as little as 5 nm [46].

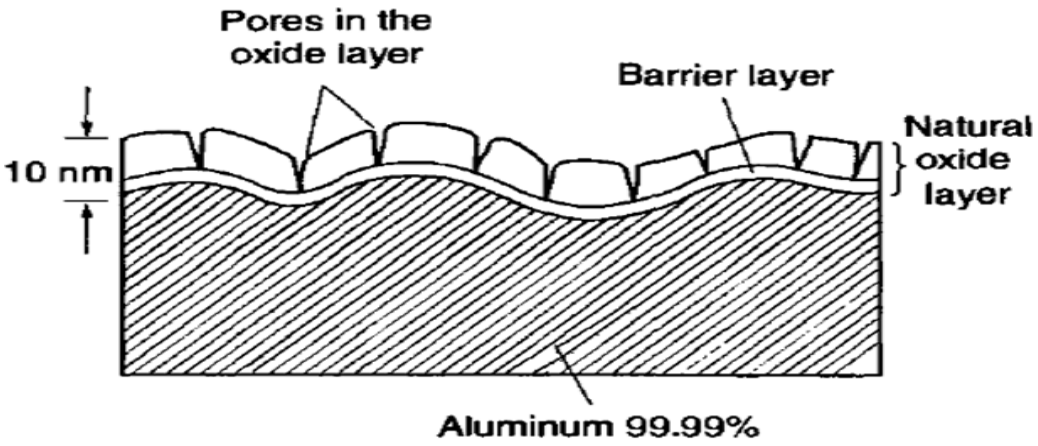

Figure 2-16 - Aluminum Oxide Structure on the Surface of Pure Aluminum [46]

The natural oxide layer is amorphous in nature and can be composed of aluminum oxide, hydroxide, or hydroxide oxide. The porous layer consists of a hydrated layer whereas the barrier layer is mostly aluminum oxide. This microstructure is entirely dependent on its environment whether aqueous, or in dry/humid air [47]. These environments can have an impact on the 'brazability' of aluminum braze sheet. One of the largest effects on overall brazing was attributed to humidity and the presence of water in the pores of the oxide surface [47].

Variations in temperature, electrolyte, voltage/current, humidity, or exposed oxygen will have an effect on the oxide. Figure 2.17 shows the different phases of oxide which can develop at varying temperature. These phases each possesses a different crystal structure and their own unique physical properties, such as density and atomic spacing [48][49].

The various metastable polymorphs that can form, aside from the more common corundum (α-Al_2O_3), are divided into two categories, those with fcc packing and those with hcp packing. Polymorphs with fcc packing include γ, η, θ, and δ, and α, κ, and χ exhibit hcp packing. Thermal and electrochemical treatments (such as annealing and anodization), that can cause the aluminum oxide layer to passivate further, exhibit similar transitional behaviors, see Figure 2.18 [49]. These methods will be described further in section 2.5.2

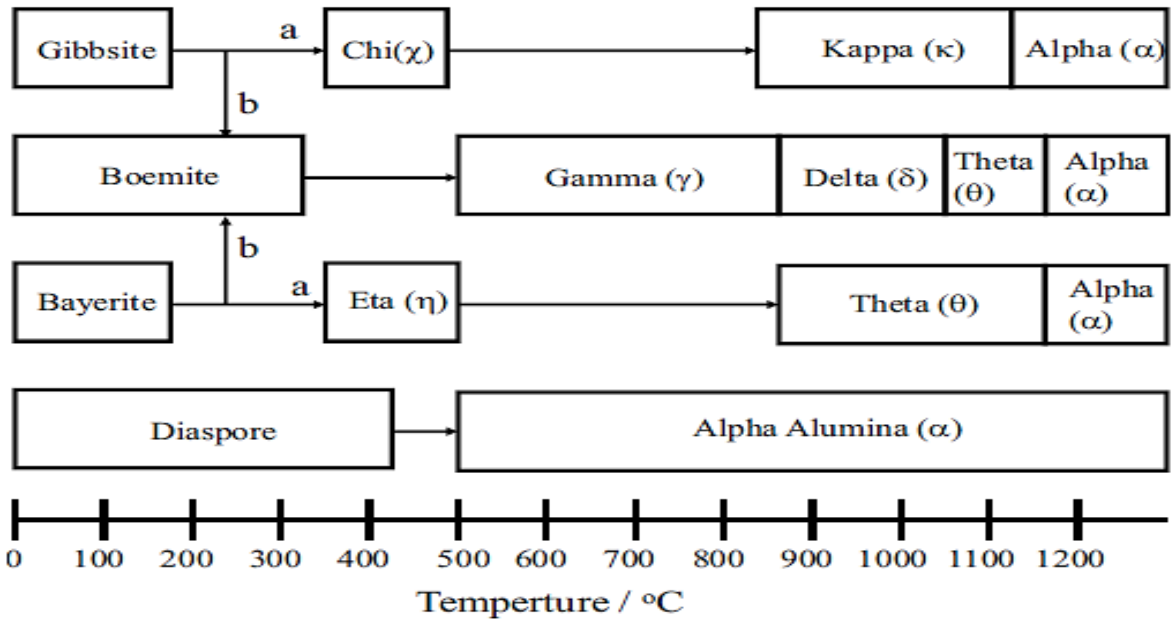

Figure 2-17 - Effect of Temperature on the Structure of Aluminum Oxide [48]

fcc

$$\gamma\text{AlOOH (boehmite)} \xrightarrow{300°–500°C} \gamma \xrightarrow{700°–800°C} \delta \xrightarrow{900°–1000°C} \theta \xrightarrow{1000°–1100°C} \alpha\text{-}Al_2O_3$$

$$\alpha\text{-}Al(OH)_3 \text{ (bayerite)} \xrightarrow{200°–300°C} \eta \xrightarrow{600°–800°C} \theta \xrightarrow{1000°–1100°C} \alpha\text{-}Al_2O_3$$

$$\text{Amorphous (anodic film)} \rightarrow \gamma \rightarrow \delta \rightarrow \theta \rightarrow \alpha\text{-}Al_2O_3$$

$$\text{Melt} \rightarrow \gamma \rightarrow \delta,\theta \rightarrow \alpha\text{-}Al_2O_3$$

Figure 2-18 - Polymorph Progression of Aluminum Oxide during Thermal or Anodic Treatment [49]

2.4.1 Growth of Aluminum Oxide

As noted above, the thickness and properties of aluminum oxide can be enhanced using different thermal, electrochemical, and chemical techniques. Significant growth of aluminum oxide (~1nm) can occur at temperatures as low as 100ºC of thermal treatment [50]. Anodization of aluminum can yield oxide layers several microns in thickness and which consist of different structures from the natural layer [51]. Certain oxidizing acids have been shown to enlarge the aluminum oxide layer as well [52]. Other methods do exist for oxide growth, but for the purposes of this paper only these methods will be discussed.

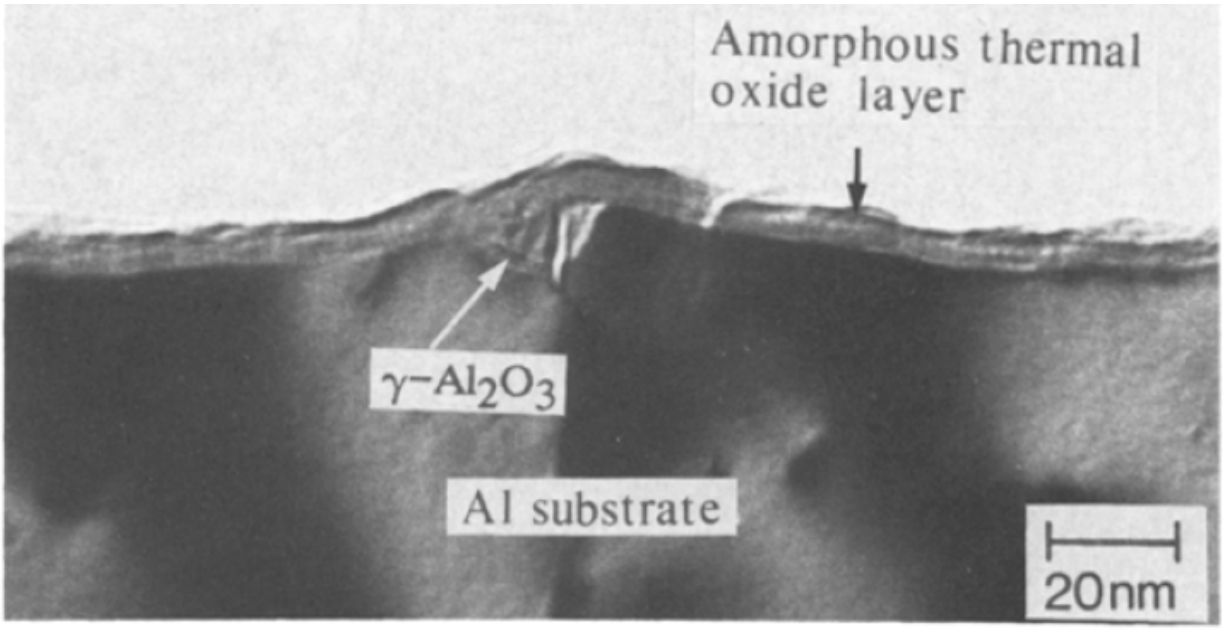

Figure 2-19 - TEM Image of Ultramicrotomed Section of Thermal Oxide Layer Grown in Air at 515°C [54]

Diagnosis of thermal oxide was heavily studied in the 50's and 60's to determine the rate of oxide growth and better understand the nature of its structure [50][53]. The results of such work found that from room temperature up to about 300-350°C an inverse logarithmic law best described oxide growth. From temperatures of 350-450°C the kinetics were best described as a parabolic relationship. Finally, at temperatures beyond 450°C, a marked transition occurred from an amorphous structure to γ-alumina. This transition continued until the entire surface was γ-alumina at which point the kinetics became more complex and significant weight gains were observed at further elevated temperatures [53].

Through use of Transmission Electron Microscopy (TEM) and ultramicrotomy, extremely thin sections cut with a glass, or diamond knife, of cross sectional specimens were able to show this transition, see Figure 2.19. The initial formation of γ-alumina was found to be at the amorphous oxide – metal interface where it grew laterally from initiation sites. It was postulated by Shimizu et al. that this growth was made possible by small local cracks in the amorphous oxide, which have never been verified under imaging [54]. The sites of formation were presumed to be at metal ridges and defects on the surface following processing. These cracks provided a transport pathway for oxygen to diffuse to the metal-oxide interface, see Figure 2.20 [54].

Anodization of aluminum is a common industrial technique for the growth of aluminum with a range of applications. Depending on the solvent action of the electrolyte used, two different alumina structures can form. In near neutral solutions, where the oxide is completely insoluble, an oxide can be grown consisting entirely of the barrier type layer, see Figure 2.16. In more aggressive solutions, a combination of barrier and porous layer are grown in combination [55]. Throughout this document, these two electrolyte and oxide types will be described as barrier and porous type.

In terms of the process itself, anodization involves the use of an inert cathode and a metal anode to be oxidized in a chosen electrolyte. A voltage is applied which promotes electronic and ionic conduction through the oxide layer. Aluminum oxide films exhibit a low electronic conductivity and a high ionic conductivity. Figure 2.21 shows an ionic exchange within a pore exposed to sulfuric acid. The growth of the oxide layer involves the inward migration of

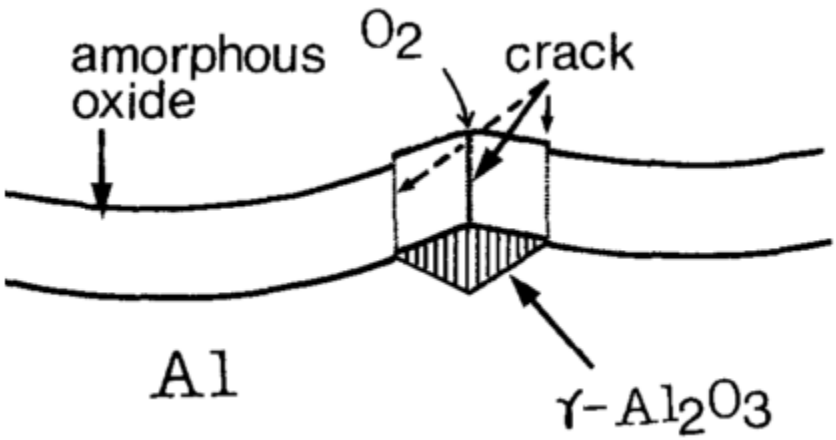

Figure 2-20 - Cracking of Amorphous Oxide through Formation of γ-Al_2O_3 [49]

O^{2-}, or OH^-, ions and the outward drift of Al^{3+} ions. The formation of Al_2O_3 has been shown to occur not only at the oxide/electrolyte interface but at the metal/oxide interface as well (at least for porous type). Migrating electrolyte anions may become incorporated into the growing film as the process continues [56].

Barrier type oxides are used commercially in dielectric capacitors and in protection of vacuum-deposited aluminum. The formation of this layer is solely a function of the temperature of the electrolyte and voltage applied. At low voltages (<100V) and electrolyte temperatures, barrier type oxides are primarily composed of amorphous aluminum oxide, with irregular patches of crystalline γ-oxide and hydrated oxide near the surface [55][57]. More recent studies have shown that at applied voltages over 200V voids form in tandem with crystalline γ alumina which may begin to breakdown the surface film of the barrier oxide [58].

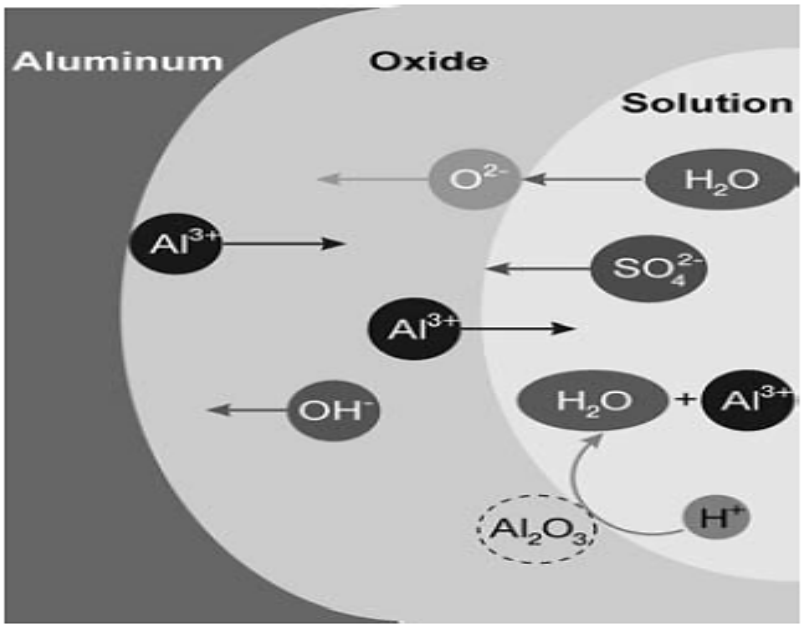

Figure 2-21 - Ionic Exchange at Pore Interface in Sulphuric Acid Solution [56]

Porous grown oxide layers are a function of applied voltage, current density, time, and the temperature of the electrolyte. These layer types show much more sensitivity in nature to electrolyte temperature and are designated hard anodization at low temperatures (0-5°C) and soft anodization at higher temperatures. Hard anodization layers show excellent abrasion resistance, whereas both porous types can be filled with paint, or dye, and sealed

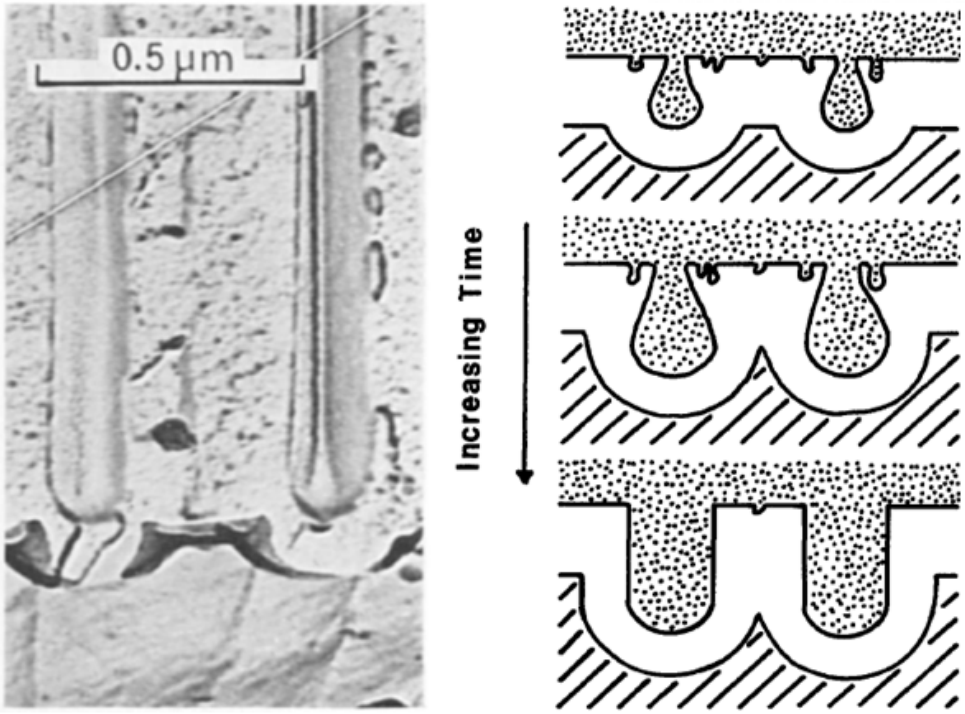

Figure 2-22 - (a) TEM image of Ultramicrotomed Section of Porous Oxide Anodized from Phosphoric Acid, 120V, 25, 5 minutes (b) Schematic of Pore Formation [59][61]

[55][59]. Large porous layers can be grown of the hard anodization type through a technique called Plasma Electrolytic Oxidation (PEO).

PEO is a common industrial technique using high voltages, around 500V, for achieving thick oxide layers on the order of 20-50 µm and is known as a form of hard anodization. This creates a very thick, dense layer on the surface of aluminum which is excellent as a form of surface treatment for other aluminum applications. It is also known to induce sparking on the surface of the oxide due to the high temperature evolution (~10000K). This is similar to a minor eruption caused by excessive voltage to a particular local region on the oxide. As a result, PEO oxide layers tend to contain 2-15% porosity [60].

The porous type layer is believed to consist of an inner, relatively compact, anhydrous form of alumina, an intermediate transition region (where the conversion of the inner anhydrous region to an outer region of high hydration is seen), and an outer region consisting mainly of hydrated oxide, where the extent of hydration and oxide density varies. It is through the intermediate transition region of hydrated oxide that electrolytic conduction is assumed to occur [55].

The porous region also demonstrates a hexagonal cell type structure to the pores which are evenly distributed across the surface, see Figure 2.22a. The formation of these pores is described in the schematic of Figure 2.22b. Defects on the surface of aluminum pose as initiation sites where a pore forms. These pores begin to grow wider at the base first and then begin to coalesce with other smaller pores and lesser defects [61]. The final uniform structure and its dimensions are a function of formation voltage, electrolyte, temperature, and concentration [59][61].

Chemical treatment of aluminum has shown to be a mechanism for alumina growth also [52]. Studies by Iwata conclude that either porous or barrier type oxides can be grown in highly oxidizing solutions, such as nitric acid. When using 68wt% concentration HNO_3 pure aluminum will form a porous region and 98wt% HNO_3 yields barrier type oxides. The thickness of these oxides over 20 and 90 minutes, respectively, was on the order of 40nm, and showed to be mostly amorphous. It was proposed that the lack of water molecules in 98wt% nitric acid was cause for lower reactivity and thus less preferential dissolution of the oxide layer [52].

2.4.2 Effect of Alloying and Substrate Surface on Aluminum Oxide Growth

So far all the discussion of aluminum oxide and its growth have been in consideration of pure aluminum. Problems in the anodization of aluminum alloys for membrane, or microelectronic, technologies have been observed in 2xxx (Al–Cu–Mg), 7xxx (Al–Zn–Mg) wrought and 3xx.x (Al–Si–Cu), and 4xx.x (Al–Si) cast alloys. The presence of a non-uniform surface, as well as second phase particles, tends towards the generation of an irregular and sometimes discontinuous oxide layer [62].

Additions of copper and, more importantly, silicon are added to aluminum cast alloys in concentrations exceeding the solid solubility of pure aluminum. These additives segregate at grain boundaries and are found distributed at the surface of the cast alloy. Anodic oxidation of these alloys usually results in the formation of thin, soft, powdery layers with a high propensity for ‘burning’ (local dissolution of surface layer and underlying alloy). Silicon also acts as a grain refiner to the cast alloy, yielding a finer grain structure on the surface. A

finer microstructure was shown by Fratila-Apachitei et al. to improve uniformity of overlying oxide [62].

Aside from ‘burning’ of the alloy surface, a different anodic response occurs depending on the presence of either α-Al, or Al-Si eutectic. Figure 2.23 demonstrates that when an oxide front encounters well-modified silicon particles, the oxide grows around the particles. This is attributed to the current distribution changing in favor of the less resistive adjacent aluminum matrix. As a consequence, the oxide grows around and, eventually, entraps the Si particle. This effect not only leads to a non-uniform oxide layer but also can promote cracks in the oxide and the formation of cavities in the oxide.

These effects were important in understanding the method by which the surface oxide is disrupted on the clad layer. The oxide would share similarities, at a smaller scale, to that in Figure 2.23 due to AA4045 being close to the composition of $AlSi_{10}$. Whether the effect would be as pronounced on the nanometer scale remains to be determined.

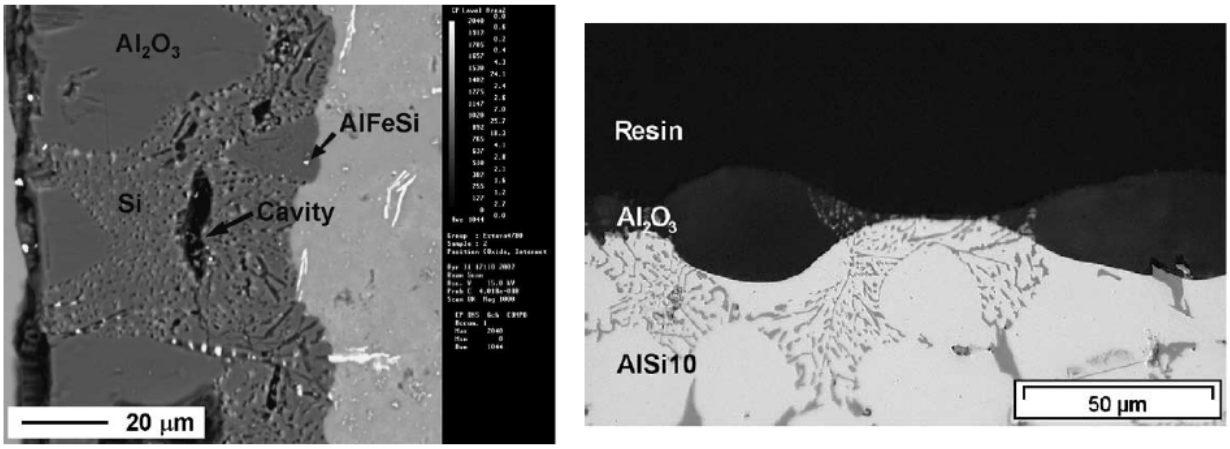

Figure 2-23 - (a) SEM and (b) Optical Cross section of $AlSi_{10}$ substrate Anodized in H_2SO_4, 4.2 A/dm^2, 0°C, for 50 min. [62]

3.0 Differential Scanning Calorimetry

Differential Scanning Calorimetry (DSC) is an analytical method for examining thermal events within a desired sample. These events are measured by the amount of energy necessary to establish a near zero temperature balance between a sample and a reference undergoing the same thermal profile. For reliable values, proper equipment is needed to ensure identical temperature regimes occur in the sample and reference as well as a controlled environment and heating rate [63][64].

Typical thermal events measured in DSC experiments of metals include melting, phase transformations, chemical reactions, and solidification/crystallization. All these metallurgical changes involve the absorption or release of latent heat, L, which can be measured by a thermocouple. Figure 3.1 gives an example of melting of a solid by graphing the enthalpies and Gibbs energies of the solid/liquid material. The free energy of the formation of liquid becomes lower than, and more favorable to, the free energy of solid at point e. This translates to an endothermic absorption of latent heat, L, to reach the enthalpy of the liquid material [64][65].

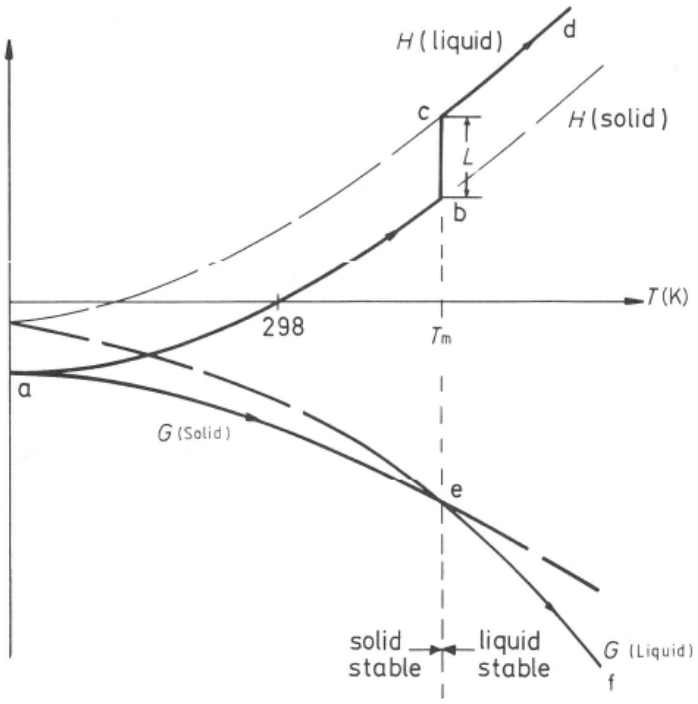

Figure 3-1 - Change in Gibbs Free Energy Upon Melting and Resultant Latent Heat, L [65]

This enthalpy can be represented as,

$$H = \int_{298}^{T} c_p dT \quad \text{or} \quad c_p = \left(\frac{\partial H}{\partial T}\right)_P$$

Such that the slope of a phase's enthalpy with temperature change can be represented as the specific heat of the material in that state [65].

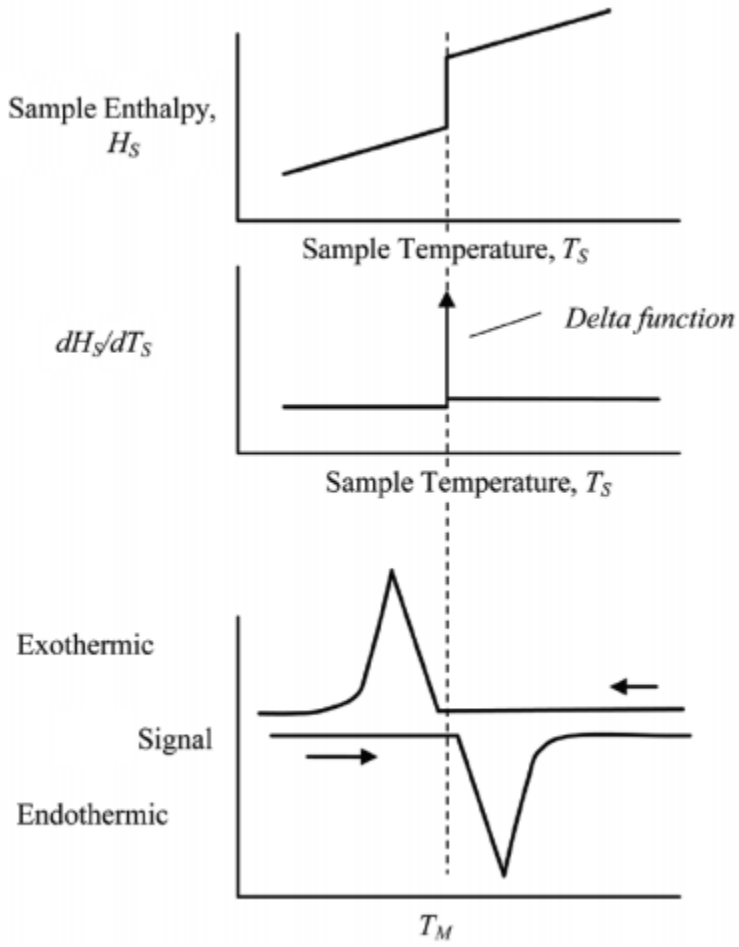

Figure 3-2 - Latent Heat of Melting Converted to DSC signal [66]

This change in enthalpy over temperature can be plotted as shown in Figure 3.2, with a step occurring at some critical temperature, T_M (see Figure 3.1). The increase/decrease in enthalpy can be viewed in the signal output from the DSC as the final bottom diagram demonstrates. The lower curve shows that as T_M is surpassed, melting occurs. The onset of this phase transformation should be seen close to, if not exactly at, the melting temperature depending on heating rates and the presence of thermal lag in the instrumentation. The

curve shows that melting occurs slowly but linearly up to a peak until the entire sample is completely melted upon returning to the baseline. The same holds true for resolidification [63][66].

The layout of a typical DSC consists of two carriers connected to thermocouple junctions placed in a controlled furnace atmosphere, see Figure 3.3. Some calorimeters will have a capillary tube for the carriers to stand on, while others will have them embedded in a chamber in the machine. The carriers hold a reference and sample crucible whose differences in temperature during heating/cooling will be monitored through the carrier to attached thermocouples. These temperature differences are characterized by first order transformations where state functions (ie. temperature) are discontinuous between changes in phases [63][65].

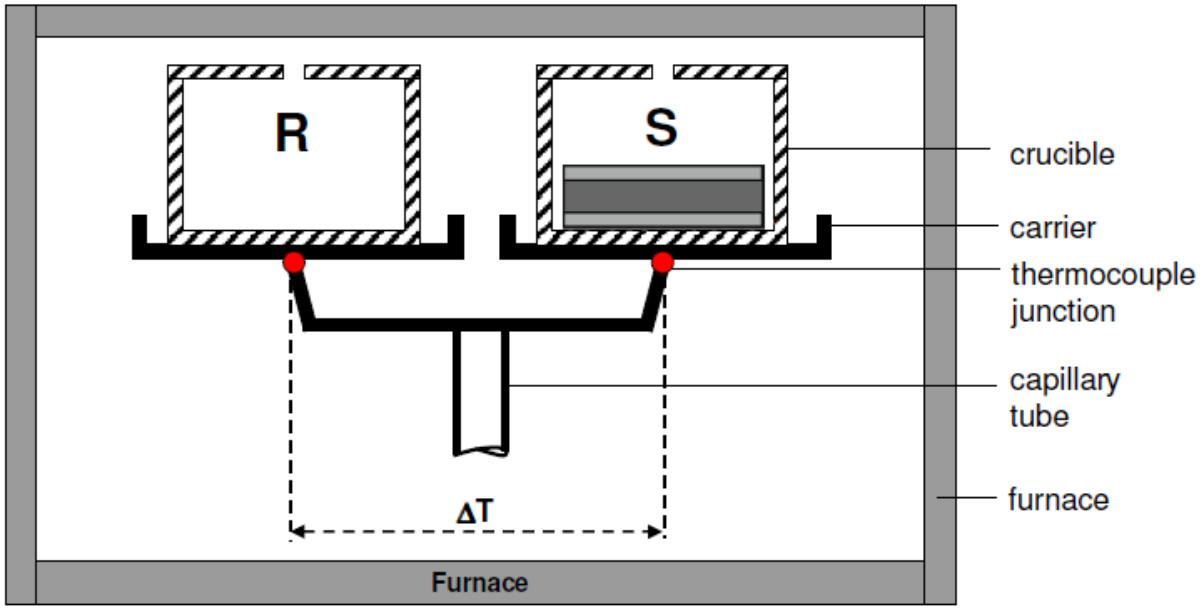

Figure 3-3 - Schematic of Basic DSC Layout [30]

For 1st order transformations, the latent heat evolved is given by Classius-Clapeyron equation. The heat flow rate (dqs/dt) at the carrier base, which holds the sample and reference crucibles, is given for the sample material as,

$$\frac{dq_s}{dt} = \frac{1}{R}(T_H - T_{SM})$$

And the heating rate for the reference pan (dq_r/dt) for the same carrier base is given as,

$$\frac{dq_r}{dt} = \frac{1}{R}(T_H - T_{RM})$$

Where T_H is the temperature of the heat source, R is the carrier and instruments thermal resistance, and T_{SM}, T_{RM} are the temperatures measured by the carrier at the sample and reference pan [64]. Subtracting Equation 3 from Equation 2 gives the difference in temperature of the sample and reference as a function of their respective heat flows,

$$\Delta T = (T_{RM} - T_{SM}) = R \cdot \left(\frac{dq_s}{dt} - \frac{dq_r}{dt}\right)$$

Heat flow to the sample side will heat both the sample and the carrier. This heat flow can be expressed for the sample and reference side as,

$$\frac{dq_s}{dt} = C_{SM}\frac{dT_{SM}}{dt} + C_S\frac{dT_S}{dt}$$

$$\frac{dq_r}{dt} = C_{RM}\frac{dT_{RM}}{dt} + C_R\frac{dT_R}{dt}$$

Where C_{SM} is the heat capacity of the carrier, C_S is the heat capacity of the sample and crucible, and C_{RM} is the heat capacity of the reference crucible [64]. If the carrier is a single solid structure holding both the sample and reference pan, it is assumed that $C_{SM} = C_{RM}$. Also the heating rate is assumed to be uniform across the carrier ($dT_S/dt = dT_R/dt = dT/dt$). However, C_S does not equal C_R due to the reference crucible being empty. From these assumptions, a final equation is derived.

$$\Delta T = (T_{RM} - T_{SM}) = R\frac{dT}{dt}(C_S - C_R)$$

Now the thermal difference of the sample and reference crucible, as measured by the carrier, is a function of the instruments thermal resistance, the heating rate applied, and the difference in specific heats of the sample and reference pans. For actual measurements, C_R is factored out by running a preliminary correction file to factor any effects of the empty sample or reference pans [63][64][66].

Before any samples are used in DSC, a correction file is measured. This is a 'calibrating' run where both the sample and reference crucible are placed on the carrier empty and exposed to a desired temperature regime. This exact same regime will be used when running the DSC with sample. The correction file contains all the information of the specific heats and temperature differences inherent in the two empty crucibles. These differences are factored out during a sample run so that there can be certainty that the data obtained is from actual thermal events [66].

During a thermal event, the measured output of the sample crucible is affected by the samples enthalpy and the DSC trace will deviate from a flat baseline to form a peak (see Figure 3.2). This enthalpy change (ΔH) is measured in the software by,

$$\Delta H = A\left(\frac{K}{m}\right)$$

Where A is the integrated area under this peak, K is the enthalpy calibration constant, and m is the sample mass. A peak in the endothermic direction is termed an endotherm and in the opposite direction an exotherm [64]. To measure the areas under these peaks a straight baseline is necessary. However, a samples specific heat may change after a thermal event and the baseline may shift. The correction file can be used to lower this thermal drift [64][66].

Measured peaks are characterized by their onset temperature, peak height, and the associated area under them. The onset temperature and peak height can be referenced to

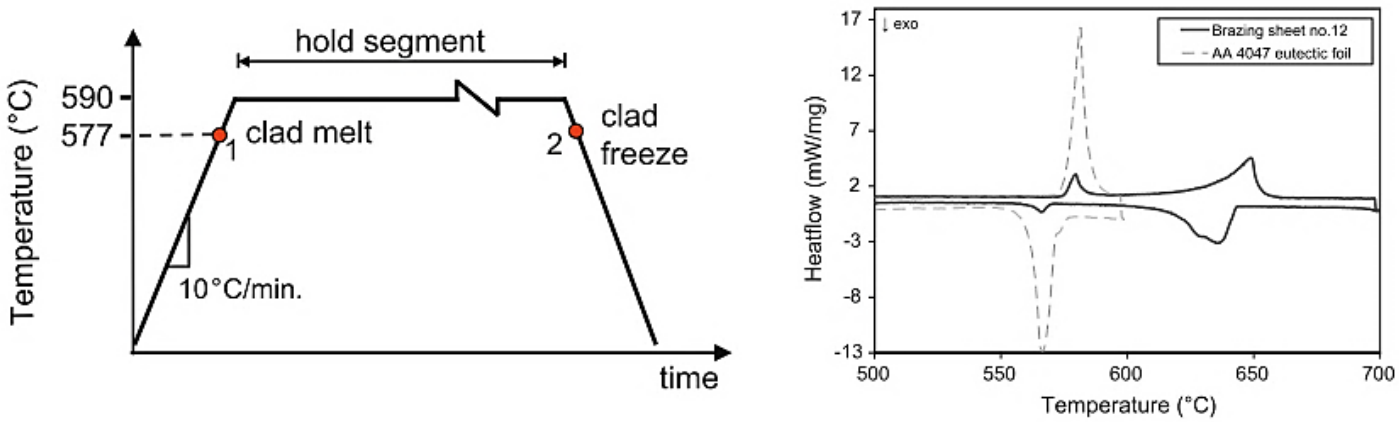

Figure 3-4 - (a) Example of Temperature Profile run in DSC program, (b) Example of DSC Results for Stock Braze Sheet and AA4047 Foil [30]

a phase diagram and the integrated area to the associated enthalpy.

Further discussion of the instrumentation in the DSC has been reserved for the methodology section. Figure 3.4a shows a temperature profile for a DSC run of automotive braze sheet designed to melt the clad layer at various isothermal hold times at 590°C. The heating rate to this desired temperature is important in achieving good results as a high thermal rate will increase temperature lag and lower the accuracy of measured temperatures and enthalpies [66]. Typical heating rates are between 5 and 20˚C/min (or K/min).

DSC results are displayed as heat flow against temperature or time, see Figure 3.4b. As mentioned above, thermal events result in observable peaks on the DSC 'trace'. Typical orientation for these charts is that the heating curve will be on the top and the curve tracing underneath and back to room temperature. The heating curve of AA4047 foil shows a large endotherm peaking at approximately 577°C (eutectic melting point of Al-Si). Likewise the initiation of solidification on the cooling curve underneath is also at this temperature. Several phase changes can be observed for the braze sheet on the same curve which are better explained in the literature [30].

3.1 Ni Modified Brazing Sheets and Differential Scanning Calorimetry

The study of automotive braze sheet joining through DSC is a relatively new technique referenced in the literature, primarily by Corbin et al. [30][36][67]. This includes monitoring and quantifying isothermal solidification and diffusional events of silicon within the sheet, as well as characterization of Dana Canada's nickel modified braze layer. This thesis is a continuation of an ongoing NSERC project examining Dana's that began with Corbin et al. examination of diffusional solidification of the clad layer [30].

As mentioned previously, the amount of liquid formed and its duration are determined by clad composition, peak brazing temperature, and interaction at the clad/core interface. Insufficient liquid will lead to a discontinuous joint which will lead to leakage, reduced mechanical integrity, and ultimately joint failure. At the same time, excess liquid can flow

and pool non-uniformly in fillet regions of the sheet assembly causing local core dissolution and leaving large α-Al residue zones [32][36]. It was noted that solid state interdiffusion at the clad/core interface was also a cause for Si depletion and liquid suppression above the eutectic [30].

Isothermal tests in the DSC, see Figure 3.5, were conducted to show that diffusional solidification of the clad layer was a slow process (even more so in the solid state) and not highly exothermic with respect to typical melting/solidification transformations [30]. The enthalpies of solidification (freezing exotherms) measured showed diminishing values at longer isothermal hold times at 590°C. The same holds true for the enthalpies of melting, as over time increasing α-Al is all that remains in the clad layer (which does not melt until 660°C). The trend of these enthalpies was shown to be parabolic with time, which was consistent with literature on the process of isothermal solidification at a solid/liquid interface (see Figure 3.5a) [67].

Microstructural work halted at temperatures prior to melting (i.e. 575°C) showed evidence of significant silicon particle coarsening and early formation of Al-Si eutectic. The quality of the metallurgical bond of the clad/core was examined to see if oxides/impurities in the roll bonded surface be the cause of slowed solid state diffusion. It was found that holding braze sheet samples after as long as eight hours at 500°C showed only a 3.3 wt% decrease of silicon from the clad. This small loss in composition was attributed not to a poor quality

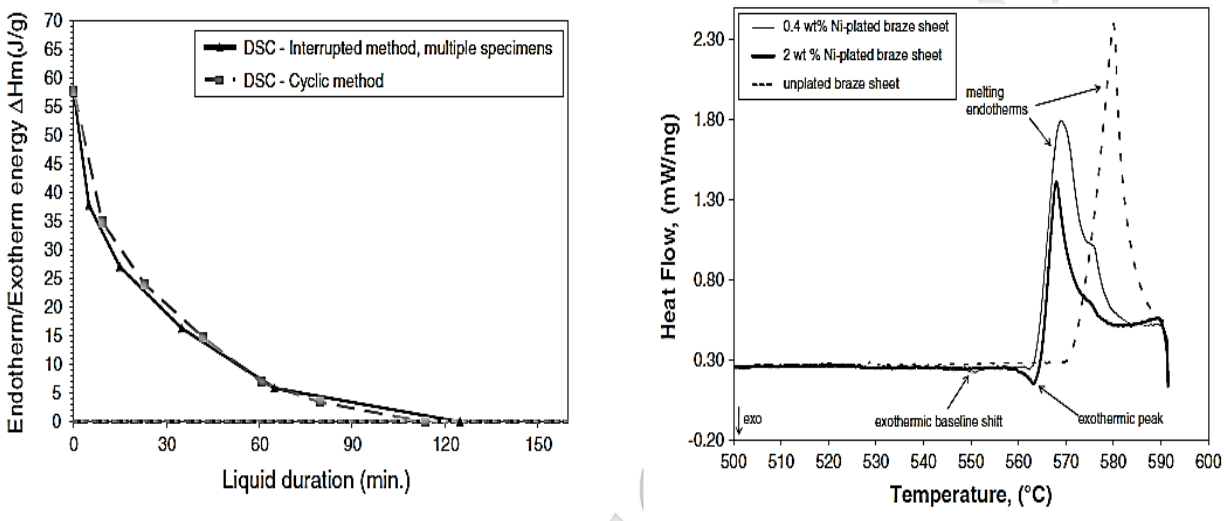

Figure 3-5 - (a) Diminishing Enthalpy of Clad Layer Melting/Solidification with Increasing Duration of Time held at Liquid, (b) Observance of Nickel Intermetallic Formation Exotherm during Heating [67]

metallurgically bonded interface, but solely to the slow rate of solid state diffusion. It was also observed that depreciation of silicon from the liquid/core layer led to epitaxial growth of α-Al into the liquid. A clad layer of roughly 50μm showed complete diffusional solidification after 120 minutes at 590°C [25].

The nickel modified layer on Dana's braze sheets has been examined previously under DSC as well [67]. For thicker layers of nickel deposited on the clad sheet surface a large exotherm could be seen prior to the melting of Al-Si eutectic, see Figure 3.5b. The heat of intermetallic formation, 3Al + Ni = Al_3Ni, was found to initiate around 563°C. This is consistent with the ternary melt mentioned in Section 2.3.1, (Al) + (Si) + Al_3Ni = L, which occurs at 565°C. It was found that solid state formation of Al_3Ni was necessary to accommodate the ternary melt formula prior to melting. If the nickel layer was thin enough, measured under XRF to be 0.4 wt%, then the observed exotherm is almost zero (Figure 3.5b).

Any formation of Al_3Ni in the solid state will reduce the magnitude of the exothermic reaction taking place upon melting. This in effect reduces the amount of pure nickel left on the surface, which will react predominantly with molten clad that has broken through the oxide. This was observed during halted tests where samples were only heated to 561°C, see Figure 3.6a. The surface had roughened from the reaction, but large portions of nickel further from the surface remained intact. Further intrusion of the intermetallic layer could be seen at 563°C where complete solid state reaction had occurred, see Figure 3.6b.

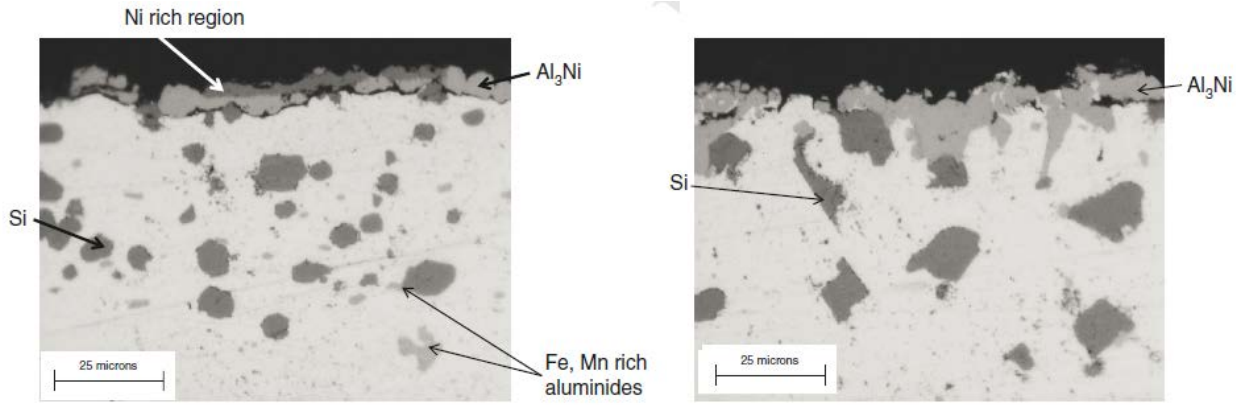

Figure 3-6 - DSC Heating of Nickel Modified Braze Sheet to (a) 561°C (b) 563°C [44]

Appendix B shows the microstructures of samples brought to 570°C and 590°C, respectively, and subsequently cooled. The microstructure indicated that the nickel wt% had very little effect on the overall microstructure once a full liquid was established [67]. The nickel reaction to Al_3Ni was found to be a one-time irreversible reaction. Isothermal solidification of silicon was not significantly altered by the presence of nickel on the surface; however, it was found that a persistent liquid remained present beyond 220 minutes of liquid duration. In other words, the complete diffusional solidification observed in non-coated material, where the liquid fraction tends to zero, was not observed in the coated materials. This was attributed to a required phase equilibria between the solid phase and ternary melt to accommodate the lack of nickel solubility in aluminum [67].

The steps observed from DSC traces and microstructure for the reaction involved; a pre-combustion stage where solid state formation of Al_3Ni occurs, an exothermic reaction initiated by formation of the liquid phase due to eutectic reaction $Al + Al_3Ni = L$, finally the reaction of liquid aluminum and solid nickel to form intermetallics at the surface [67]. The method by which nickel can form solid state reactions with aluminum across the oxide layer has yet to be explained.

4.0 Experimental Methods

4.1 Materials

All brazing sheet materials used for this thesis were chosen and supplied by Dana Canada out of its research and development facility located in Oakville, ON. Table 4.1 outlines the materials received at the start of this project. Braze sheets were clad with AA4045 on one side accounting for 9% of the total braze sheet thickness. All braze sheets were roughly 8.5" x 11".

Table 4-1 - Materials from Dana Canada

Braze Sheet	Gauge	Nominal Clad %	Plating Variability
3003/4045	0.008"	9	A,B,C

To examine the effects of variations in the nickel modified layer, three single side clad 3003/4045 braze sheets were plated. These exact process variations were not disclosed and the importance of this study lay more in how these sheets varied than in their exact origin. None of the plated sheets were analyzed for chemical composition other than to verify the original plated nickel from its formed intermetallics.

Samples were electroplated on a reel to reel system with the braze sheet moving in parallel with the roll direction of the sheet. Recall that the roll direction is the imprint left in the sheet from the final step of cold rolling during production. Following plating, these braze sheets would be stamped and assembled prior to brazing, see Figure 4.1a [5]. To assure uniformity; sections were taken across the width of the sheet for analysis. These sections were designated as Edge 1, Centre, and Edge 2

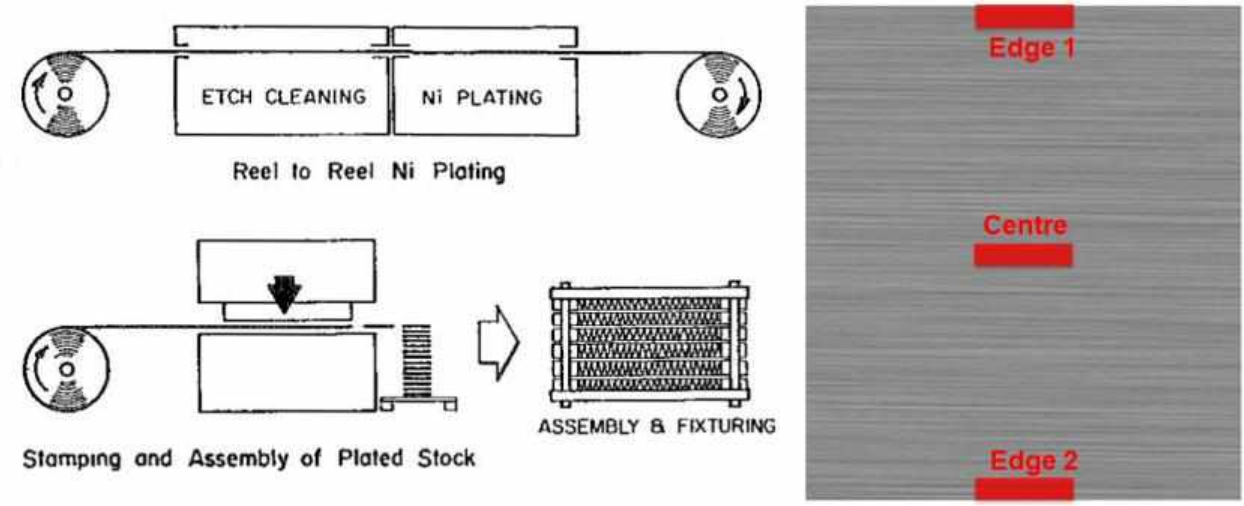

Figure 4-1 - (a) Reel to Reel Process from Braze Sheet to Heat Exchanger [5] (b) Selected Sectioning and Naming Convention for Braze Sheet Sections

4.2 DSC Experiments

There are two types of DSC equipment used in the measuring of heat capacity. Power compensation DSC uses two identical furnaces for the sample and reference. It equalizes the temperatures in both by varying the power input. In these experiments, Heat Flux DSC was implemented which uses a single chamber and the sample and reference are placed in separate alumina crucibles on top of heated disks in the same furnace chamber. This can be seen in Figure 4.2a.

Thermocouples are not embedded in the samples, or even within the crucibles, but are connected to the heating disks. It is important that the temperature difference which may arise between the thermocouple and the sample, or reference, pan be small so that both are exposed to the same temperature profile. This small temperature difference is referred to as thermal lag and develops from thermal resistance between the sample and pan, and also the pan and disk. This can lead to an offset latent heat and transition temperature readings of thermal events which must be considered for any DSC results. The effects of thermal lag can be minimized by lowering the heating rate, dT/dt.

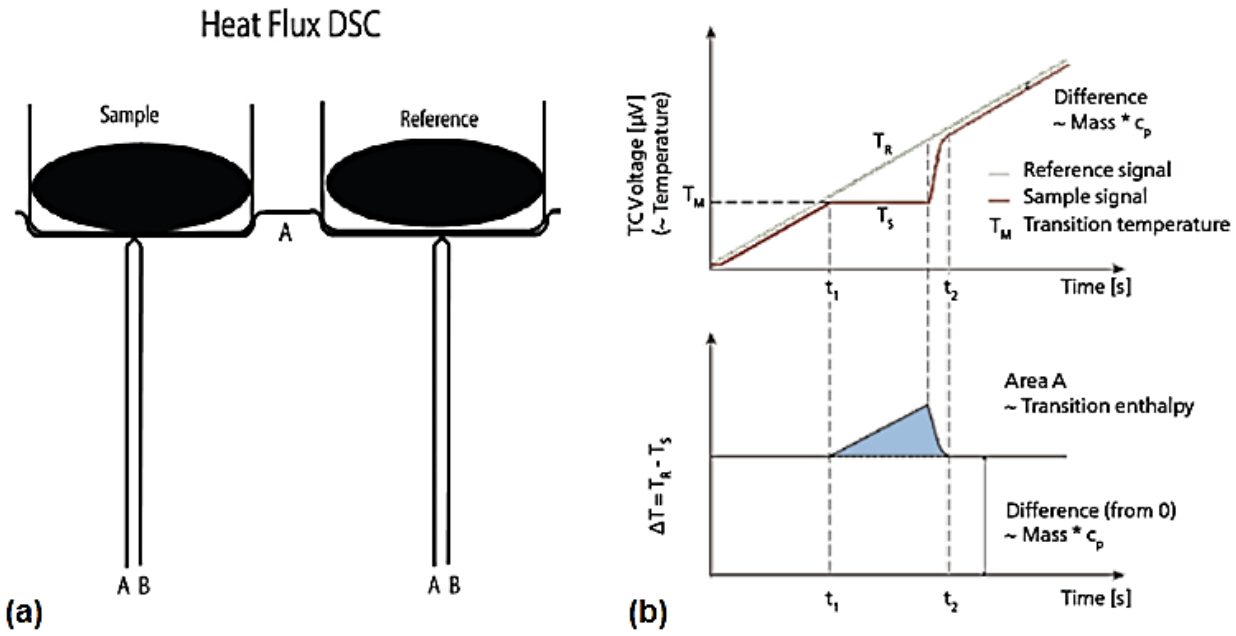

Figure 4-2 - (a) Reference and Sample Orientation in Crucibles on Measuring Head with Thermocouples (b) Temperature Difference between Sample and Reference during Heating yields Calculated Area (Enthalpy) [68]

Recall from section 3.0 that the temperature difference between two crucibles, sample and reference, are measured during a given temperature regime, see Figure 4.2a. Any difference in temperature resulting from a phase transformation will be detected and can be translated into a measured area (enthalpy), see Figure 4.2b. DSC experiments were conducted throughout this project and therefore the methods used for the technique deserve a detailed discussion.

4.2.1 Equipment

The DSC equipment used in the following work consisted of the Netzsch DSC 404c measuring unit as well as a power supply and computer system for data acquisition and storage. These sub-systems are well integrated within the commercial Netzsch DSC package enabling time/temperature controlled experiments, data collection, and data analysis. The system and the sample holder outside of the vacuum chamber can be seen in Figure 4.3. A more in depth schematic can be seen in Appendix C where the vacuum chamber is closed and individual components are outlined.

The sample environment is contained within a tube furnace. The heat-flux measuring head supports the sample and crucible within the hot zone of the tube furnace. This DSC is capable of a maximum temperature of 1500°C and linear heating rates ranging from 0.1-50°C/min. below 1200°C. The furnace can be evacuated to provide a vacuum (10^{-4}mbar) and remove atmospheric contaminants prior to processing [68]. This proved to be important in later experiments in terms of lowering oxygen content to prevent oxidation of nickel.

Static atmospheres can be used as well as dynamic/flowing atmospheres of inert or reducing gases. The shielding gas is supplied from an external gas supply bottle equipped with a two-stage pressure regulator. The gas flow is controlled by an internal solenoid within the DSC and a manual flow control valve, which was set to a flow rate of 150 ml/min. in these experiments. High purity Ar gas (99.998%, grade 4.8 supplied by Praxair) was used as a shielding gas for all experiments.

Figure 4-3 - (a) DSC Measuring Equipment with Controller and Gas Flow Monitor behind (b) Image of Sample Carrier with Alumina Crucibles

Temperature control and heat flow signal acquisition is performed by the TASC 412/3A thermal analysis system controller. The functions of the controller are temperature control and temperature linearization during heating segments. The controller is capable of sample temperature control (STC), which minimizes deviations from the nominal program temperatures via PID control. The temperature resolution is 0.1°C and accuracy is calibrated to within < ±3.0°C using the melting onset temperatures of five elemental standard reference materials (SRMs), namely, indium (In, Tm = 156.6°C), Tin (Sn, Tm = 231.9°C), aluminum (Al, Tm = 660.3°C), silver (Ag, Tm = 961.8°C), and gold (Au, Tm = 1064.2°C) [69].

The sample holder consists of a heat flux measurement head and is supported in the hot zone by an alumina capillary tube on which radiation heat shields are mounted. The DSC-Cp measuring head uses type-S thermocouples (Pt/Pt-10%Rh) with a maximum temperature of 1650°C. The accuracy of this measuring head for specific heat and enthalpy determination are ±2.5% and ±3.0% respectively up to 1400°C. The stated measurement reproducibility of this system is < 1.5% for enthalpy changes and 0.3°C for temperatures below 1000°C [69]. Heat flow baseline reproducibility is < ±2.5 mW.

Sample pans of alumina were used, instead of aluminum pans, due to the use of temperatures approaching 600˚C. The lids of the crucibles were vented to allow exchange of gases between sample and furnace environment. The sensors for heat measurement are located in the measuring head below the crucibles. The enthalpy of any phase transformations during testing is conducted through the crucible and measured by the thermocouples. Although the conductive properties of alumina are not ideal, this thin walled ceramic oxide material is well suited due to operating temperatures and providing the sample an inert containment free of metallurgical interactions with the specimen.

Al_2O_3 crucibles are reusable after cleaning. The cleaning process consisted of soaking for 30 minutes in a hot aqua-regia solution freshly prepared from concentrated acetic and nitric acids in equal parts. The crucibles were then rinsed and ultrasonically cleaned in acetone for 30 minutes. The crucibles were then rinsed in distilled water and then baked in air at 1475°C to burn off any remaining contaminants.

4.2.2 Sample Preparation Techniques

DSC Al_2O_3 crucibles used had a measured height of 4mm and a measured outer diameter of 6.8mm. Supplied brazing sheets ranged from 0.008 - 0.02" and were approximately 8.5 x 11". Sheets were punched, using a punch and die set, to a diameter 0.1875" (4.76 mm). Punched discs were cleaned in acetone, if dirty. Using a Denver Instruments SI-114 scale, the discs were weighed to an accuracy of 0.0001g. An average 0.008" thick punched disc weighed 10.0 ± 0.1 mg. The weights of samples and crucibles were entered into the DSC software prior to sample testing.

4.2.3 DSC Operation and Temperature Programs

Individual experiments were first set up using a personal computer that uses an IEEE 488 interface connection with the TASC 413/3A DSC controller. Temperature segments, shielding gas conditions and instrument settings are programmed via a Netzsch DSC-specific graphic user interface. Netzsch Thermal Analysis Data software (version 6.0) is also used for data interpretation and analysis.

Any temperature profile test requires a correction file to remove background instrumental and crucible effects from the experimental results. Figure 4.4 illustrates the temperature programs used for all brazing sheet tests. Initial tests involved a simple profile that went to the peak brazing temperature 590°C and then cooled back to room temperature at 10K/min. This test was later modified to allow faster trials and minimize solid state diffusion by ramping up to 500°C at 20K/min before transitioning to 10K/min, see Figure 4.5. The second, third and fourth trials were similar to work done by Corbin et al. [30] Isothermal holds were conducted at hold times from 2-15 minutes at 590°C to better understand the liquid duration of the braze sheets. Figure 4.4c shows a pre-melt and soak test which was later modified to an initial temperature of 565°C in an effort to react all the surface nickel and isolate the initial melting endotherm. Finally, cyclic testing was done to achieve multiple

data points to model the rate of isothermal solidification and liquid duration. Data acquisition rates were set at 1 pt./s during all athermal and isothermal segments.

Before a DSC experiment can be conducted, a correction file must be generated by performing a DSC trial using the desired temperature program in the absence of the physical sample (sample crucible is empty). This is to create a background trace of the thermal behavior of both empty crucibles so that it can be factored out during the actual sample test. The intention is to obtain flatter baselines that are less affected by experimental artifacts which can cause signal shifts. Figure 4.5 illustrates a typical correction file (blue), which was obtained for empty crucibles heated to 590°C and subsequently cooled at a rate of 20K/min to 500°C then 10K/min to 590°C. The corresponding temperature history (red dotted line) and sample trace (green) are also included. As long as the crucibles are sufficiently clean, the crucibles and correction file can be reused for all future sample testing.

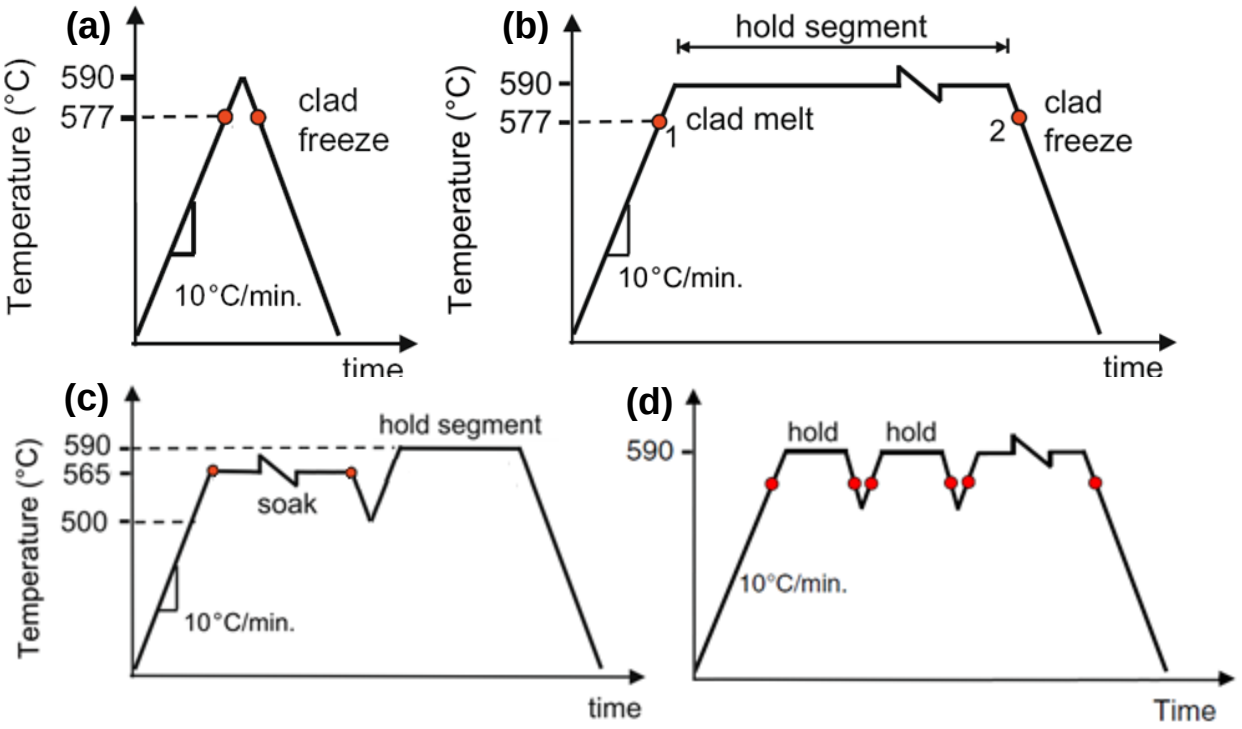

Figure 4-4 - Temperature Profiles used during DSC testing of Braze Sheet (a) Ramp to Peak (b) Isothermal Hold (c) Exohold (d) Cyclic

After the correction file is created, the sample can be loaded into the DSC for the actual run. The braze sheet sample would be placed in the sample crucible and placed adjacent to the empty reference pan. The DSC furnace chamber is then lowered into position, the chamber is pumped down using a mechanical pump, and the chamber is backfilled with Ar purge gas. This pumping and backfilling is typically done twice to ensure that the atmosphere is free of oxygen and as inert as possible. Temperature programs start at 20°C with Ar gas already flowing in. Once a purge gas flow was visually confirmed by the flow control indicator and positive pressure within the furnace chamber was established, the furnace exhaust valve was manually opened. This enabled the dynamic flow of shielding gas and prevented the backfilling of the sample environment with air. The experiment was then started using the control software.

Heat flow traces recorded by the DSC were expressed in mW, or mW/mg based on the sample mass entered at the start of the program. The green curve in figure 4.5 illustrates a typical DSC trace for a braze sheet sample that was heated using the identical temperature program via the previously obtained correction file. The temperature segments and endothermic/exothermic peaks will be further discussed in Section 4.2.4. Once the trial was complete, the samples were examined through detailed metallographic analysis using Optical Microscopy and SEM/EDS.

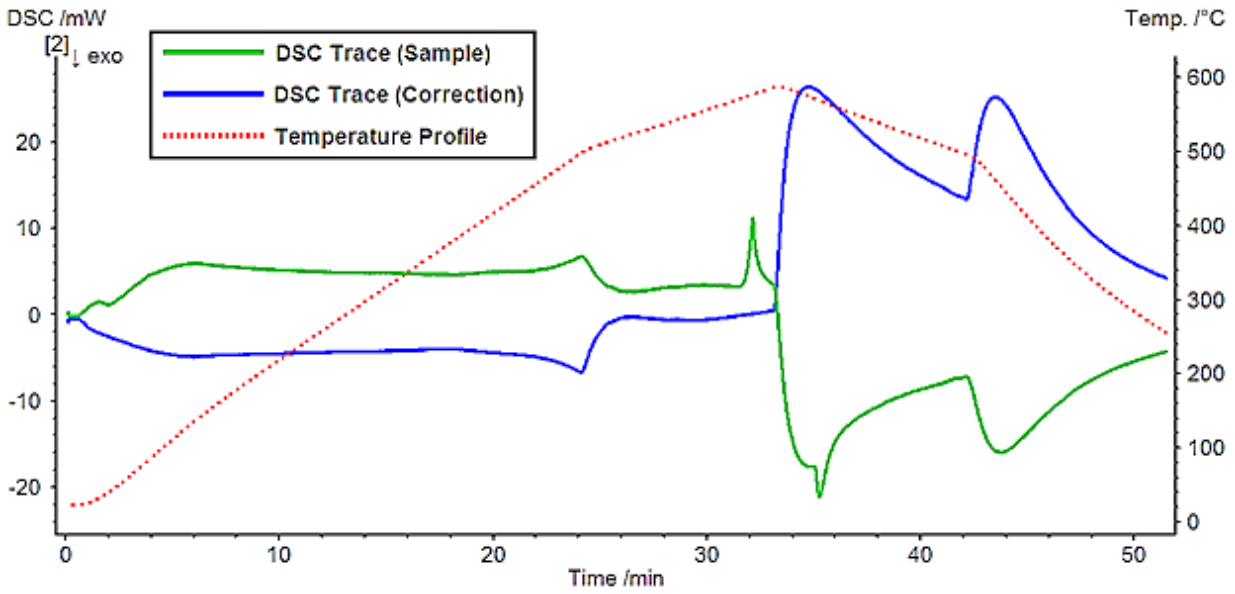

Figure 4-5 - Correction and Sample File run through Temperature Profile shown

4.2.4 Analysis of DSC Results

Following completion of a sample file, the Netzsch Proteus software (version 6.0) was used to measure important values and areas along the DSC trace. Individual segments of DSC traces can be isolated and manipulated for comparison and measurement of important attributes such as reaction onset temperatures and reaction enthalpies. By convention, the exothermic heat flow direction is oriented downwards on the y-axis. Phase transformations such as melting will create positive deviations from the DSC trace baseline, forming endothermic melting peaks (endotherms).

In Figure 4.5, the heating segment of the DSC trace shows some initial drifting at low temperatures due to the rapid heating rate employed. Deviations in the correction and sample traces are visible during the sudden changes in heating rates (dT/dt). The baseline stabilized several minutes following any heat changes in the temperature program. A large endothermic peak, endotherm, is visible at the end of the heat-up segment just before peak braze temperature. The onset of this peak was measured at 577.7°C, which coincides with the Al-Si eutectic point. The cooling curve shows a large exothermic peak, or exotherm, which corresponds to the resolidification of Al-Si eutectic.

To identify temperature-specific phase transition such as melting, the athermal segments of DSC heat flow traces can be plotted as a function of temperature, instead of time such as in Figure 4.5. Figure 4.6 shows ideal melting endotherms that are graphed with temperature on the x-axis. Case 1 illustrates how the onset temperature (T_{onset}) of a melting peak was calculated using Netzsch Proteus software. The onset temperature was determined at the intersection of the extrapolated baseline and peak onset tangent.

The specific heat of the sample determines the position of the DSC baseline, in the absence of a phase transformation [63]. The flat DSC trace for case 1 in Figure 4.6 illustrates how a pure, ideal material will form a flat, continuous baseline parallel, but not equal to, 0 J/g (a value where no samples or crucibles would be present). The baseline can shift following a phase transformation (melting), which is a result of a change in specific heat in the liquid

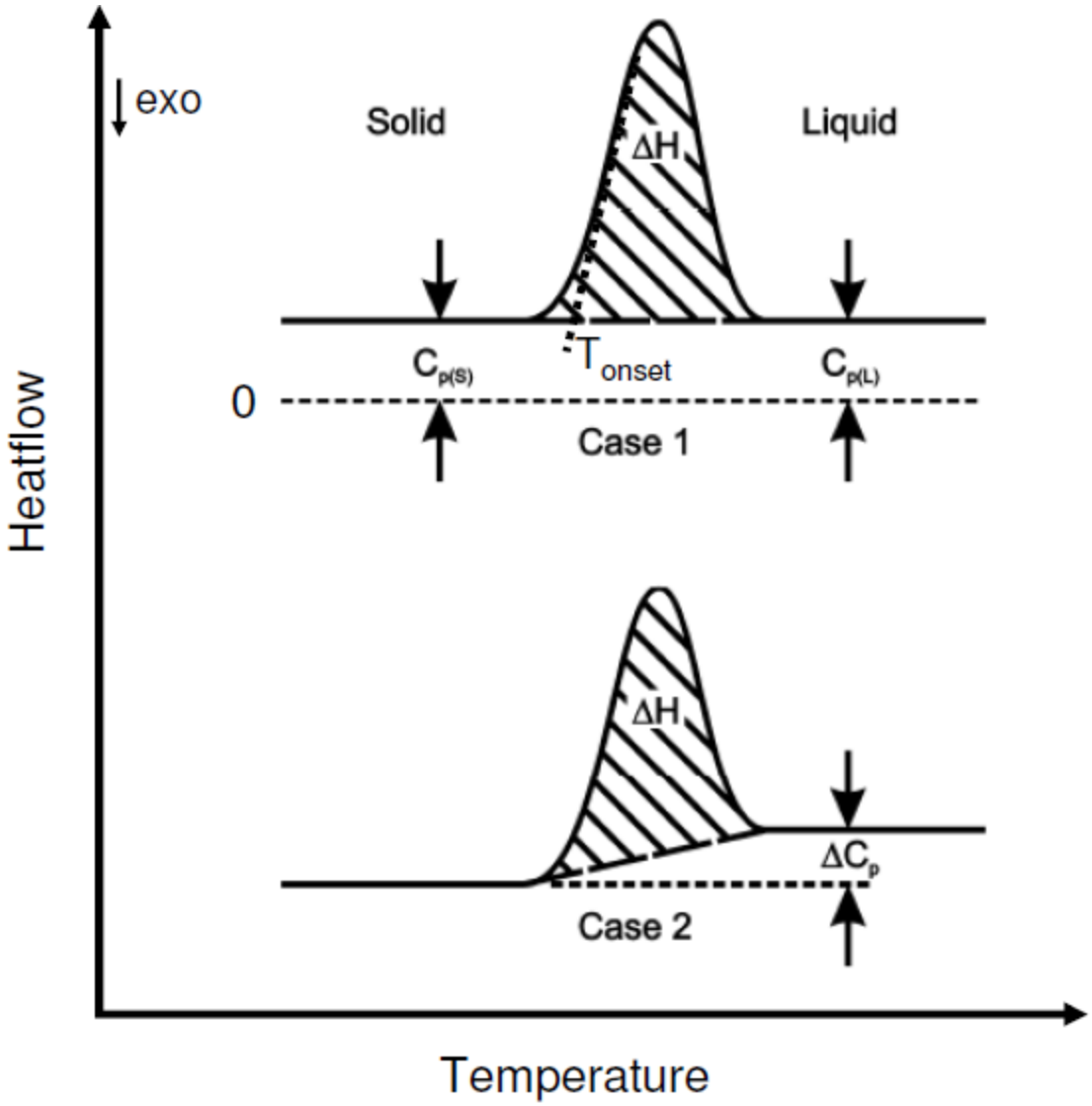

Figure 4-6 - Differences in Specific Heat for the Baseline following Peak [71]

phase. Additionally, improved thermal contact between the new liquid phase and crucible after melting may also contribute to baseline shifting across the melting endotherm [70].

Measuring the area under curves during phase transformations such as intermetallic reactions, melting, or resolidification yields the enthalpy of the transition. The magnitude of this measurement (in J or J/g) can provide an indication of the amount of liquid formed or solidified. It is important to note that the entire sample mass is used to calculate enthalpy values in units of J/g.

In this study, the area of DSC peaks was found by integration using the Netzsch Proteus software. As illustrated in Figure 4.7, there are a variety of methods available for DSC peak integration and baseline interpolation in the presence of baseline shifting across a peak [63]. These include: a) linear, b) tangential sigmoidal, and c) horizontal left or right starting. The integration limits were manually selected and examination of the first and second derivatives of the DSC trace. The start of a peak was considered to be the point where the first and second derivatives began to increase as the DSC trace departed from the baseline. The end of a peak was determined at the point where the second derivative was zero. At this point the slope of the trace is no longer changing and the baseline can be considered to be re-established after the thermal event.

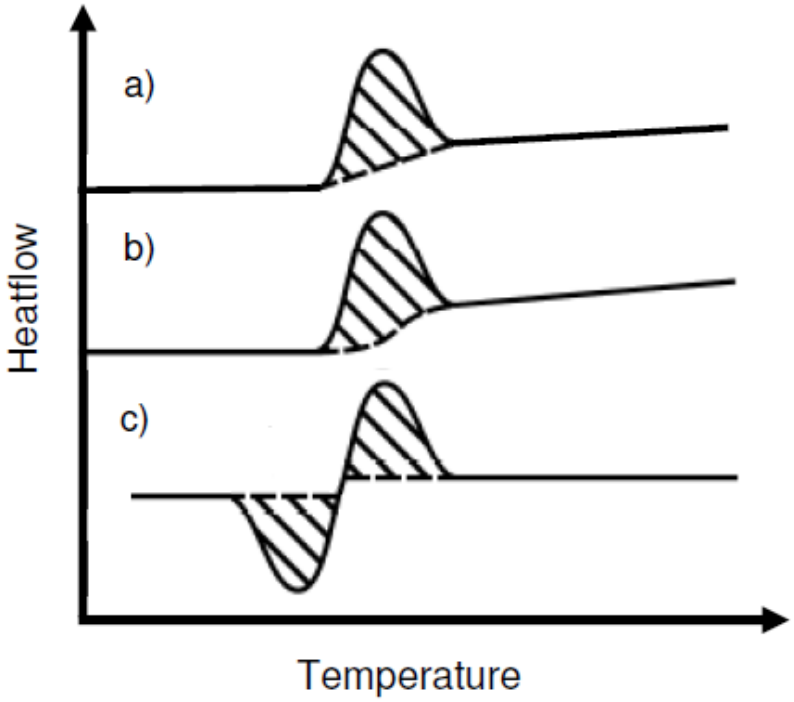

Figure 4-7 - Different Methods of Measuring DSC Peaks [71]

Since the exact nature of baseline shifting across the peak due to thermal contact resistance and CP effects is not well known, a linear interpolation method (a) was used in cases where a stable baseline is available on either side of the peak. For most sample traces, method (b) was implemented for uniformity in the measuring of all endotherms or exotherms. Method (c) was adopted in the case of adjoining peaks. A left horizontal started peak was used when starting from the left of the baseline and right horizontal from the end.

4.3 Metallographic Analysis

As-Received braze sheets were sectioned and examined topographically and cross-sectionally under optical and SEM. Samples punched and run under DSC were further investigated under the same metallographic techniques. Metallographic samples were prepared by typical metallurgical techniques as described below.

4.3.1 Sample Preparation

Following sectioning or DSC experiments, samples were mounted using a metal/plastic clip and mounted in epoxy resin, or conductive bakelite for SEM. Samples were exposed by gradually grinding into the mount until a suitable cross section was revealed. Aluminum, being a soft metal, required excessive care and many polishing/cleaning steps to achieve a satisfactory image (see Table 4.2). In most preparations, a cotton swab was used in between polishing steps to remove any excess dirt or polishing solution. Samples were cleaned thoroughly with deionized water in between each polishing step.

Table 4-2 - Grinding and Polishing Methodology

Step	Surface		Suspension	Lubricant	Time	Force per Sample (N)	RPM	Direction
1	ANSI Grit	320	Water	None	2:00	20	300	>> CW
2		600	Water	None	2:00	20	300	>> CW
3		800	Water	None	3:00	20	300	>> CW
4		1200	Water	None	5:00	20	300	>> CW
5	MD-Mol		3 µm Dia.	E. Glycol	5:00	20	150	>< CCW
6	MD-Nap		1 µm Dia.	E. Glycol	5:00	20	150	>< CCW
7	MD-Chem		Colloidal Silica	None	1:00	20	150	>< CCW

The first three grinding steps were used to reveal the desired cross section of the sample. Following this coarse grinding, a fine grinding step ending either at 1200, or 2400 was adopted. Samples were then thoroughly rinsed in water and dried with compressed air. Polishing began using a 3µm diamond suspension, either a spray or liquid, and ethylene

glycol based lubricant. As a final step, colloidal silica was used immediately followed by a substantial rinse in water. Struers MD grade polishing pads were used during all steps. All samples were examined under an optical microscope for dirt and grit prior to taking any images.

4.3.2 Optical Microscopy

The polished cross sections were viewed under optical microscopy using an Olympus MTV-3 microscope. Images were captured using a digital camera at magnifications ranging from 10-1000X. If necessary, Image-Pro software was implemented for analyzing collected images.

4.3.3 Scanning Electron Microscopy

A JEOL 6460 scanning electron microscope (SEM) was used for high magnification metallographic examination of specimens. A 20kV electron gun acceleration voltage was used. Secondary electron (SE) imaging was used to interpret the morphology and topographical contrast of the sections. This SEM is equipped with an Oxford energy dispersive x-ray spectrometry (EDS) analysis system. EDS was used to quantitatively analyze the chemical composition of the samples at various locations on the cross section

4.4 Methods of Oxide Growth

In the second half of the project, the mechanism by which the oxide was disrupted and molten clad flow exuded onto the surface was to be studied. For this mechanism to be examined, it was necessary to gain an understanding of the surface oxide composition and structure. Recall that aluminum and, to a lesser extent, aluminum oxide naturally passivates in open air and forms a layer on the order of 10nm. Knowledge of the natural amorphous layer allowed for the creation of analogue surface layers to begin testing its role as a barrier to the nickel aluminide reaction.

Section 2.5.1 discusses the chosen techniques used to simulate the surface oxide layer, that is, thermally, anodically, and chemically. Thermal trials kept under 400-450°C, as well as anodic trials under 50V, were able to avoid a crystalline formation of γ-alumina. Chemical trials were not part of the initial experimentation but more so a byproduct of surface preparation. When the oxidizing behavior of nitric acid was discovered, chemical trials were included as a method for amorphous oxide growth.

4.4.1 Initial Experiments and Methodology

Following the selection of measurement and growth techniques, work began on experimental setup for initial oxide growth measurements. Literature consulted provided a guide to experimental standards that were used in previous thermal and anodic oxide growth testing. From this, major experimental parameters were outlined for each oxide growth method which included:

Thermal Oxide Growth
- Temperature (Growth rate/Structure)
- Time (Thickness)

Anodic Barrier Growth
- Formation Voltage
- Current Density (f(Voltage), Structure, Thick.)
- Time (Thickness)
- Electrolyte Concentration

Anodic Porous Growth
- Formation Voltage (Porous Cell Shape)
- Electrolyte Concentration/Temperature
- Current Density (Similar to Barrier)
- Porous Cell Structure (Size/Width)

Other (Sample Preparation, Equipment used, etc.)

Sample preparation was another important factor, especially in the case of anodic oxide growth. Samples were typically chemically, or electrochemically, altered to ensure a clean, uniform surface for the oxide to grow from. Imperfections on the surface could induce imperfections in the oxide layer leading to cracking, or cause a preferential leakage site for current. From several papers [51-62], all preparation techniques were assembled and are listed below:

Sample Preparation Techniques

- Mechanical Grind/Polish (400/800/1200 Grit, 6/3/1 μm Polish, Colloidal Silica) [62]
- Chemical Polish (NaOH, HNO_3, H_3PO_4) [53][61]
- Ultrasonic Cleaning (Ethanol, Isopropanol) [51][62]
- Electropolish ($HClO_4/CH_4O$, $HClO_4/C_2H_4O_2$) [58][59]
- Heat Treatment (350-500˚C, Anneal Aluminum Surface, Finer Grain Structure Anodizes Better) [61][62]

All the techniques listed above were pulled from technical papers creating barrier/porous type anodic alumina on 4-5N purity aluminum. In a paper by Fratila-Apachitei et al. Al-10Si was used as the substrate and here the samples were ground/polished and then ultrasonically cleaned [62]. For this study, a two-stage chemical treatment of the alloy surface involving [72]:

Exposure to 10% NaOH (aq.)

$$Al_2O_3 + 6NaOH \rightarrow 2Al(OH)_3 + 3Na_2O$$
$$NaOH + Al \rightarrow NaAlO_2\,(Smut) + H_2$$

- Removal of Existing Oxide
- Exposure of underlying Si, Fe, Mn, Mg Precipitates
- Buildup of Smut Layer

Exposure to 68% HNO_3 + Further Oxidant (Fe^{3+}, HF)

$$NaAlO_2 + HNO_3 \rightarrow NaNO_3 + HAlO_2$$
$$M(Fe, Mn, Si)^{x+} + HNO_3 \rightarrow M(NO_3)_x + H_2O$$
$$SiO_2 + HF \rightarrow SiF_4 + H_2 \text{ (if HF added)}$$

- Neutralize Surface Smut
- Oxidation of Alloying Elements
- HF Needed to Remove SiO_2

An experimental setup was arranged to conduct anodizing experiments of the aluminum sheet. Figure 4.8 includes all the equipment used to facilitate anodizing. In the first few initial trials, a single side cathode was used in a beaker but was quickly replaced by a stainless steel pan which allowed double sided anodizing. The power supply used had a maximum output of 48V. The power supply only had a single radial dial for control of voltage; current could only be monitored in these experiments.

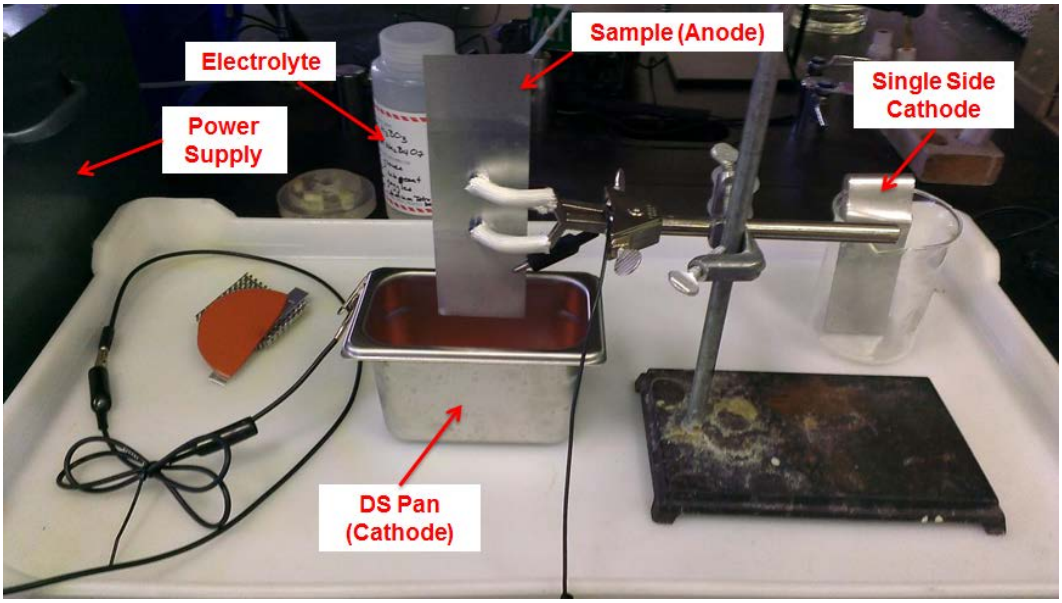

Figure 4-8 - Experimental Setup for Anodization Experimentation

Finally, the choice of electrolyte was needed for both porous and barrier type. Some properties that were to be considered were anion incorporation from the electrolyte into the oxide (which can affect oxide behavior/structure), electrolyte aggressiveness (which affects the existence and size of porous cells), and thicknesses achievable at low voltages. A matrix was created for barrier and porous type electrolytes which looked at variables such as applied voltage, electrolyte temperature/concentration/aggressiveness, anodizing ratios, porous cell parameters, and environment, health and safety considerations. Some values, such as total film thickness, were not clearly stated in the papers. For barrier type anodizing, a boric acid/borax solution was used and for porous type anodizing a phosphoric acid solution was selected.

Thermal tests were much simpler, involving only a sample sheet and an oven. Samples were not surface prepared in any way but simply placed in the oven where their natural oxide would grow with time. Some issues that were considered were keeping the braze sheet at a temperature well below liquidus, or avoiding where microstructural changes could occur, and avoiding a change in oxide morphology to a crystalline structure. Ovens were used within Dana facilities and samples were readily exposed to open air within the oven.

Following oxide growth, by whichever method, samples were cleaned in DI water and dried. They were then taken and examined under optical microscopy. Surface images were taken at varying magnifications and documented. Some samples were sectioned and examined under optical microscopy (with limited results due to the small thickness of the oxide). Other samples were sectioned and examined under SEM, FIB-SEM, and FTIR.

4.4.2 Oxide Growth Results

Once the experimental setup had been devised, oxide trials began using a barrier type solution. The solution was a mixture of both 0.5M anhydrous boric acid (H_3BO_3) and 0.05M anhydrous sodium tetraborate ($Na_2B_4O_7$). The solution was mixed together with deionized water in a large beaker and transferred to a 1L plastic container. The solution needed to remain near neutral to have the effect of creating a barrier type oxide layer. This neutral pH level ensured that the mixture was not aggressive enough to promote a porous layer forming on top of the barrier. From literature, the mixture was used with voltages of 20-1000V, a current density of 25A/m2, and at a temperature of 25˚C. This mixture was documented as having an anodize ratio of 14Å/V and, with an applied voltage of around 48V, was expected to yield a 65nm barrier layer [51].

Several trials were conducted using a single side cathode. Figure 4.9 below shows the results of anodizing with no surface preparation. This was a single side cathode trial where

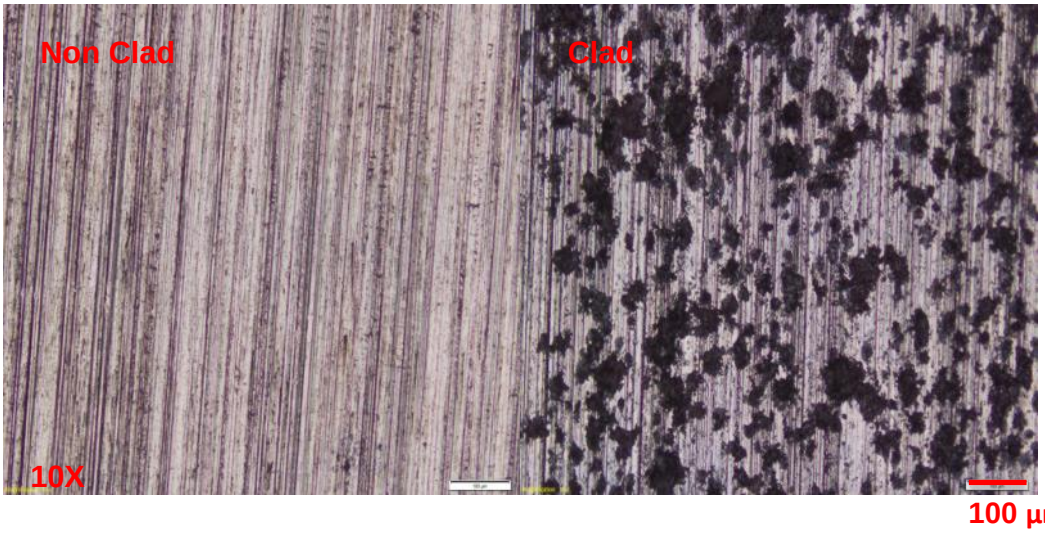

Figure 4-9 - Surface Images (200x) of Anodizing of Clad Layer without Chemical Surface Treatment

the clad side seems to be 'burning' the sheet (see section 2.5.3) which has been observed in anodizing trials conducted in other anodizing processes of Al-Si [62]. In all surface images, the striations from the previous roll fabrication of the sheet could be observed indicating the roll direction.

At this point chemical treatment was adopted. This consisted of 1-2 min. exposure in an aqueous NaOH solution as described above, followed by 2 min. in a HNO_3 mixture. This result proved effective in initiating actual anodization, though still not on the clad side. At this point, the double sided pan was used exclusively for all trials so far. It became clear that anodization was still not occurring on the clad side of the braze sheet due to the presence of silicon.

It was decided to use chemical methods to remove the surface silicon which was inhibiting uniform, proper anodizing of the surface. Varying levels of HF were used in a HNO_3 diluted DI water mixture which was made solely for these trials. It was not until concentrated levels of these two acids were used that any true removal of silicon was obvious. Figure 4.10 and 4.11 shows the results of anodizing with nitric acid mentioned above (left figure) and later with a concentrated nitric/hydrofluoric acid mixture (right figure).

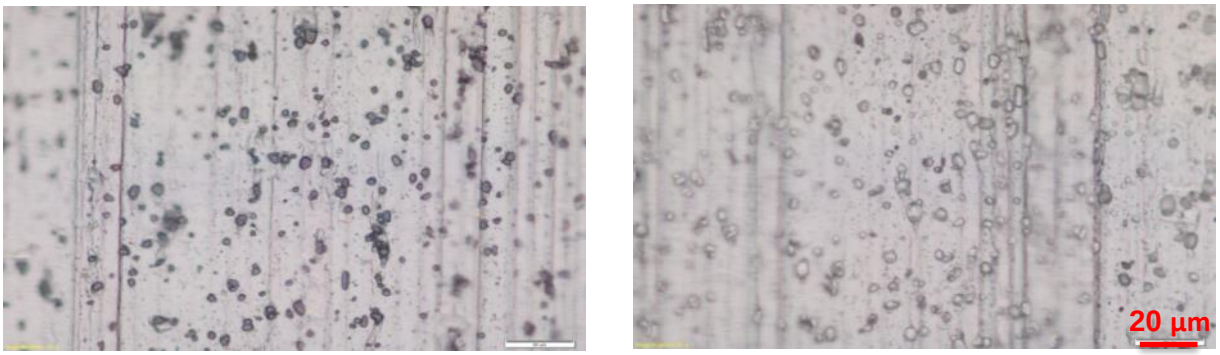

Figure 4-10 - Surface Images (500x) showing the Removal of Surface Silicon

Once the silicon had been removed, it became clear that both sides of the surface had been anodized. This was confirmed partially through an optical surface viewing, though mostly by using a two point resistance test with a multimeter. The oxide as a whole provides a barrier to further current flow and so would show no resistance value on the meter.

Applying the same technique to an as received sample would show resistances around 4-6μΩ/cm.

Another method of verifying the oxide was to monitor the process itself. When anodizing it was important to set the voltage to the desired value before the power supply was turned on. This helped ensure uniformity in the oxide layer and to maintain consistent results. Once the power supply was switched on a spike in current is observed which represents the respective current through the sample relative to the voltage applied. However immediately after, the current drops which coincides with the development, and continuous growth, of oxide. Eventually a steady state is reached which is assumed to be the equilibrium exchange in ionic transport of Al^{3+} and O^{2-} through the oxide layer. If this drop was not significant and did not lie close to zero amps, it was assumed that one side, or both, was not anodizing. [57]

During the anodization process, oxygen is evolved at the surface of the anode and it is this evolved oxygen that is the main source for the growth of the oxide layer. If during anodization the evolution of oxygen is observable on the surface. It was another indicator that the oxide layer was not being formed.

With a proper surface treatment and method of anodic growth, samples were prepared for characterization purposes to examine their thickness and consistency. Optical methods did not have the resolution capabilities of observing the oxide, with a best attempted measurement of 884nm (more than 10 times the estimated 65nm from anodization ratios). It

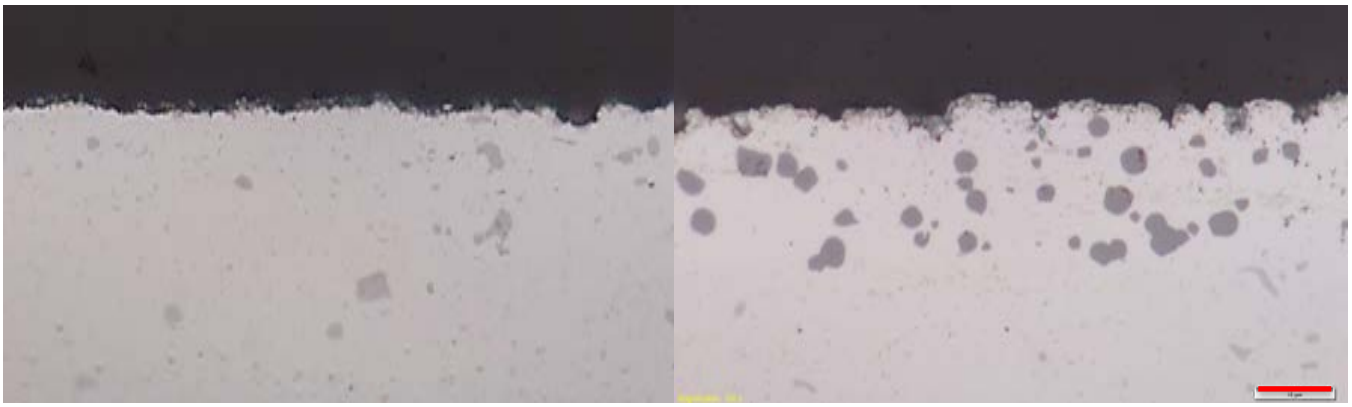

Figure 4-11 - Cross Sectional Images (1000x) of Core (left) and Clad (right) layers following Hydroflouric Acid Treatment

became clear that SEM/FIB-SEM/TEM imaging were a necessity.

Figure 4.11 shows the 1000X optical images of the nonclad/clad layers after surface preparation (1 min NaOH, 5min HNO3 + HF(c)) and barrier type anodization (Boric Solution, 40V, 5min). The surface on the clad side had roughened due to hydrofluoric acids preferential removal of the silicon on the surface. A surface layer is observable and the results of measurement were mentioned above. Some papers had advised measuring samples at an angle when measuring the oxide layer, but it was assumed that the oxide layer was too thin to measure accurately by optical microscopy.

For the thermal growth trials a temperature of 350˚C was chosen. This temperature was below the values typical of heat treatment for the clad layer (AA4045), 380-520˚C, and would not promote any crystalline growth within the oxide. Therefore, the oxide would be amorphous in nature and roughly analogous to a naturally grown aluminum oxide. The braze sheet was cut into a 2” x 8.5” rectangular strip which was bent to a 90˚ angle so that the strip could be placed on its side in the oven. The strip was left at 350˚C for 24 hours to ensure a thick thermally grown oxide was produced.

All samples were examined under FIB-SEM and measured at roughly 20,000X. Figure 4.12 shows the results of sample D from FIB-SEM. The image shows the clad surface consisting of the grain structure and silicon/intermetallic particles. The surface had been sputtered with a gold layer seen on top of the oxide (white layer). The operator has zoomed in to achieve the oxide layer measurements and then panned back out to get the overall surface image. The value of 65nm estimated from the anodize ratio of 14Å/V proved highly accurate. The oxide layer is continuous and uniformly thick within the tolerance of ±1nm from the measurements taken. One other important thing to note is the grain structure itself. Typically a fabricated braze sheet contains a finer grain structure near the surface as imparted by the rolling process. Here it would appear that a large portion of those finer grains have been chemically removed. This would contribute to a less uniform oxide layer over the surface as outlined in literature [62].

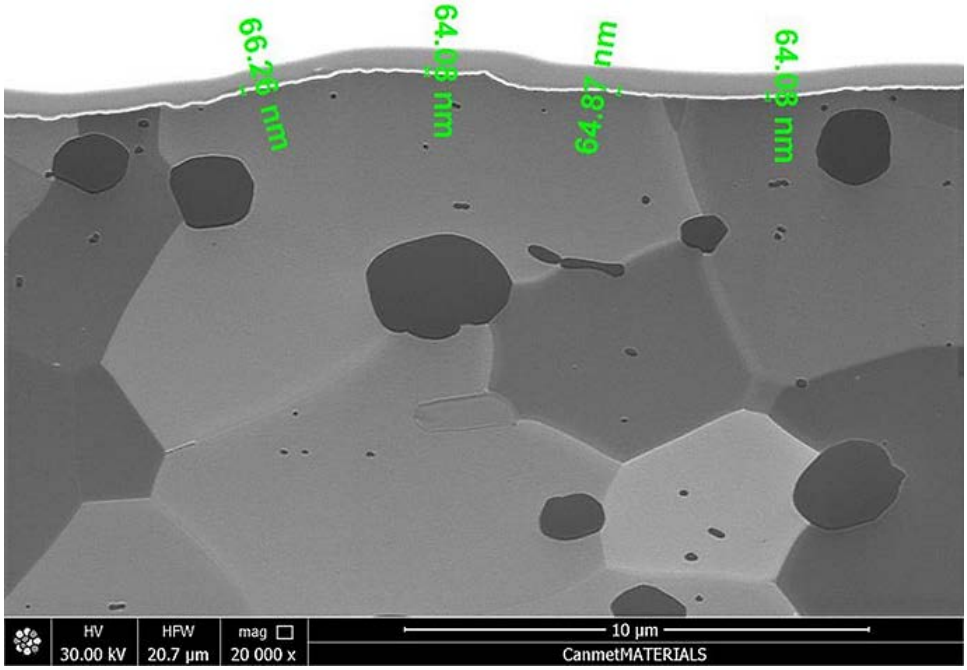

Figure 4-12 - FIB-SEM Image of Clad Layer Cross Section showing Measured Oxide Layer (in White) (Courtesy of Dana Canada)

Sample D showed the thickest oxide layer with roughly 65nm grown on the surface. In decreasing order, sample B showed a layer of 43 nm, sample C a layer of 40nm, and sample A was ambiguously found to be 10-20nm. The measurements were taken at a much higher magnification than what is shown in the figure, and then the image was taken after for reference. The measurements were in line with what was expected of the oxide measurements. However, sample B proved surprising in its thickness. It was expected that this sample would more likely coincide with that of sample A due to no growth technique being applied. This is when it was discovered that nitric acid was actually increasing the thickness of the surface oxide.

Surface chemistry results were extracted from work involving SEM. Figure 4.13 consists of surface shots from SEM of sample A, B, C, and D on the clad side. Recall samples B and D have had their surface silicon removed. Five areas on the surface were selected and measured using energy dispersive x-ray spectroscopy (EDX). The results are included in Table 4.3. A charted version is available in Appendix E which includes the standard deviations for each run.

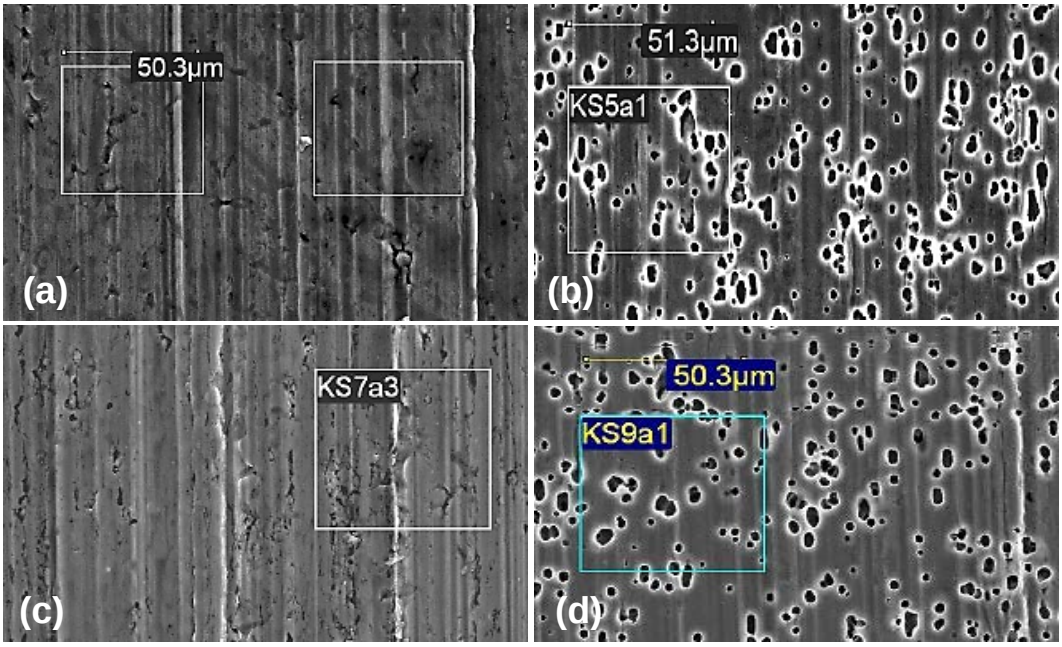

Figure 4-13 - SEM-EDX Surface Shots of Sample A, B, C, and D on the Clad Side (Courtesy of Dana Canada)

There is a marked decrease in the amount of carbon present on the clad surface following each treatment. Carbon is most likely from residual hydrocarbons such as oil, lubricant, or dirt. Surface treatment most likely chemically removed some of this carbon away and thermal oxide growth may have covered the carbon to lower EDX detection. An increase in fluorine is noticed in the B-Clad from the use of HF in surface preparation, and is likely 'masked' to some extent in the D-Clad which received the same treatment. Silicon levels drop by a factor of 5-6 from the surface treatment which can be seen in the cavities of sample B and D in Figure 4.13.

Table 4-3 - Elemental Composition (wt%) of Core and Clad side for Samples A, B, C, and D under SEM-EDX (Courtesy of Dana Canada)

	C	O	F	Al	Si	Total
A - Clad	9.3	0.9	0.7	86.4	10.4	107.7
B - Clad	4.7	1.0	1.1	93.8	2.2	102.8
C - Clad	3	1.8	0	90.3	12.5	107.6
D - Clad	3.3	6.4	0.5	92.5	2.1	104.8
	C	O	Al	Mn	Cu	Total
A - Core	4.8	1.2	94.6	1.7	0.5	102.8
B - Core	4.6	0.7	95.3	1.3	0.5	102.4
C - Core	3.3	2.1	97.6	1.6	0.5	105.1
D - Core	3.9	6.9	98.1	1.3	0.6	110.8

The same decrease that is shown in the clad is not observed in percent carbon on the core region. There seems to be fewer hydrocarbons present on this side of the sheet. One possible suggestion is that it is easier to trap these hydrocarbons under the harder surfaces of surface silicon on the clad side. A slight decrease in manganese levels indicates that some surface intermetallic is being removed from the core side, though much less is at the surface. Copper levels remained roughly constant throughout.

In terms of % oxygen, the clad region saw lower levels of oxide than the core except in the case of the surface prepared (most likely due to preferential attack from HNO_3). The anodized specimen exhibited roughly a six fold increase in % oxygen on both sides compared to as-received, which coincides well with measurements (t_A = 10-20nm, t_D = 65nm). Comparing with other measurements, samples B and C show much less oxygen traces which may be a function of nature/composition of oxide present on the surface. The thermal samples were in a dry oven which may have dehydrated the typically hydrous porous layer. At this point, it is unclear as to why sample B's oxygen composition is so low.

With measurements from FIB-SEM being uncertain due to the level of magnification required, it was decided that any further observation of the surface oxides would be done using TEM.

4.4.3 Oxide Disruption Methodology

From the literature and the current anodization experiments, it was observed that the clad layer and the chemical treatment could create a range of alternate surfaces for the nickel layer to interact with. Therefore, it was of interest to see not only the treatment effects but the effects of these with an increased surface oxide. To limit the extent of this experimental design, anodization was limited to create surface layers of the barrier type only.

Three surface conditions were proposed to be coated later with nickel. The first was the as-received condition with the native oxide on the surface. Surface images from anodization work by Fratila-Apachitei et. al indicated that surface silicon distorts the natural aluminum oxide over the surface [62]. The next was a light surface treatment consisting of a sodium

hydroxide and nitric acid treatment. This would create a surface where the silicon was oxidized and the aluminum oxide layer would be thicker. Finally a heavy surface treatment, similar to what had been done during anodization experimentation, was chosen to remove the surface silicon. These conditions are summarized in Figure 4.14.

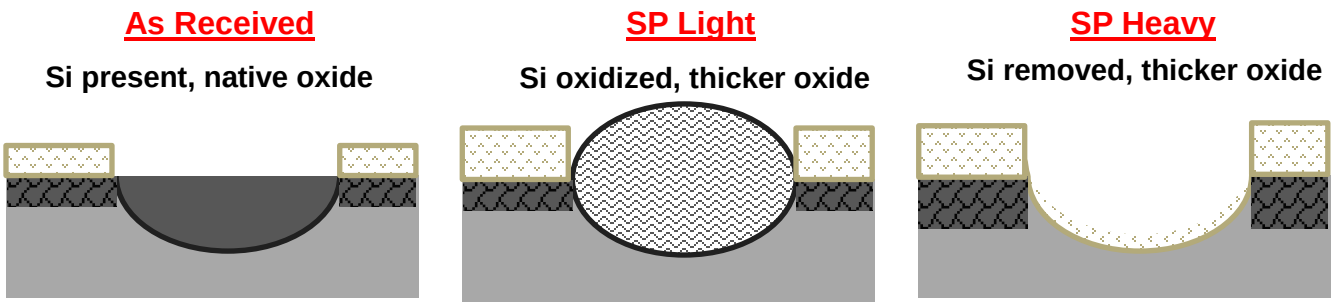

Figure 4-14 - Different Methods of Surface Treatment (White and Black Layers indicate Growth Inwards and Outwards)

As received sheet samples would remain without any surface treatment and be coated with nickel. Both light and heavy surface preparations were then synthesized under three different conditions; one sample anodized in boric acid using 10V, one using boric acid under 40V, and one made only through initial chemical treatment. Light surface preparation refers to a 30s treatment of Sodium Hydroxide, and a 30s treatment of 68% Nitric Acid. The small amount of time was to minimize the growth of oxide from the acid while still prepping the sample for anodization. Heavy surface treatment refers to 30s treatment of NaOH, and two minutes of Nitric and Hydroflouric acid. The longer duration of acid treatment was the length of time it took to visually remove all surface silicon under optical microscopy. All samples anodized were done for a duration of five minutes. This left seven different surface conditions to be coated with nickel. Samples were labeled E-K as follows:

- E – As Received
- F – Light Surface Preparation
- G – Light Surface Preparation, Barrier Type 10V
- H – Heavy Surface Preparation
- I – Heavy Surface Preparation, Barrier Type 10V
- J – Light Surface Preparation, Barrier Type 40V
- K – Heavy Surface Preparation, Barrier Type 40V

A method of coating the surface with nickel was narrowed down to either Chemical Vapor Deposition (CVD), or sputtering. Sputtering offered better surface adhesion given the difficulty in coating the surface oxide with nickel. Sputtered nickel ions would imbed into the oxide and grow epitaxially. The thicknesses chosen for oxide disruption experiments were 0.1, 0.25, and 0.5μm.

4.4.4 Sputtering Equipment

Oxide disruption samples grown in the lab were coated by an ATC ORION series AJA sputtering tool with multi-target capabilities available at the G2N facilities at the University of Waterloo. This machine offered both DC-magnetron and RF sputtering argon plasma onto metals, semiconductors and dielectrics. The machine was capable of heating samples to 1000˚C and main chamber pressures of $5x10^{-7}$ Torr using a diffusion pump. Work done previously by a researcher at G2N provided the initial working parameters for using a nickel target.

Nickel, being a ferromagnetic material at room temperature, possesses a natural magnetic field surrounding itself. This created a problem in that it weakened the ablation effect of being struck by the argon plasma. As a result, higher wattages were necessary to decrease deposition times and improve the sputtering stream. The nickel target was coupled with a DC magnetron which uses high-energy magnetic fields to contain the generated plasma around the target and allow predictable paths towards the desired substrate. The parameters chosen for the sputtering trials were 180W and 5mT in the main chamber at room temperature.

Samples were placed on a sample loading tray and held down with arms fastened to the sample tray with screws. This tray was loaded into the sputterer loading chamber on a holder upside down. The loading chamber was pumped down, and a gate valve was opened allowing the holder to slide into the main chamber. The sample tray was attached to a rotator in the main chamber and then the gate valve was closed. A two minute ramp up was initiated to allow the plasma to strike the target and clean the surface from any previous

work. After the two minute ramp up, the target hatch would open and the sputtered nickel would coat the rotating sample substrate.

Several tests were conducted to determine the optimal deposition times for achieving coating thicknesses of 0.1, 0.25, and 0.5 μm. As received 0.008" braze sheet, from Dana Canada, was used to discern the necessary deposition times. Samples were sectioned into 4 x 4 cm squares and loaded for testing one at a time. These squares were cleaned in acetone prior to loading for cleanliness of the sample and to maintain the uncontaminated environment of the sputtering main chamber.

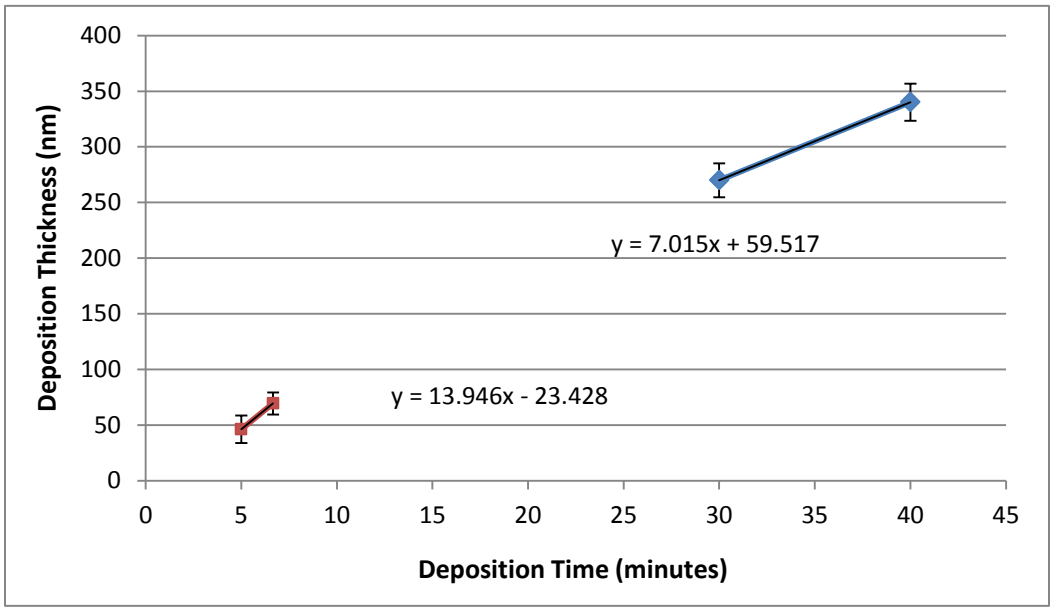

Figure 4-15 - Profilometer Measurements of Sputtered Nickel Coatings on Aluminum Alloy Substrate

Previous work from an operator at G2N had shown that for a 40 minute sputtering time, a coating thickness of 228nm layer would deposit. Trials began using this 40 minute deposition time as well as a 30 minute time. The deposition rates were initially assumed to be linear and were measured using a Dektak 8 stylus profilometer, available at G2N. A glass slide was taped onto the surface of the sample entering the sputterer. The glass slide, and tape, became coated with the same thickness as the sample. The tape was then removed from the glass slide creating a step size measurable in the profilometer. The measurements, including samples coated for 300 and 400 seconds, are shown in Figure 4.15. Twelve independent measurements were taken along the created step in the coating.

It became clear from the profilometer measurements that a linear relationship across all deposition times was not a valid assumption. Measured steps were taken across a length of 500μm and measured heights were taken from a similar length into the coating for comparative purposes. However, during measurements it became clear that the coating was still increasing in size the further one measured into the coating. Measurements lengths increased to 700-800μm were beginning to push the limits of the machine and not coming any closer to a leveling of the coating. This most likely was due to the coating near the step being delaminated and stressed when the tape was ripped before measurement.

From here, all samples were measured under SEM. Samples were deposited for 400s, 30 minutes, and 60 minutes before being sectioned and mounted in stacks of three samples per deposition time. Figure 4.16 shows a sample coated for 30 minutes mounted in conductive epoxy. Higher magnifications on the order of 20,000X were used along with image analysis software to determine the exact thicknesses of the nickel layer. Twelve measurements were taken across three different samples of each deposition type. The results of the measurements are outlined in Appendix F.

The SEM measurements were in good statistical agreement and were the final investigation

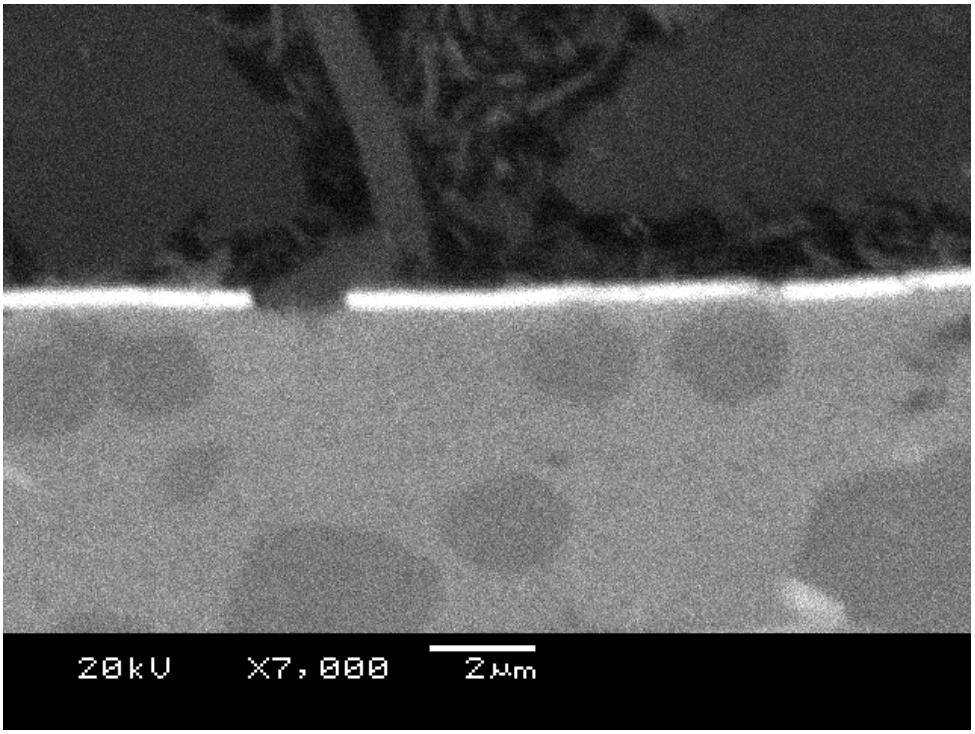

Figure 4-16 - SEM Image of 30 Minute Sputtered Nickel Coating on Clad Layer

taken into discerning deposition times. The final deposition times chosen were 6, 30, and 60 minutes to achieve thicknesses of 0.1, 0.25, and 0.5μm on the substrate surface. Oxide disruption samples were loaded into the sputterer two at a time for each deposition time. For instance, samples G and H would be loaded into the same sample holder for a 6 minute coating. Optical microscopy of the surface was done prior to sputtering so that the clad layer was the coated layer on the single side braze sheet. Samples were transported to and from the sputterer within individual plastic bags to protect them from any contamination.

4.4.5 XPS Equipment

The X-ray Photoelectron Spectroscopy (XPS) equipment available at WatLab in the University of Waterloo was used for investigation of post DSC samples of interest. All depth profiles were conducted with a monochromated Al-Ka (1486.6 eV) 150 W X-ray source. The average sample current applied was 2μA and the takeoff angle at 0°. Vacuum pressure levels in the analysis chamber were set to 2.5×10^{-8} mbar. The defined sputter area for depth profiles was 1x1 mm^2.

5.0 Experimental Results and Discussions

5.1 Characterization of Ni-Plating Process Variation Samples

The composition and structure of Dana's nickel modified braze sheets, and also its behavior thermally, was the first area of interest in this project. Therefore the effect of plating process variations, across the multiple braze sheets that were supplied, was to be investigated. All plated sheets were of the same base braze sheet which was a 0.2 mm (0.008"), single side clad layer, containing 10% silicon.

5.1.1 Initial Braze Sheet Measurements

Initial characterization was done using optical microscopy and SEM of the as-received braze sheet. Samples received are discussed in section 4.1 and its cross section is shown in Figure 5.1. The figure shows a single sided, 9% clad, braze sheet. Spheroidized silicon can be seen on the upper 9% of the sheet (clad layer). Iron and manganese precipitates are distributed throughout the remaining core layer.

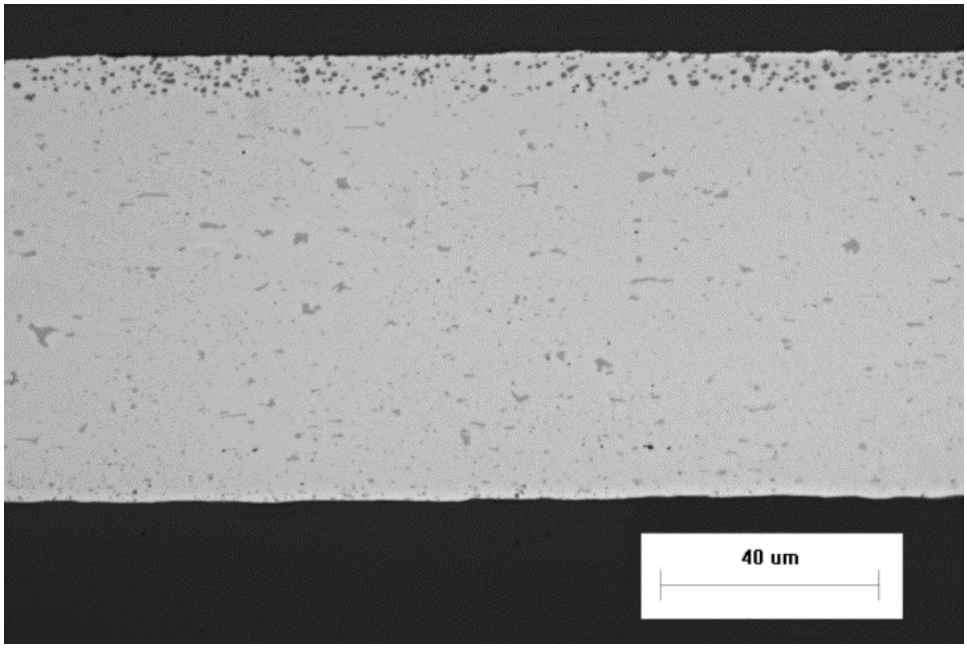

Figure 5-1 - Cross Sectional Imaging (200x) of (a) Single Sided 3003/4045, 0.02cm Braze Sheet

A method for measuring the fraction coverage and mean height of the sample plating deposits is shown in Figure 5.2. The image shows a schematic of a typical screen shot of the clad layer as viewed under optical or SEM. The total length, L_t, of the sample on the screen was taken and then the length and height of each deposit was measured. From these measurements, the following equations were used.

$$\textbf{Fraction Coverage, } f = \frac{\sum_1^n L_n}{L_t} \qquad \textbf{Mean Height, } \bar{H} = \frac{\sum_1^n h_n}{n}$$

Ten images were taken across the cross section for uniform measurement of the sectioned sheet. The deposit heights, and their standard deviations, have been normalized using the highest measured value. SEM measurements of sections from the centre of the sheet were mounted and measured using the above methodology (see Figure 5.3).

From the measurements it became clear that there was no discernible difference in deposit height between samples A, B, and C. There was a slight increase in deposit height from A to C and all samples were normalized to the tallest sample, C. It was also clear from the data that there was a lot of scatter in deposit height. Optical measurements were observed to be 30% larger than SEM measurements.

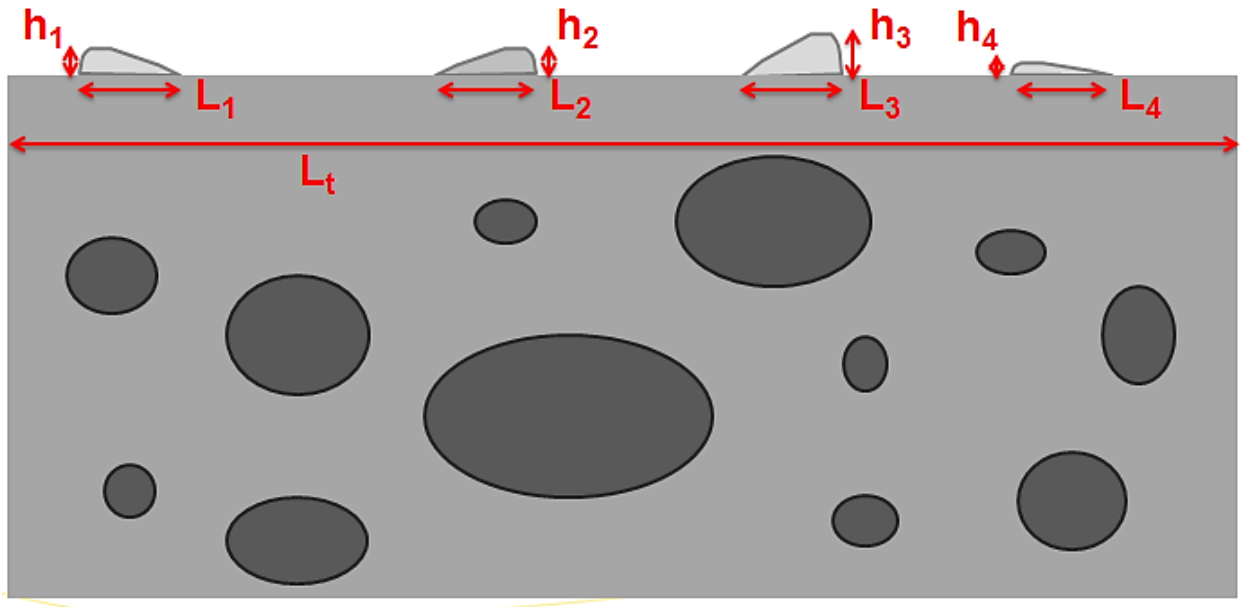

Figure 5-2 - Method of Characterizing Nickel Deposits on Clad Surface

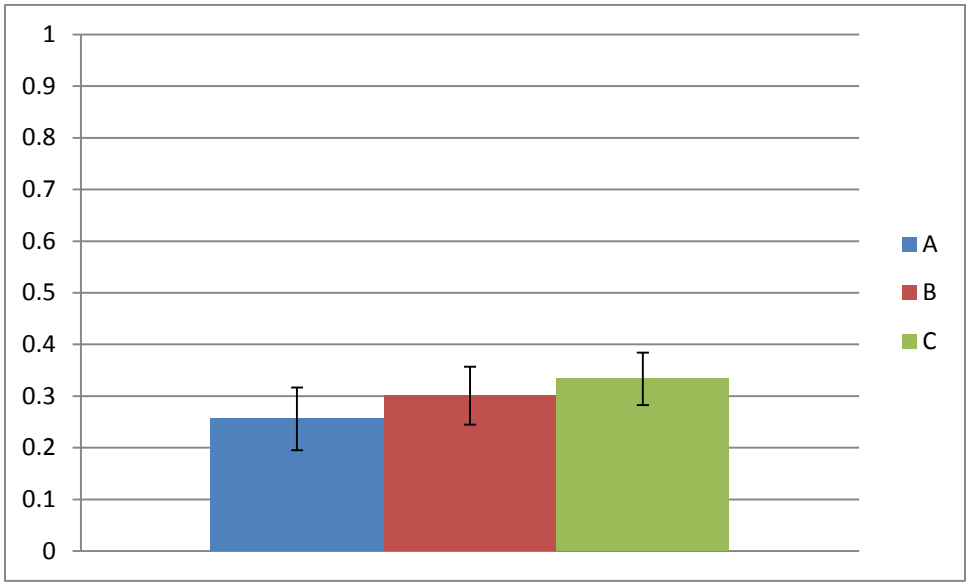

Figure 5-3 - Normalized Measured Thickness of Nickel Deposits on Samples A, B and C measured under Scanning Electron Microscopy

Following these measurements, specimens were loaded into the SEM oriented flat such that an overview of the surface was observed. These images provided insight not only into the plating nature of the nickel deposits, but also fraction coverage could be measured. Images were taken under SEM at 700X magnification. For each plated sheet, sixteen images were taken and stitched together using photo editing software. They were then exported into Image Pro software where contrast was used to resolve the area fraction, see Figure 5.4. This figure shows the segmentation function used on a photo of an unrelated solutionized Al-Cu-Mg-Si sample examined under SEM. The differentiation of contrast was used to calculate the percentage of nickel deposit coverage on the aluminum surface.

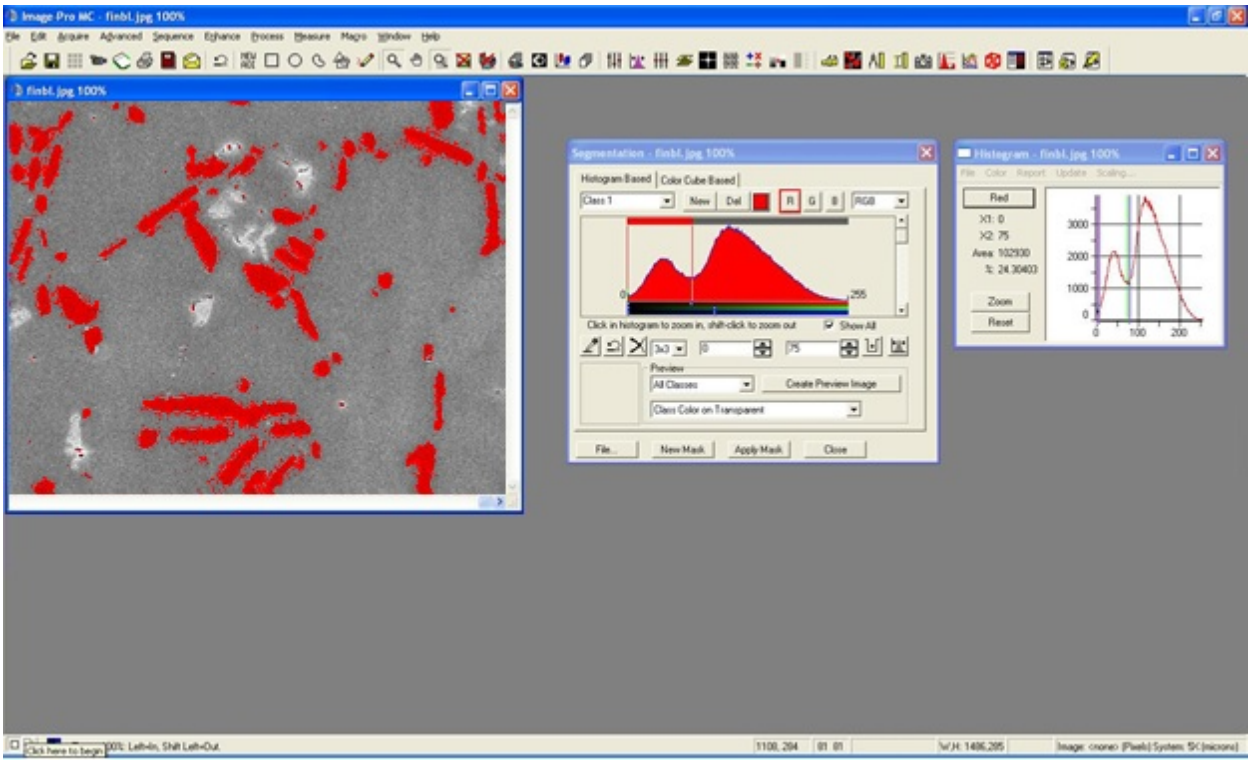

Figure 5-4 - Example of Area Coverage Calculation on SEM Image using ImagePro

The effect of punching samples for DSC was also considered. Two additional stitched images from SEM were created using DSC samples punched from the plated and unplated side located at the centre of each sheet. It was believed that the impact from the punch into the sample may have either pushed the nickel layer into the sample, or caused it to flake off depending on the side of impact. The results of these calculated areas are shown in Figure 5.5. It became apparent from the resultant areas that the orientation of punching had little or no effect.

The method of area calculation by SEM proved to be far more effective at determining the area fractions of the nickel braze promoter layer. The stitched images covered a much larger surface area and allowed for a much more global array of measurements than optical methods. A notable difference was observed during the SEM calculations. Sample A exhibited a 7-10% increase in plating coverage which was considered as a factor later during thermal analysis.

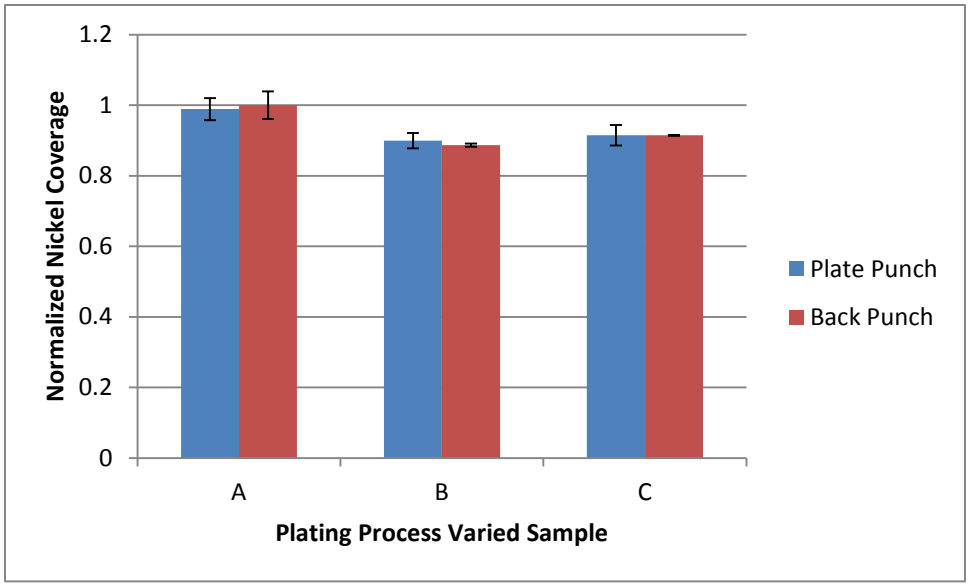

Figure 5-5 -Fraction Area Coverage Calculated Using SEM with Punch Direction Considered

All samples for DSC were punched from the centre of the braze sheets to minimize any variability.

5.1.2 Observation and Measurement of the Nickel Reaction

Thermal analysis of Process Plating Variations (PPV) began with examination of unplated braze sheet behavior. Initial testing was a simple heating to 590°C and then cooling at 10K/min, an example is shown in Figure 5.6. The data from the heating of the sample is shown in red, and cooling in blue. Two distinct curves are observable; one for the melting of the clad layer on the braze sheet and one for the resolidification. The melting endotherm was measured to be 18.84J/g with a peak value of 577.7°C in line with the Al-Si eutectic, see Appendix A. Upon freezing, a reduced enthalpy of -12.62J/g was recorded with a peak value of 568.7°C. The reduced enthalpy and peak value during resolidification are due to the diffusion of silicon into the core as discussed in section 2.2.4. Three tests in the DSC were run for the as-received brazing sheet sample. The averaged results of these tests are shown in Table 5.1.

Table 5-1 - Averaged DSC Results of Different Unplated Brazing Sheets

Gauge Thickness	Nominal Clad	Melt Onset (°C)	Endotherm (J/g)	Melt Peak (°C)	Exotherm (J/g)	Weight (mg)
0.008"	9%	574.7	19.36	577.7	-16.35	10 ± 0.1

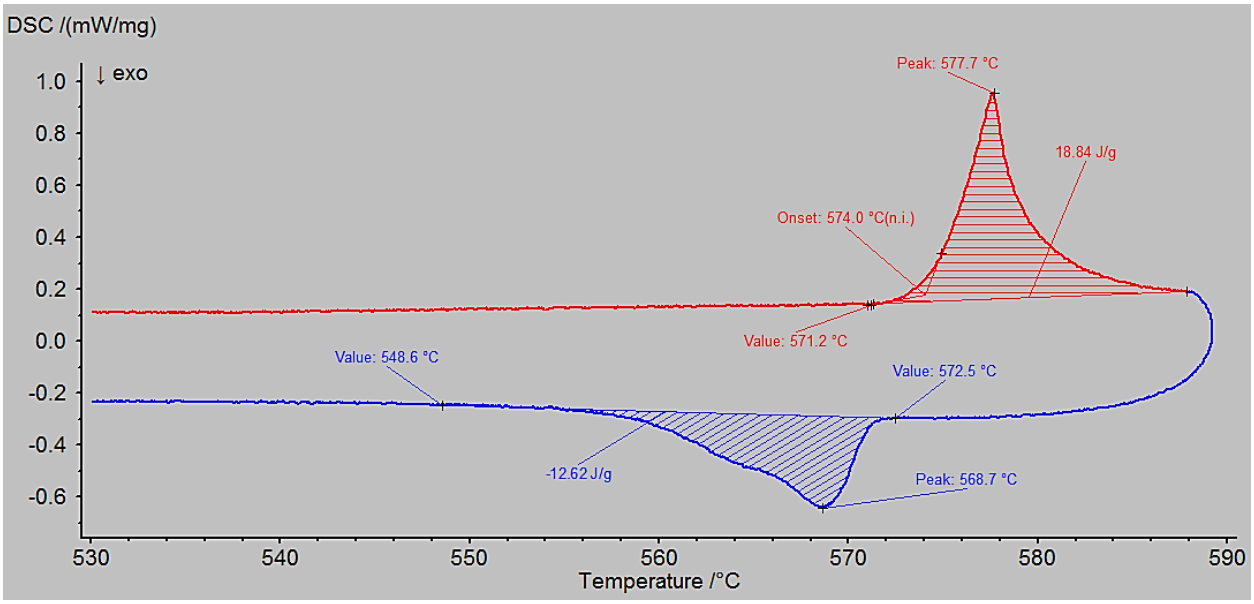

Figure 5-6 - DSC Trace of Unplated, 3003/4045, H24, 0.008" Braze Sheet

To obtain an understanding of as-received sheet behavior and plating behavior, plated samples were tested under the same DSC temperature ramp up to 590°C. Corbin et al. had previously noted a sizable exotherm prior to any melting endotherm [30][67]. This value would typically peak at 565°C which coincided with the Al-Ni-Si ternary eutectic point as well as the formation of Al_3Ni. Recall that the ternary eutectic is denoted as L = (Al) + (Si) + (Al_3Ni). The same results were observed in samples A, B, and C when testing for plating process variation, see Figure 5.7a-c.

The exotherm from intermetallic formation proved to be quite variable with values ranging from -0.5 to -8.0 J/g across samples A, B, and C. These values did not show any notable trend across the different samples and could sometimes register no exotherm at all. The results of the above tests (averaged over 3 sample runs) in Figures 5.8a-c are outlined in Table 5.2. Variance in temperature onsets and peaks were within the stated measurement reproducibility for temperatures (±0.3°C). There was a slight decline in peak, onset, and end values of the peaks trending from sample A to C. The difference in melting endotherms was another large difference between plated and unplated samples which will be discussed later in this section.

Table 5-2 - DSC Results of Heat Up to 590°C and Cool Down for Samples A, B, C, and Unplated Braze Sheet

Heating Exotherm	No Plating	A	B	C
Initiates (˚C)	-	564.8	563.2	563.1
Onset (˚C)	-	565.2	563.9	565.3
Area (J/g)	-	-2.86 ± 1.55	-2.23 ± 0.58	-2.55 ± 0.44
Peak (˚C)	-	566	564.9	564
Ends (˚C)	-	566.8	566	564.5
Heating Endotherm				
Peak (˚C)	577.7	567.6	567.2	565.2
Area (J/g)	18.84	8.67 ± 1.66	8.32 ± 0.11	7.02 ± 3.16
Ends (˚C)	587.9	580.5	577	571.3
Cooling Exotherm				
Initiates (˚C)	572.5	562.5	560.1	560.1
Peak (˚C)	568.7	555.9	555.8	555.6
Area (J/g)	-12.62	-12.34 ± 0.34	-13.85 ± 0.62	-13.58 ± 0.72
Ends (˚C)	548.6	539.6	544.3	544.2

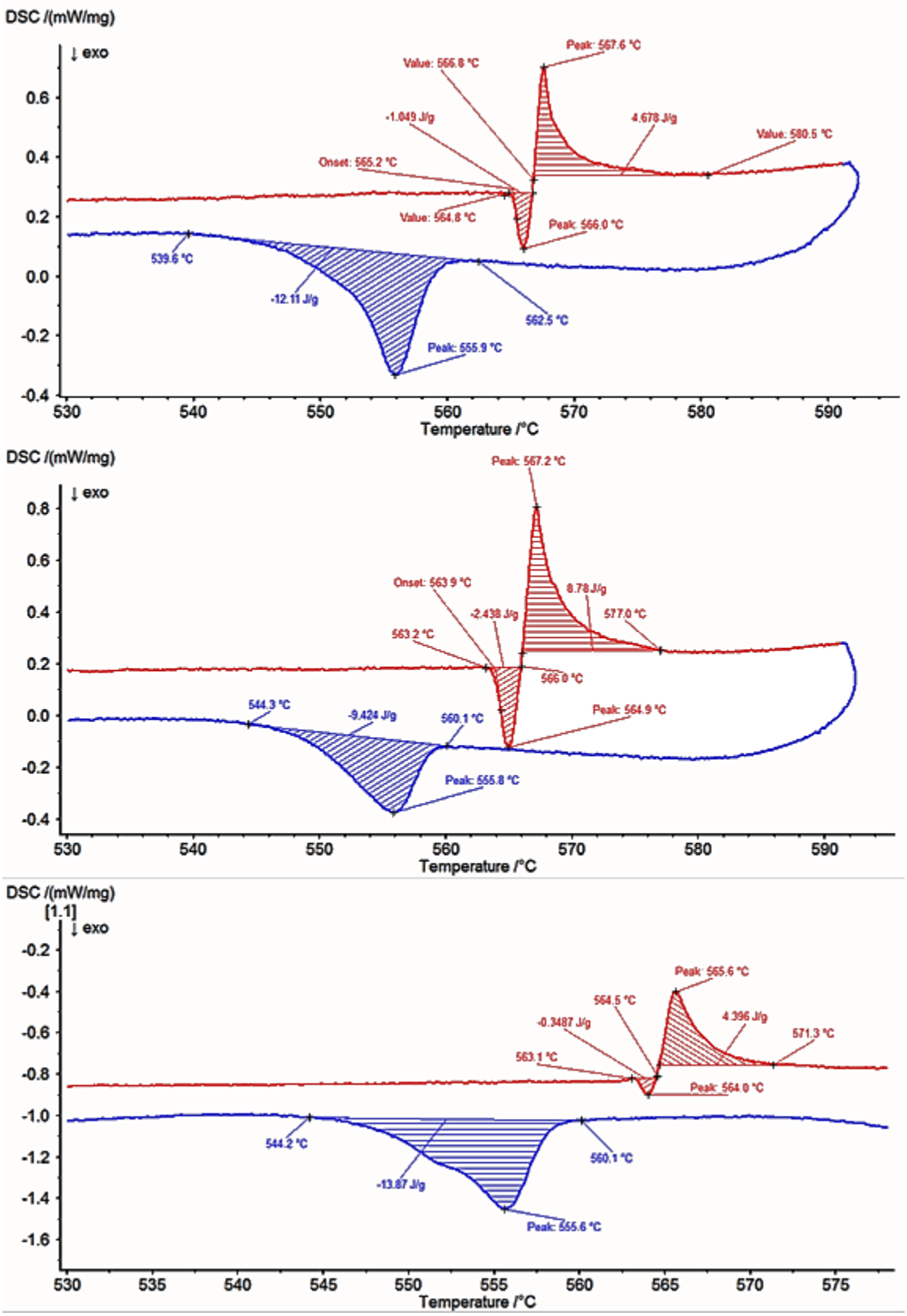

Figure 5-7 - Heat Up (Red) and Cool Down (Blue) of Samples A, B, and C, Respectively, Demonstrating Nickel Exotherm on Heat Up

The DSC reacted coupons were mounted and examined under optical microscopy and SEM. Images of the reacted nickel layer were examined at 100X under optical, see Figure 5.8a-c. The surface of the clad layer was heavily roughened with nickel/silicon-rich phases present. The formed Al_3Ni was visible as a light grey phase in large clusters embedding into the aluminum matrix. This is due to large amount of aluminum needed to be consumed to form the intermetallic as well as the large volume fraction increase observed in Al_3Ni crystal structure, see section 2.3. The formation of silicon as a component of the ternary was observable as a dark grey phase representing Al-Si eutectic.

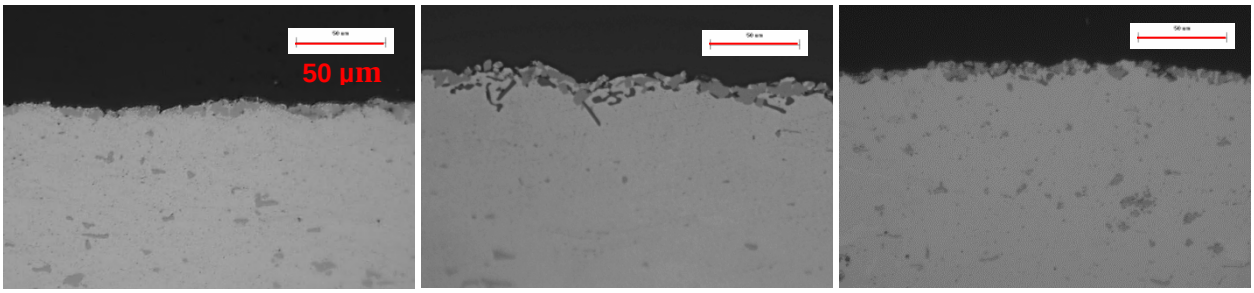

Figure 5-8 - Samples A (left) to C (right) Fully Reacted after Ramp Up to Braze Temperature 590°C

An interest in viewing the reacted surface prior to melting led to the SEM imaging of a

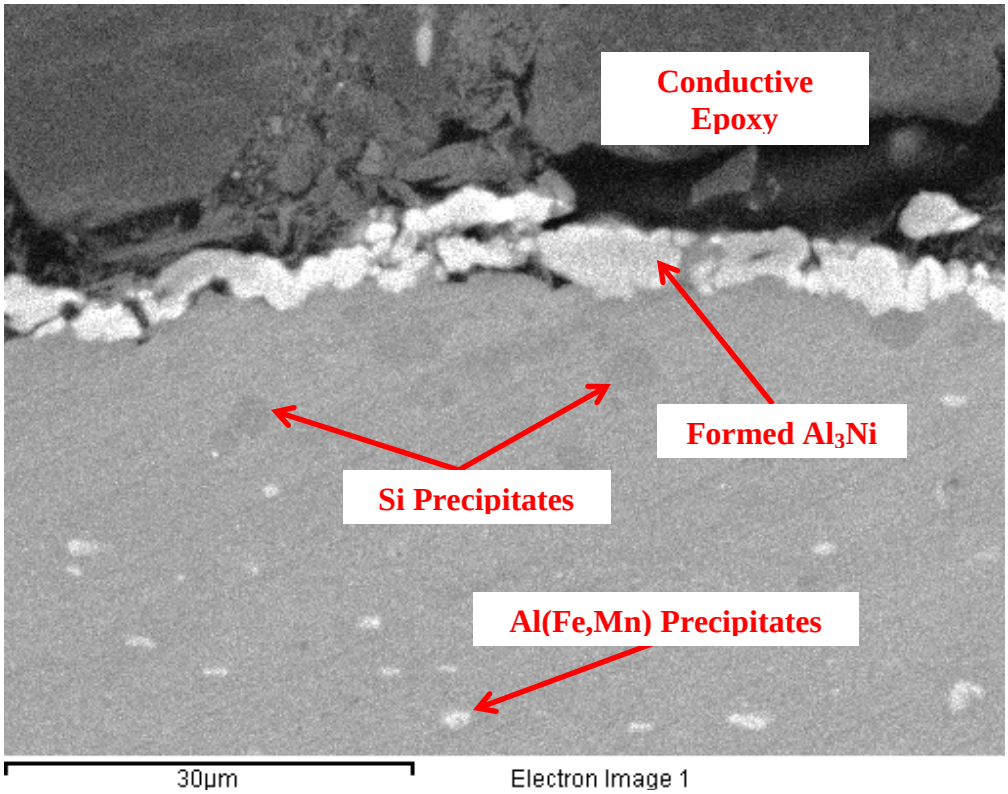

Figure 5-9 - SEM image of Sample A brought to 563°C and subsequently cooled

sample ramped up only to 563°C. The reacted nickel surface tended to occupy a continuous strip of the overall clad layer. Figure 5.9 shows the presence of the NiAl3 intermetallics, Fe-rich phases and Si eutectics etc. Other precipitates relating to braze sheet microstructure (outlined in sections 2.2 and 2.2.5) are visible as well.

5.1.3 Behavior of Liquid Clad Layer Melt

The length of liquid duration in each sample was initially tested using an isothermal hold outlined in section 4.2.3, Figure 4.4b. The testing was done using separate samples which sometimes yielded variations in the liquid duration trends, see Figure 5.10. These differences were believed to be caused by variance in the amount of nickel respective to the PPV method and/or local coverage of each sample. Isothermal hold times varied from 2-30 minutes depending on whether the sheet was plated or unplated. Figure 5.11 outlines the reduction of freezing exotherms (Si diffusion) upon solidification of each sample, in this case for unplated sheet. Exotherm values for the initial irreversible exotherm of intermetallic formation varied greatly. Aside from sample C, all samples trended linearly towards a liquid duration of 18-20 minutes. Thus, though the nickel layer did tend to lower liquid duration slightly, liquid duration of all sheets was fairly consistent and lost Si content to the core at a constant rate.

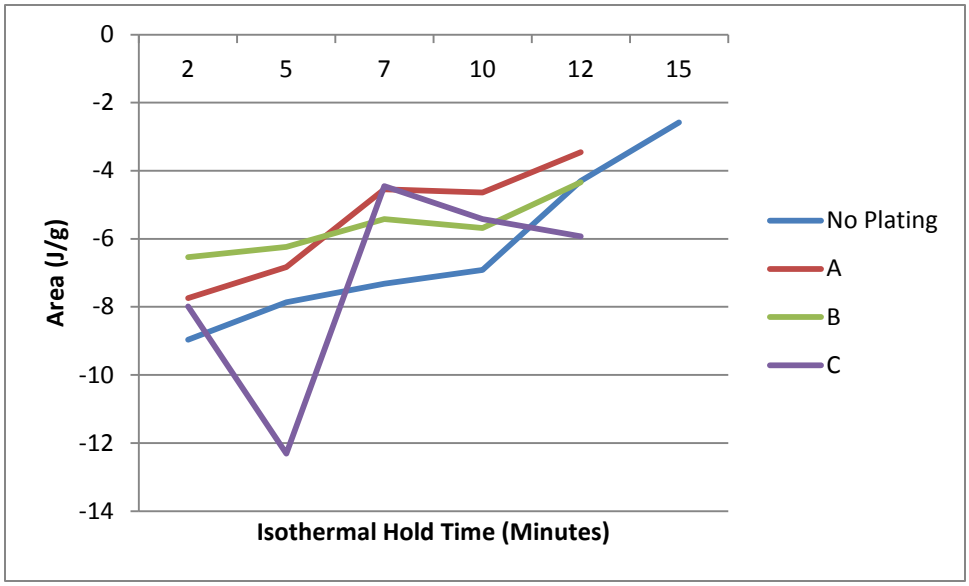

Figure 5-10 - Isothermal Hold Testing of Samples A, B, C, and Unplated showing Trend in Cooling Exotherms

These isothermal tests were done prior to any knowledge of cyclic testing results achieved by Corbin et. al. In terms of kinetics, these tests provided very little data other than a rough estimate of total liquid duration. Following this batch of tests, all further liquid testing was done using cyclic testing discussed later in this section.

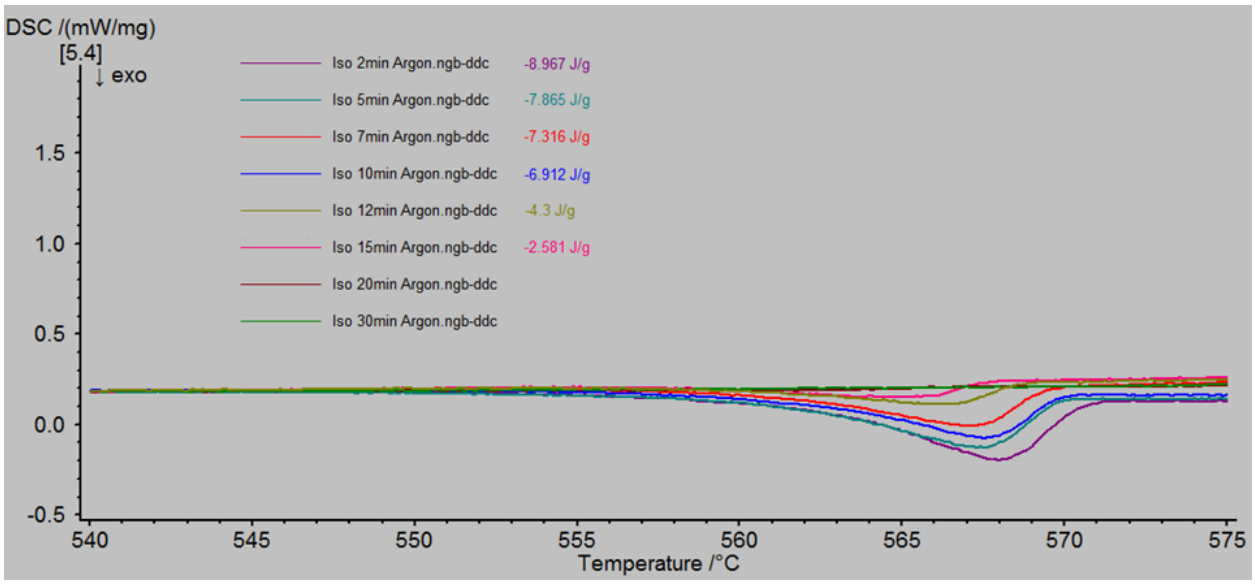

Figure 5-11 - Isothermal Holds of 0.08" H24 Unplated Braze Sheet Held at 590°C for 2-30 Minutes for Each Test

The suppression of the melting endotherm due to initial intermetallic formation created issues in calculating the first enthalpy of melting. Figure 5.12 illustrates this difficulty between the two opposing enthalpies. The red dashed line shows the DSC signal as it is

received in a typical ramp up of nickel coated braze sheet. The black line depicts the true heights and widths of each individual enthalpy and their calculated areas.

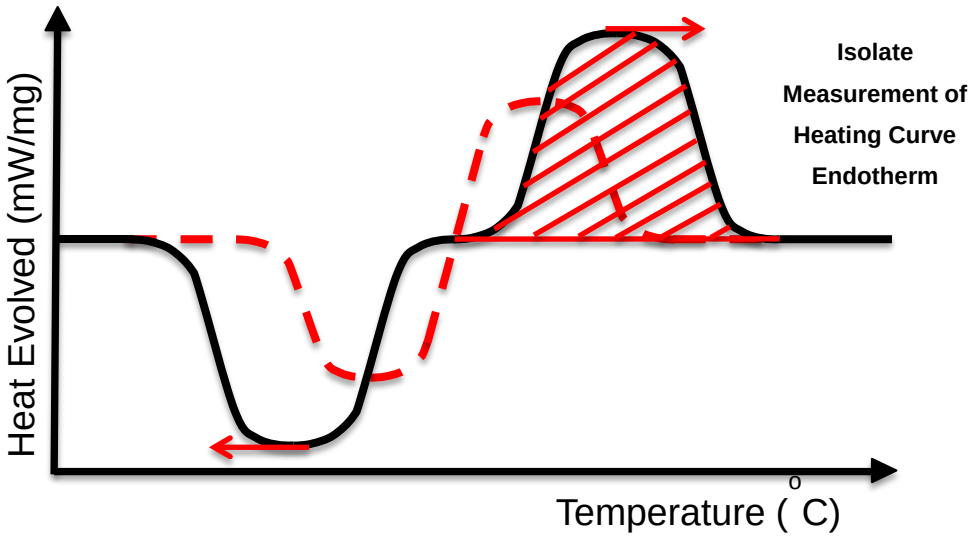

Figure 5-12 - Illustration of Heating Curve Convolution of Exotherm and Endotherm (Red Dashed Line) and Desired Method of Separation (Black Line)

It was found in previous SEM work that the nickel reaction was indeed a one-time reaction and would be absent upon further heat up. This was illustrated in Figure 5.9 where at 563˚C all the surface nickel deposits had become a thick layer of reacted Al_3Ni. This reaction can be observed in the material's microstructure after exposure to elevated temperatures as low as 555˚C in the DSC and can complete as early as 563˚C, see Figure 5.13. Further tests proved that the reaction occurred continuously when held isothermally at 560˚C and that all surface nickel could react prior to the Al-Si-Ni ternary melting point of 565˚C.

A temperature program was devised in an effort to de-convolute the heat of intermetallic

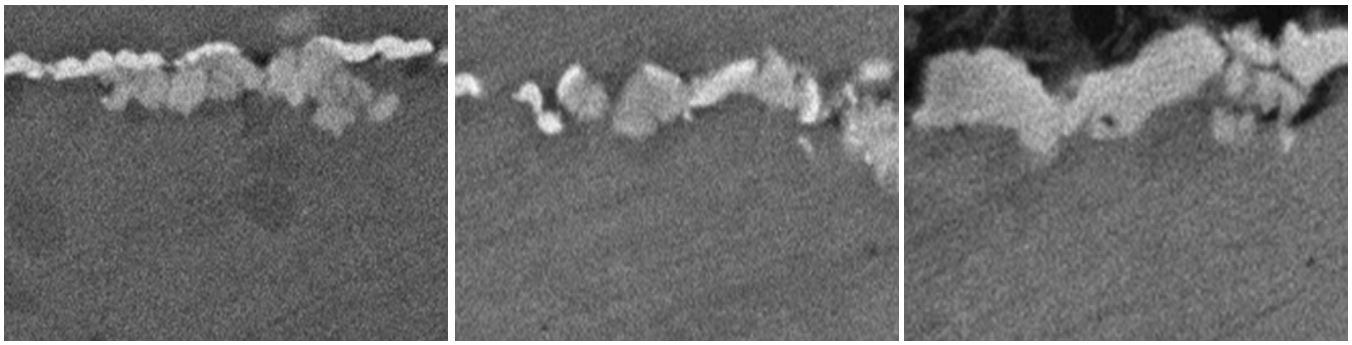

Figure 5-13 - SEM Imaging showing DSC specimens heated to and cooled from (a) 555˚C (b) 560˚C (c) 563˚C

formation from the melting endotherm. This involved a designated hold time at a temperature of 560˚C for 2-10 minutes. This would provide sufficient time for the surface nickel to completely react and form Al_3Ni with the surrounding clad layer. The sample would then be cooled to 500˚C, before a ramp up to 590˚C, and then cooled. The cooling to 500˚C was to allow sufficient ramp up time to achieve a steady baseline and reliable re-heat

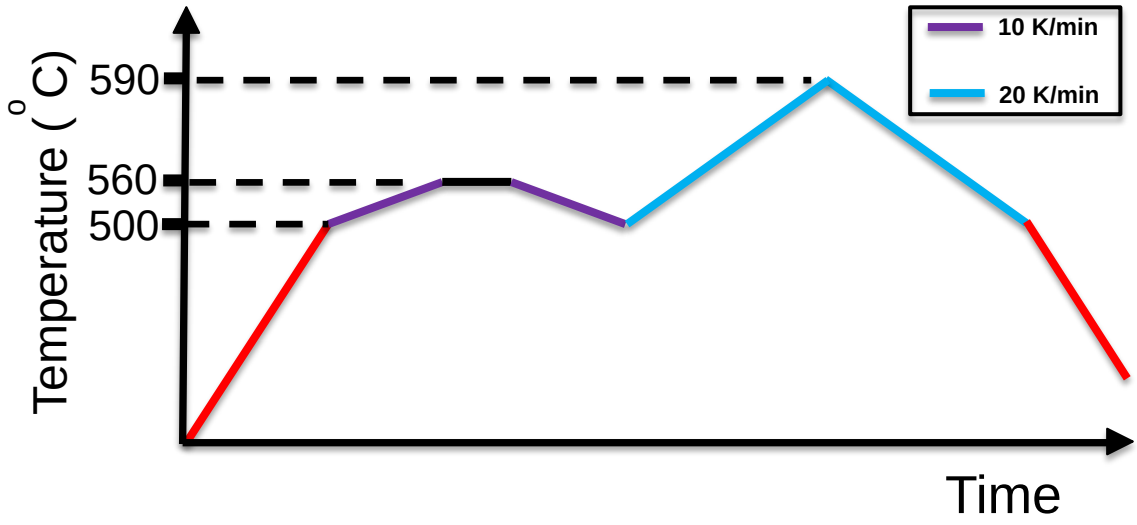

Figure 5-14 - Temperature Program for Exohold DSC Experiment, Black Line indicates Isothermal Hold

endotherm data. The temperature program as run in the DSC is shown in Figure 5.14.

The results of this testing is shown in Figure 5.15 for sample A. Notice that an exotherm on

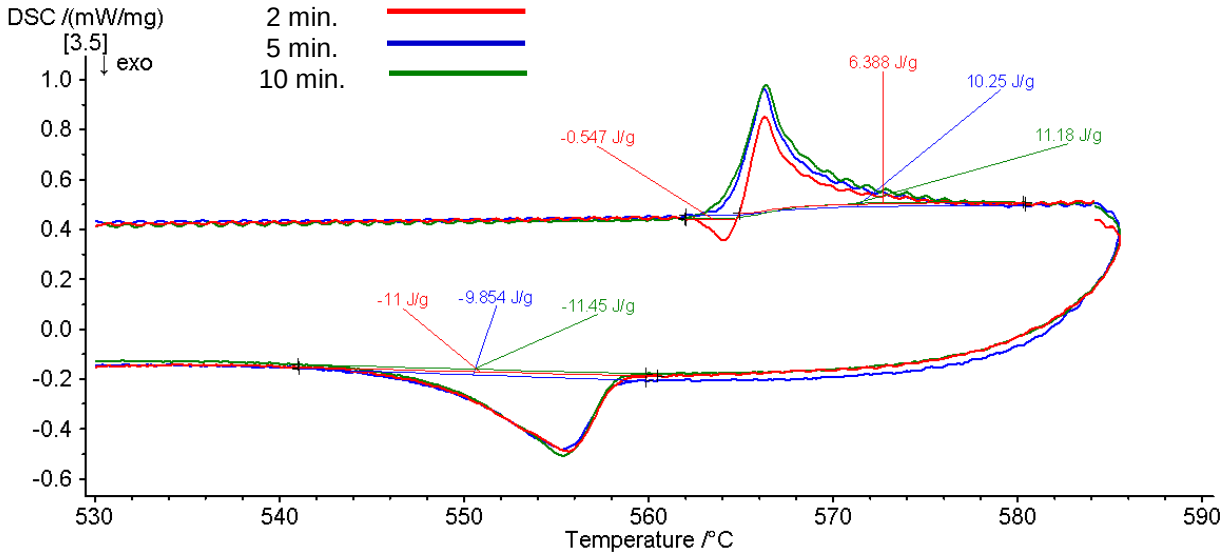

Figure 5-15 - DSC 'Exohold' Testing Showing Heating Endotherms and Cooling Exotherms after Isothermal Holds of 560°C at 2, 5, and 10 Minutes

heating is observed only in the two minute condition. All other tests show no reaction of nickel following a five and ten minute isothermal hold at 560˚C. This would seem to support the argument that the aluminum nickel reaction is a one-time exothermic reaction which is convoluted with the melting endotherm. This is further supported by the fact that the melting endotherm increases as the hold time at 560°C increases, see Figure 5.7.

The resulting enthalpies are listed in Figure 5.16. A drastic improvement in overall heat endotherm energy was observed in comparing initial testing (heating to 590˚C and cooling) of the PPV samples and exohold testing of the same samples A, B, and C. Sample B showed the most persistent exotherms in all cases of the nickel aluminum exothermic reaction. It was not until the specimen was held to 560˚C for ten minutes and then subsequently melted that the exotherm was finally removed and a higher endotherm was observed compared to initial testing. All samples showed no exotherm following a ten minute hold and most only required two minutes (Samples A and C). Holds at 560˚C were expected to include silicon diffusion while the nickel reacted. While improvements are seen in the endotherms from initial testing, these are still lower than the unplated condition.

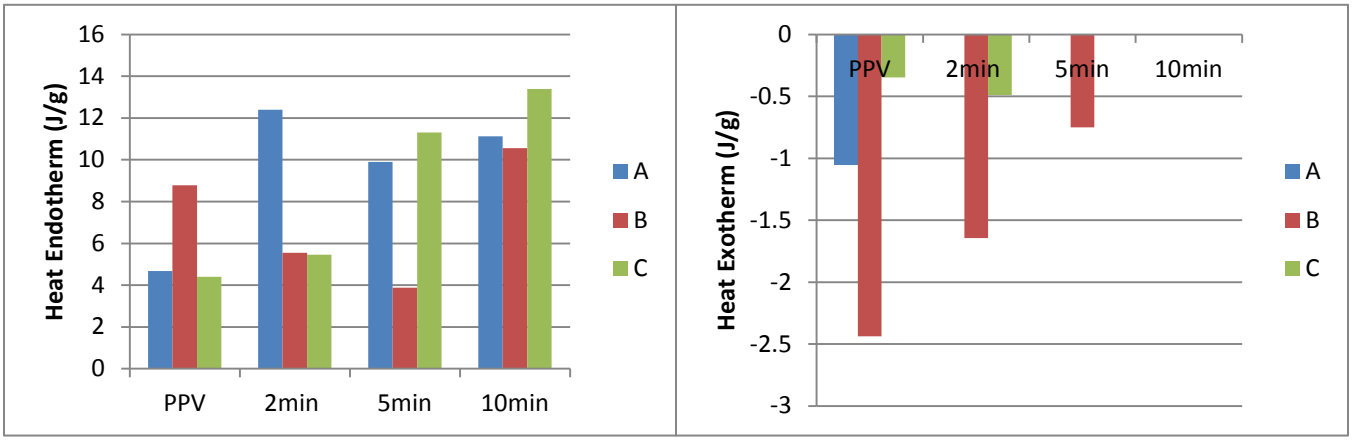

Figure 5-16 - Comparing Exohold Heating Results to Initial DSC Testing of PPV Samples

SEM images of the samples A, B, and C were taken after heating to observe the reacted surface, see Figure 5.17. The same blanketing effect of molten aluminum was observed in samples A, B, and C that had been seen in section 5.1.3. The bumpy surface was attributed to the presence of hard Al_3Ni formations dispersed in the resolidified matrix. These formations were either lying above the matrix or were encased by it during resolidification. The surface of sample B showed a much finer dispersion of these particles compared to

samples A and C. Again surface roughness was prevalent which was consistent with all previous optical and SEM imaging.

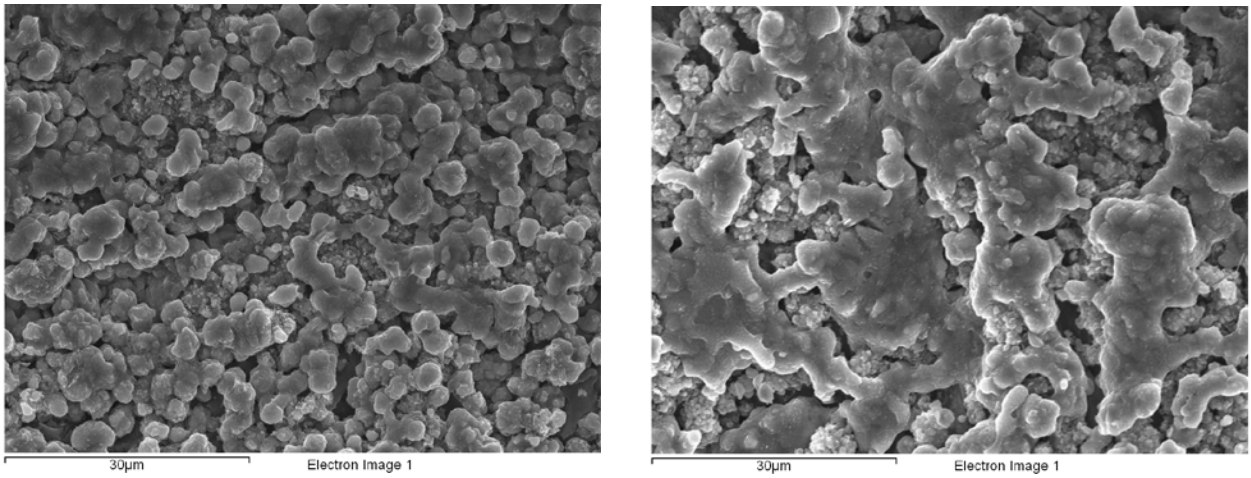

Figure 5-17 - SEM Surface Images of Samples A and C, Respectively, following Nickel Reaction and Melting at 560°C prior to 'Exohold' Testing

For a more definitive description of liquid duration, cyclic testing was done for all plated and unplated samples. The temperature program is illustrated in Figure 5.18. The beginning of the DSC test is similar to a ramp up to 590˚C with a 10Kpm heat to 500˚C and 20Kpm to 590˚C. Samples are then cycled at 10Kpm from 590˚C to 490˚C back and forth. For every 590˚C peak there was an isothermal hold of 1-5 minutes depending on the sheet thickness. The most common test for 0.008" braze sheet had four 1 minute holds and a final 2 minute hold at the end to allow extra time for isothermal solidification.

As discussed in chapter 2.0, silicon will diffuse from the clad layer into the silicon deficient core region. The rate of diffusion is increased when the clad layer is molten and the silicon

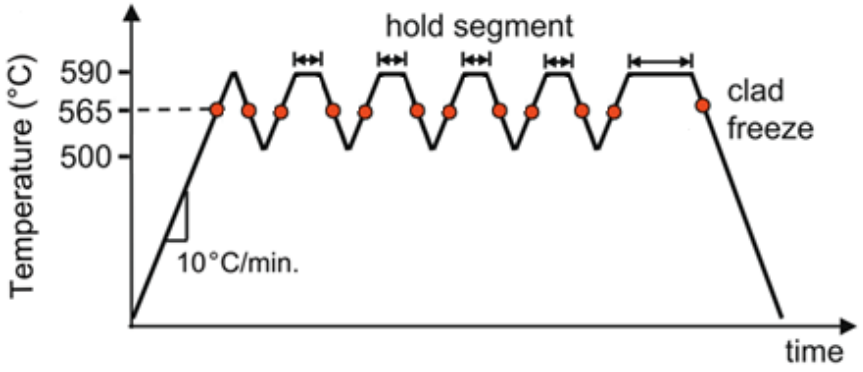

Figure 5-18 - DSC Temperature Program for Cyclical Testing

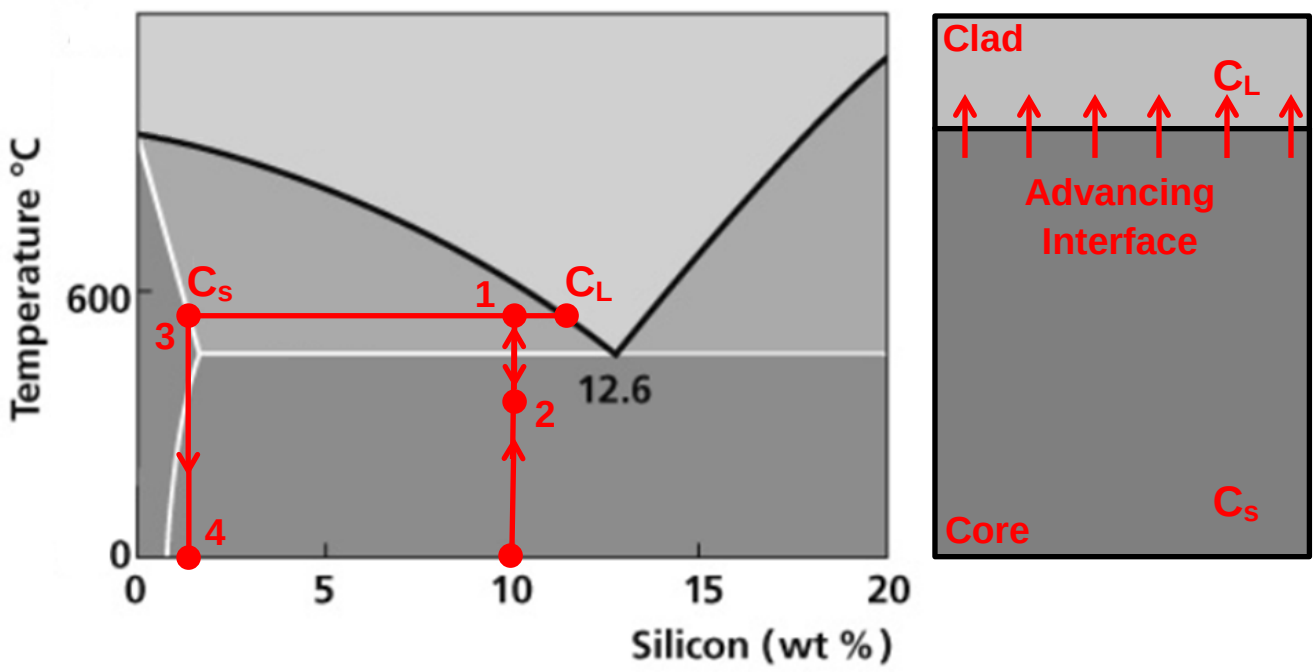

Figure 5-19 - Representation of the Effect of DSC Cyclical Testing on Clad Composition based on the Al-Si Phase Diagram [73]

is near to core region grain boundaries. As a result, the clad layer thickness is reduced with each successive heat up and cool down during the cyclic testing. Figure 5.19 shows the resultant path on an Al-Si phase diagram followed during this cyclic testing on a sample with 10% silicon. Cyclical heating of the braze sheet between 500˚C and 590˚C (Points 1 and 2) leads to silicon diffusion and an advancing interface of composition C_s. Eventually only a composition C_s remains (Point 3). Successive heating and cooling between points 3 and 4 will result in an absence of endothermic and exothermic peaks during DSC testing. Only much higher temperatures will show any trace of melting for this composition. A similar effect would be expected for the Al-Ni-Si system.

The enthalpies of melting of each braze sheet were recorded for every peak, on the temperature program above, until no area could be measured. When these enthalpies go to zero the sample has solidified isothermally by silicon diffusion and no liquid phase remains present for temperatures up to 590˚C. To acquire true liquid duration data, it was imperative to document the times where melting onset and the times where freezing completed. Recall that melting of these braze sheets onsets around 574˚C and completely freezes at roughly 550˚C. The addition of these total liquid durations totaled to roughly a half hour for one DSC test. Values for all data were averaged over three tests.

The same unplated braze sheets tested in section 5.1.1 were first examined using the cyclic method, see Figure 5.20. The liquid duration data for all samples followed a parabolic function typical of isothermal solidification, as noted by Corbin et al. This parabolic relation has been shown to be directly related to the rate of isothermal solidification across a planar solid-liquid interface [67]. The calculated trend line and its R^2 values are included in Table 5.3. The rate of removal of silicon showed a strong linear trend and a value of zero at twelve minutes suggesting liquid duration was much lower than predicted in isothermal tests. This was attributed to the braze sheets being thinner than those studied by Corbin et. al and having less silicon available to maintain the molten clad layer.

Table 5-3 - Linear Extrapolation of Heat Endotherms for Unplated Samples versus Liquid Duration Squared

Gauge	Nominal Clad	Trend Line	R^2	Total Duration (minutes)
0.008"	9%	$\Delta H = -5.576t + 19.743$	0.9996	12.20

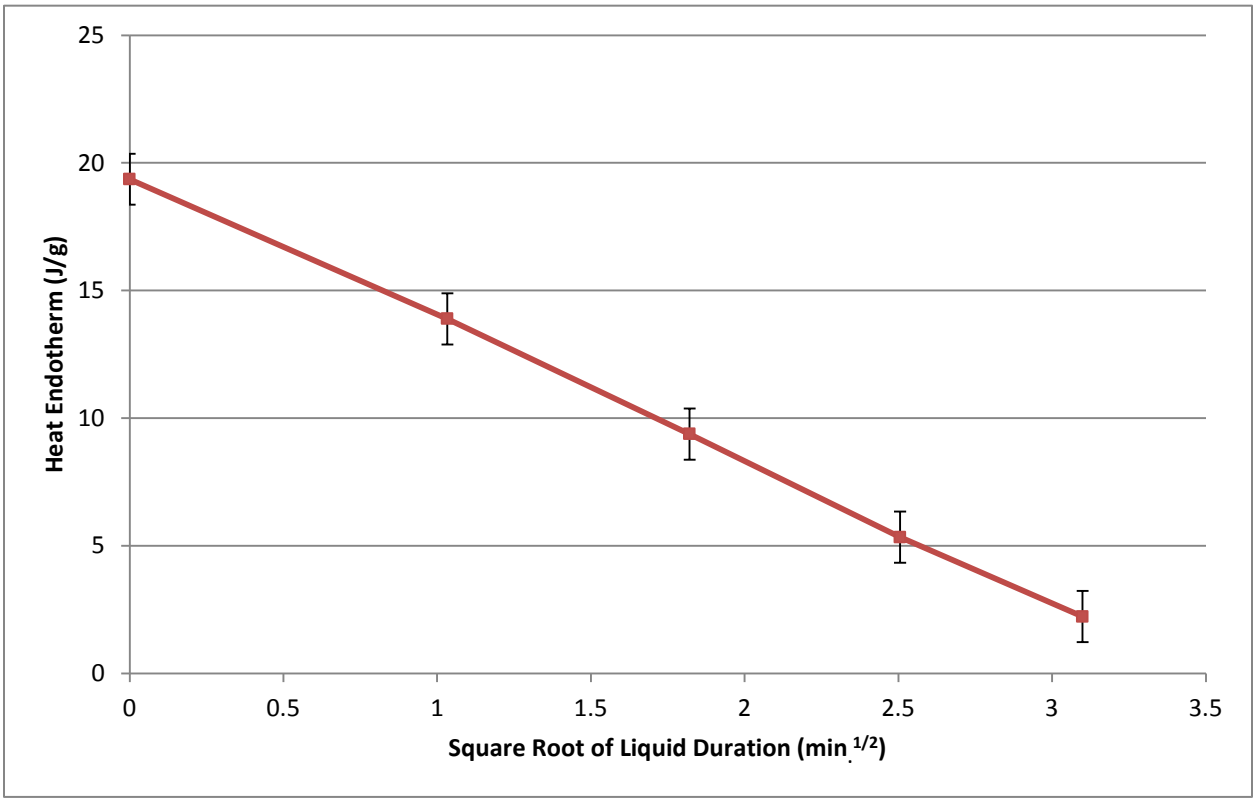

Figure 5-20 - Heat Endotherm Values for Cyclical Testing of 0.008", 9% Clad Braze Sheet

Samples A, B, and C were all plated versions of the 9% SS braze sheet mentioned above. The results of the nine cyclic tests are shown in Figure 5.21. The data has been shifted to the right to show how strong the effect of Al_3Ni is on the first endotherm. Again there is no real trend to the initial values of the exotherms or endotherms across the various platings. While the absolute values of endotherms over braze time were variable, the rate of reduction (i.e. the slopes of the curves) are similar for all materials. Samples from A showed the highest average endothermic values of all the samples and as Figure 5.22 shows, these values were most in line with the unplated braze sheet. Samples B and C showed an inhibited liquid duration over the entire cyclic testing.

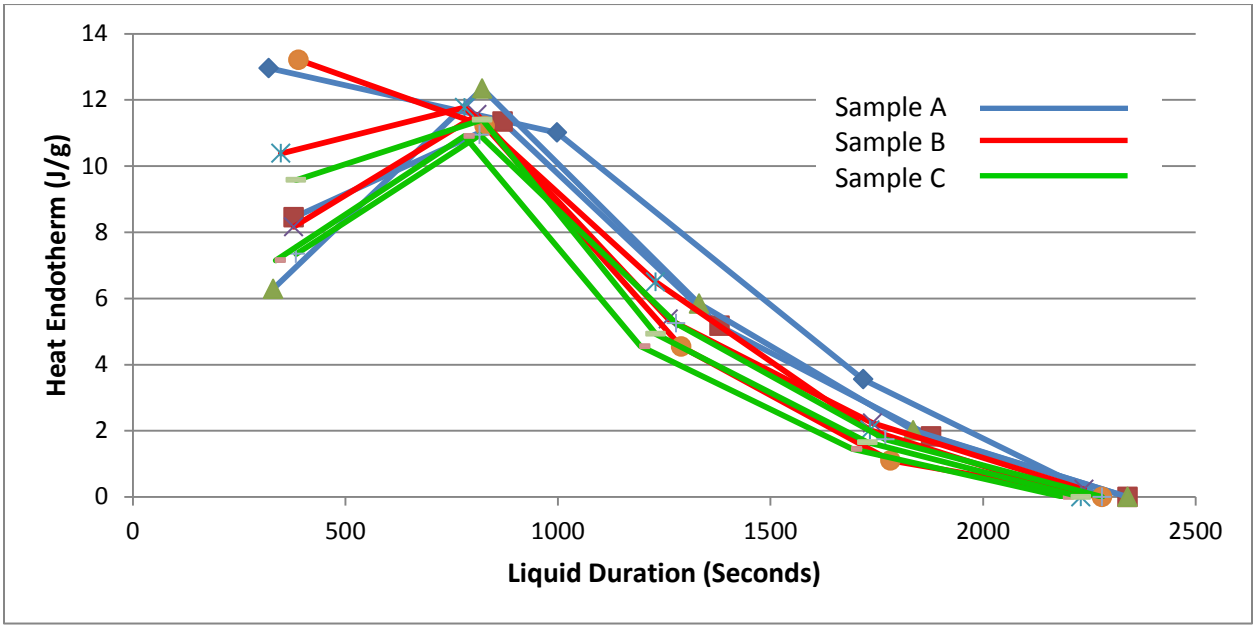

Figure 5-21 - Heat Endotherm Values for Cyclical Testing of Samples A, B, and C

From the calculated trend lines, the initial endothermic values for the plated sheets varied between 15-20 J/g which agrees well with non-plated data. A noted decrease in both B and C samples was consistently observed during all tests. The reason for this difference may be attributed to the slight difference in surface area coverage of nickel. Another possibility is the higher measured values of nickel found in B and C, though this was only marginally higher. This increased amount was noted during SEM and optical testing which showed B and C had thicker deposits by 10-20%.

The data was then averaged and graphed over liquid squared duration, as shown in Figure 5.22. From this initial endotherm values could be extracted. From these results it appeared

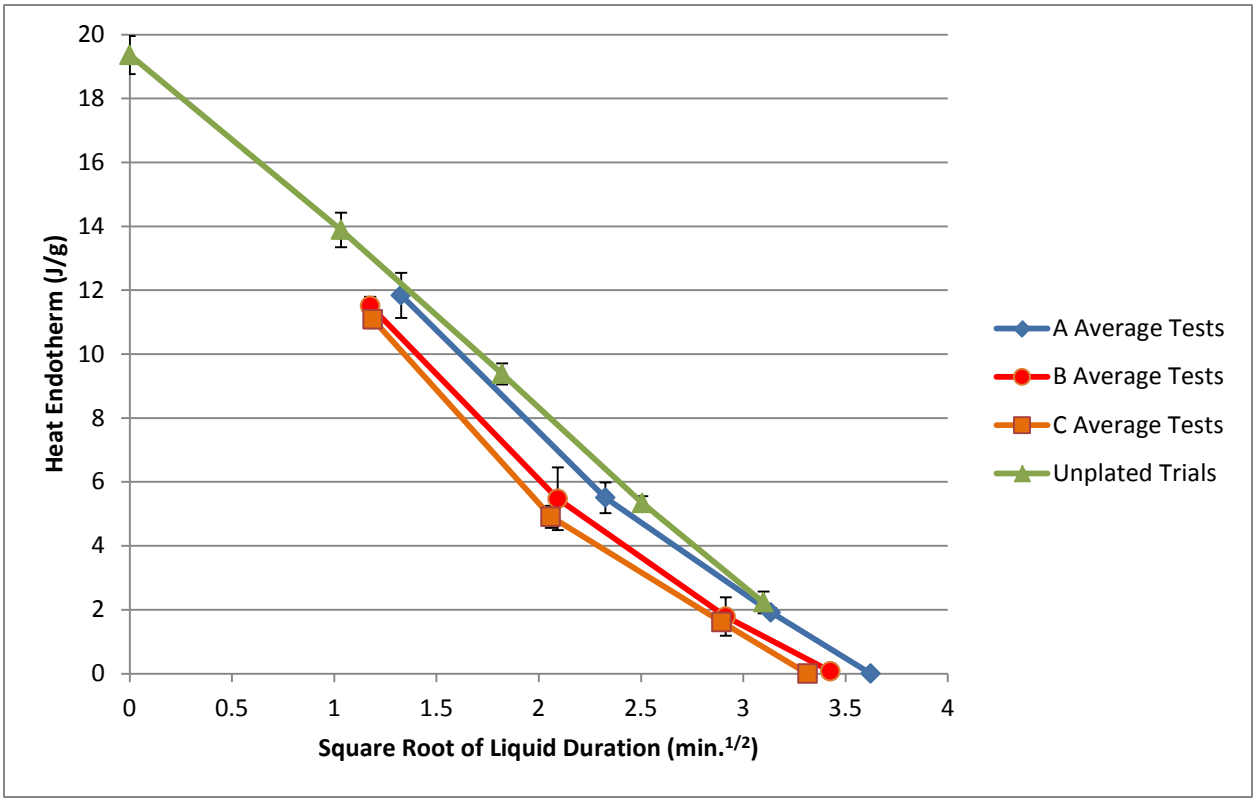

Figure 5-22 - Averaged Heat Endotherm Values for Cyclical Testing of Samples A, B, C, and Unplated 0.008" Braze Sheet

that sample A possessed roughly 1.5-2 J/g higher endothermic values during testing of all PPV braze sheet. The same rate of silicon removal was observed in all samples.

Using data from cyclical testing and the knowledge that isothermal solidification during these tests is in a parabolic relation with time, one can extrapolate the true enthalpy of melting on the first melt. This technique is a useful byproduct for calculating this enthalpy of melting was found through work by Corbin et. al [67]. Using the relation,

$$\Delta H_{meas} = \Delta H_{melt} - \Delta H_{exo}$$

Where ΔH_{meas} is the measured enthalpy of melting on the first peak of melting in the first pass of cyclical testing, ΔH_{melt} is the true enthalpy of melting for the sample, and ΔH_{exo} the true enthalpy of the aluminum nickel reaction. This equation can be rearranged to solve for the true enthalpy of the aluminum nickel reaction,

$$\Delta H_{exo} = \Delta H_{melt} - \Delta H_{measured}$$

Table 5.4 outlines these calculated true exotherms for all PPV samples. The table includes the average of the cyclical tests heating exotherms and endotherms. The linear relationship from Figure 5.22 is used to interpolate ΔH_{melt}. The difference between this term and the averaged endotherm gives the final ΔH_{exo}.

Table 5-4- Calculated True Endotherm and Exotherm during and prior to Melting for all PPV Samples

	Average Measured Exotherm (J/g)	Average Measured Endotherm (J/g)	ΔHMelt (J/g)	ΔHExo (J/g)	Total Exotherm
Unplated	0	19.36	19.36	0	0
A	-6.09	9.23	17.52	-8.29	-14.38
B	-6.66	10.58	16.94	-6.36	-13.02
C	-5.78	8.02	16.56	-8.54	-14.32

The average measured exotherm shown in the second column represents the intermetallic formation in the solid state prior to melting. The third, fourth, and fifth columns involve the convolution of continued intermetallic formation during melting which involves both exothermic and endothermic transformations. The calculated exotherm, ΔH_{exo}, does not include any intermetallic reaction prior to melting and is solely the Al_3Ni formed while the clad layer melts. Therefore, the sum of columns two and four yields the total energy of all reacted Al_3Ni. This data may be used to estimate the ratio of prereacted nickel to reacted nickel during melting. The prereacted value being the average melting exotherm visible prior to melting and the convoluted value is the remainder during melting. From the limited study performed, the results suggest that sample B has the least amount of reacted nickel at -6.36 J/g but had the highest amount of pre-react Ni (-6.66J/g) prior to melting of the clad. By this same method, samples A and C are calculated to have very similar ratios of prereacted to reacted Ni (approximately 1:1.4)

Optical work is shown in Figure 5.23 for A and B samples following cyclical testing. No silicon is visible anywhere in the sample as would be expected following a complete absence of endothermic values at the end of cyclical testing. The only phase visible, aside from the typical unplated braze sheet microstructure, was the Al_3Ni phase at the surface which is not expected to melt until 854˚C according to the Al-Ni phase diagram, see Appendix A. The post-test microstructure of sample C was observed to be very similar to samples A and B.

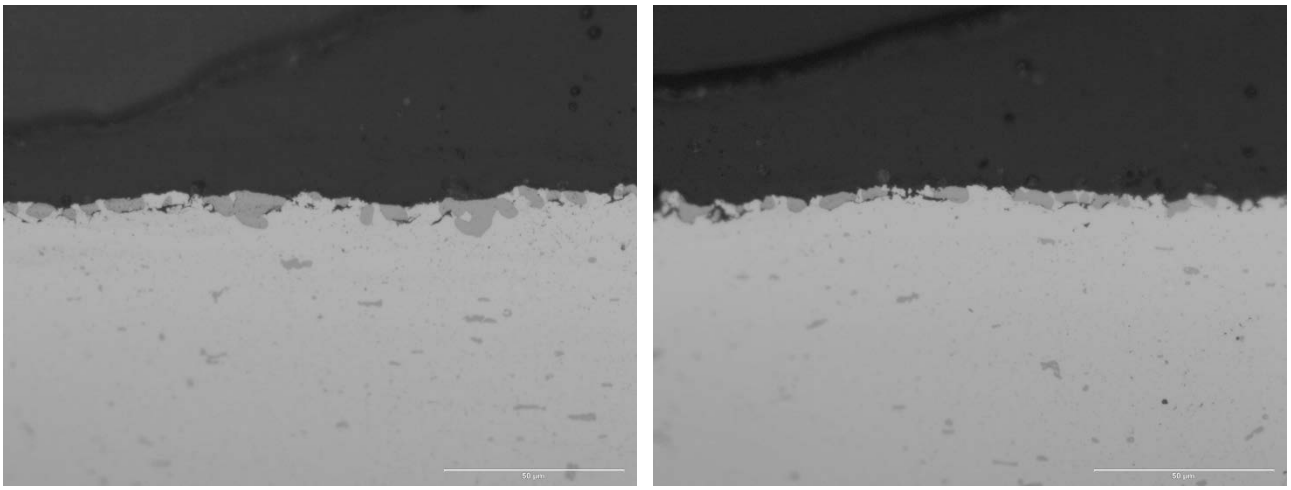

Figure 5-23 - Samples A and B after cyclic testing (50X, scale bar 50µm)

5.1.4 Process Variation Brazing Sheet Conclusions

The effects of an unspecified variation in the plating process of three modified braze sheets was examined using optical and thermal characterization techniques. Samples received from Dana Canada were 0.008”, 9% single side clad aluminum braze sheet. These samples were labelled as samples A, B, and C.

Overall, there was little discernable differences measured between samples A, B and C. Optical and SEM measurements revealed that slight variation in the thickness of surface nickel deposits. Using the characterization method outlined in Figure 5.2, Ni thickness was found to increase slightly from samples A to C, (5-15% variation depending on method of measurement, optical versus SEM measurement) but a decrease in surface coverage.

Samples B and C were measured to have up to 10% less coverage than sample A. Given the time consuming nature of these measurements and relatively small area analyzed (total area analyzed was only 1% of the entire coupon), any differences measured for samples A, B and C can be deemed to be within the realms of experimental errors

Consistent with the physical measurements of the Ni deposits, the thermal behavior of samples A, B, and C were found to be similar. The onsets (or beginnings) of the aluminum nickel reaction to form Al_3Ni were found to happen consistently at temperatures around 565˚C. As in previous work by Corbin et. al, the exotherm of intermetallic formation during heating was a one-time irreversible reaction [67]. This reaction typically onset at 565˚C and, if halted, would completely react by 563˚C for all samples (see section 5.1.3). The surface roughness and formation of the intermetallic were confirmed optically with A, B and C showing similar microstructures. For most samples (over 70%), holding at 560°C for just two minutes removed any indication of an exothermic peak at 565°C upon subsequent heating. After 5 minutes at 560°C, no exothermic reactions were observed which suggests that all the Ni has fully reacted with the Al in the clad to form Al_3Ni.

Isothermal and cyclical testing of liquid duration, and melt behavior, showed that an unplated sheet retained its clad layer longer than plated sheets. Overall, the unplated samples lasted 12 minutes whereas plated samples were between 8-10 minutes. This suggested that either more silicon was being transported, or that the rate of silicon diffusion into the core was faster for PPV samples. The former might be accounted for by the ternary Al-Si-Ni reaction which upon solidification yields (Al) + (Si) + (Al_3Ni). This means that some silicon is required for the ternary reaction to solidify which would be the case in plated sheets. As for the latter, it was not directly observed that the presence of nickel inhibited the rate of silicon removal across the clad/core interface. It would be interesting to see the calculated pseudo-binary diagrams from an Al-Si system with increasing values of nickel.

Although slight differences were noted in the microstructural and thermal characterization of the Ni deposits, these differences are marginal and lie within the limits of experimental errors. Therefore, it may be concluded that the different process parameters used for the plating of samples A, B, and C have negligible overall impact on the characteristics of the Ni plating and resulting braze reaction.

5.2 Oxide Growth and Disruption

The study of process variation in nickel modified braze sheets provided a framework for future thermal analysis and materials characterization of the oxide disruption mechanism. As discussed in sections 2.5 and 4.4, the surface of the braze sheets is uniformly covered by a tenacious layer of oxide, even during melting. The Al_3Ni intermetallic reaction documented in the previous chapter provides a method of breaking through this layer and promoting liquid clad flow. However, the manner by which the oxide layer is broken has never been studied to any real extent. The aim of this area of the project was to better understand both oxide and surface reactions as well as the process of oxide disruption.

Previous studies in section 5.1 were done on material that was found to have very small variation in plating characteristics and thermal/microstructure evolution. Hence, from 5.2 onwards, laboratory-generated surfaces and coatings have been developed and investigated to understand the interaction of the oxide layer and surface reactions during heating and melting.

The natural oxide layer present of the clad surface is quite miniscule (on the order of 10nm) and, as a result, is very difficult to characterize on its own. Variation of the layer, without any transition in structure or properties, was decided to be the best method to study disruption of the layer. This included chemical treatment and anodization of the oxide layer to create different surface conditions for the interaction of nickel. Recall from section 4.4, that the different surface altered samples either had surface oxides grown (by chemical treatment, anodization, or both), and also that some were stripped of their surface silicon by HF treatment.

5.2.1 Results of Oxide Growth Experiments

The design of oxide growth experiments is discussed in the methodology section in more detail. The treatments agreed upon received some combination of chemical treatment by HNO_3 and HF, and anodization using borax/boric acid (creating a barrier type layer). The purpose of adding a barrier layer to the surface was to enlarge the oxide layer for

characterization purposes, as well as to study any critical thickness where no nickel can be transported across the oxide. All samples used in this section of study were 0.008", 12% SS braze sheet. These braze sheets were exactly the same as previous braze sheets used in the PPV studies, except for a larger clad layer thickness. The samples created for this study included:

- A – As Received
- B – Heavy Surface Preparation (5min. HNO_3 + HF)
- C – Thermal Oxide Grown (350˚C, 24 hours)
- D – Heavy Surface Preparation (same as B), Barrier Type 40V
- E – As Received
- F – Light Surface Preparation (30s NaOH, 30s HNO_3)
- G – Light Surface Preparation, Barrier Type 10V
- H – Heavy Surface Preparation (30s NaOH, 2 min. HNO_3 + HF)
- I – Heavy Surface Preparation, Barrier Type 10V
- J – Light Surface Preparation, Barrier Type 40V
- K – Heavy Surface Preparation, Barrier Type 40V

Section 4.4.2 outlines the results for samples A, B, C, and D which were studied previously by Dana Canada Corporation. Section 4.4.3 outlines the method and reasoning behind the creation of samples E-K. Light surface preparation refers to a surface treatment of sodium hydroxide followed by nitric acid. Heavy surface preparation involves chemical treatment of sodium hydroxide followed by a mixture of nitric and hydrofluoric acid. Samples E-K were examined under SEM-EDX and Fourier Transform Infrared Spectroscopy (FTIR) techniques. Certain samples from the same test group had their surface oxide layers closely characterized using Transmission Electron Microscopy (TEM). These samples included E-G, J, and K.

Samples E-K are organized into Table 5.6. There were three variations to the surface layer which were investigated. The effect of surface preparation itself in samples E, F, and H and the effect of a thicker oxide anodized onto an LSP and HSP sample. The purpose of anodization was to see if a critical oxide layer could be created such that the aluminum

nickel reaction is delayed or halted. For the purposes of clarity, samples E-K will be referred to later in this section by their surface preparation and the degree of barrier type anodization, if any. For instance, sample G will be referred to as LSP 10V.

Table 5-5 - Oxide Disruption Naming Convention

	As Received	Nitric Acid (LSP)	Nitric/HF (HSP)
As Received	E	F	H
Barrier 10V	-	G	I
Barrier 40V	-	J	K

SEM EDX testing of the surface was done under the same methodology as outlined in section 4.4.2. The results of these tests are shown in Table 5.6. A lower amount of carbon was found in all samples which had undergone heavy surface preparation (samples H, I, and K) and in sample G (LSP 10V). The presence of fluorine was only found, to a significant amount, in samples which also had undergone heavy surface treatment. The effect of hydrofluoric and nitric acid is best observed in the amount of silicon detected on the surface. HSP samples showed a fourfold decrease in silicon content.

Table 5-6 - SEM-EDX Measurement of the Clad Layer of Oxide Disruption Samples

ID.	Element (Weight %)					
	C	O	F	Al	Si	Total
A	9.3	0.9	0.7	86.4	10.4	107.8
B	4.7	1.0	1.1	93.8	2.2	102.8
C	3.0	1.8	0.0	90.3	12.5	107.7
D	3.3	6.4	0.5	92.5	2.1	104.9
E	3.7	1.4	-	87.1	10.9	103.2
F	3.5	0.9	-	88.4	12.0	104.8
G	2.5	2.6	-	85.7	13.0	103.8
H	2.8	0.5	1.4	92.7	2.9	100.4
I	3.3	2.4	0.3	92.0	3.0	101.0
J	4.1	10.5	0.1	89.7	11.9	116.3
K	2.2	7.4	0.4	91.7	2.6	104.3

The full results for % oxygen composition are shown in Figure 5.24. Sample J (LSP 40V) yielded the largest surface oxide, whereas sample H (HSP) showed the lowest. A decreasing trend in the surface oxygen composition from as received (E) to LSP (F) to HSP (H) can be seen as well. Heavy surface treatment had an effect of lowering the oxygen percentage for all cases when compared to light treatment. Both of these treatments were immersed in sodium hydroxide first which should have removed an equal amount of the surface oxide layer. Whether nitric acid was as effective at regenerating the oxide while in the presence of hydrofluoric is debatable. This may explain why there is a decrease in HSP surface oxides. Another possibility is the presence of fluorine embedded in the sample surface may have altered or deterred the oxide.

FTIR measurements were performed in the 4000-400 cm^{-1} spectral range. 32 spectra were co-added for each sample and the resolution was 4 cm^{-1}. All samples were measured in a dry N_2 exposed environment. The abundance of oxygen under FTIR was contrasted the results from SEM-EDX surface scans, see Figure 5.25. These were found to be in good agreement.

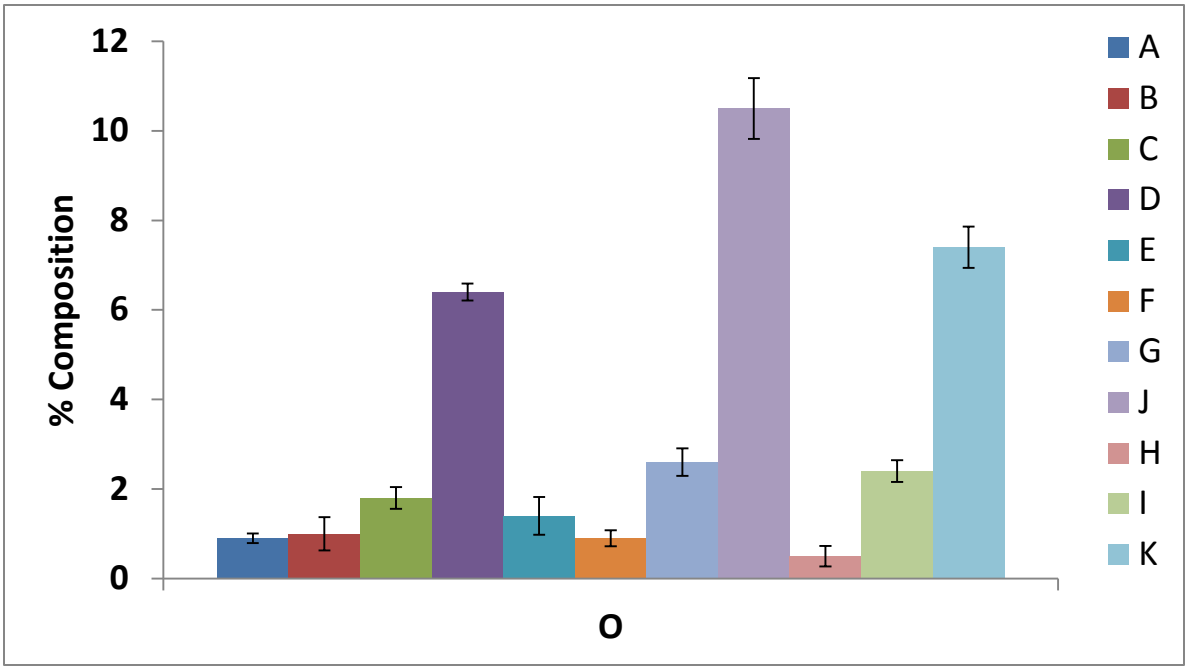

Figure 5-24 - SEM-EDX Measurement of Percent Oxygen on the Clad Surface of Oxide Disruption Samples

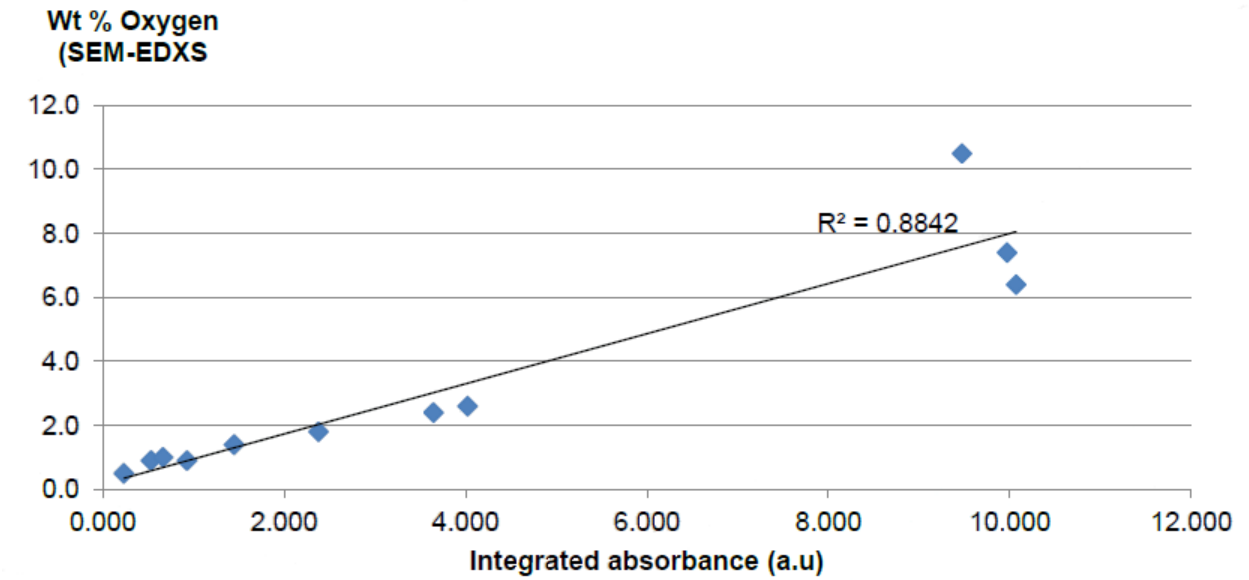

Figure 5-25 – Comparing FTIR Measurement of Clad Surface with SEM-EDX (Courtesy of Dana Canada)

FIB-SEM studies, discussed in section 4.4.2, attempted to measure the thickness of the oxide layer, see Appendix E. Due to the scale of the oxide thickness, exact measurements could not be resolved with this technique. Five specimens were sectioned using focused ion beam and then placed in an FEI Tecnai Osiris TEM. Samples were coated in a Pd-Au coating using a Denton Desk-IV high vacuum sputter coater. They were then cut using a FEI Helios NanoLab-650 FIB-SEM and placed in TEM under a high angle annular dark field. The TEM measurements and their standard deviations are shown in Table 5.7. Most samples were resolved to a range of at least ±2 nm. The same trend that is seen in the SEM-EDX measurement of different surface preparations can be seen in TEM with more accuracy. The HSP sample had the thinnest oxide and that the hydrofluoric acid inhibits oxide growth even though the samples were exposed to nitric acid as well for the same two minutes. Thirty seconds of nitric acid in the LSP samples was enough to grow back half of the original native oxide seen in as received specimens. Anodizing to 40V added as much as 60nm to the surface oxide, and was more effective in HSP samples. This is most likely due to the effects of surface silicon, or lack thereof in HSP samples, when anodizing discussed in section 2.4.3.

Table 5-7 - TEM Measurement of Oxide Thickness for Selected Oxide Disruption Samples (Courtesy of Dana Canada)

Specimen	Oxide Thickness	Standard Deviation
AR	26 nm	±2 nm
LSP	13 nm	±4 nm
HSP	5 nm	±1 nm
LSP 40V	60 nm	±1 nm
HSP 40V	66 nm	±2 nm

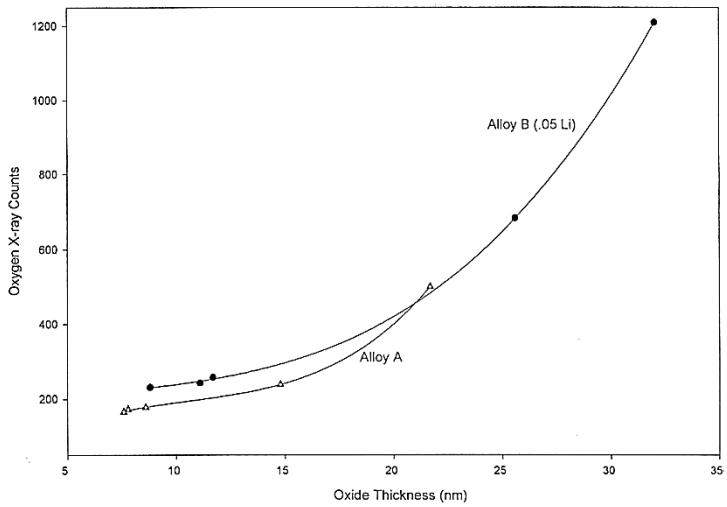

Figure 5-26 - WDS Measured Oxygen versus Measured TEM Thickness for Alloy A (Al10Si) and Alloy B (Al10Si0.05Li) [74]

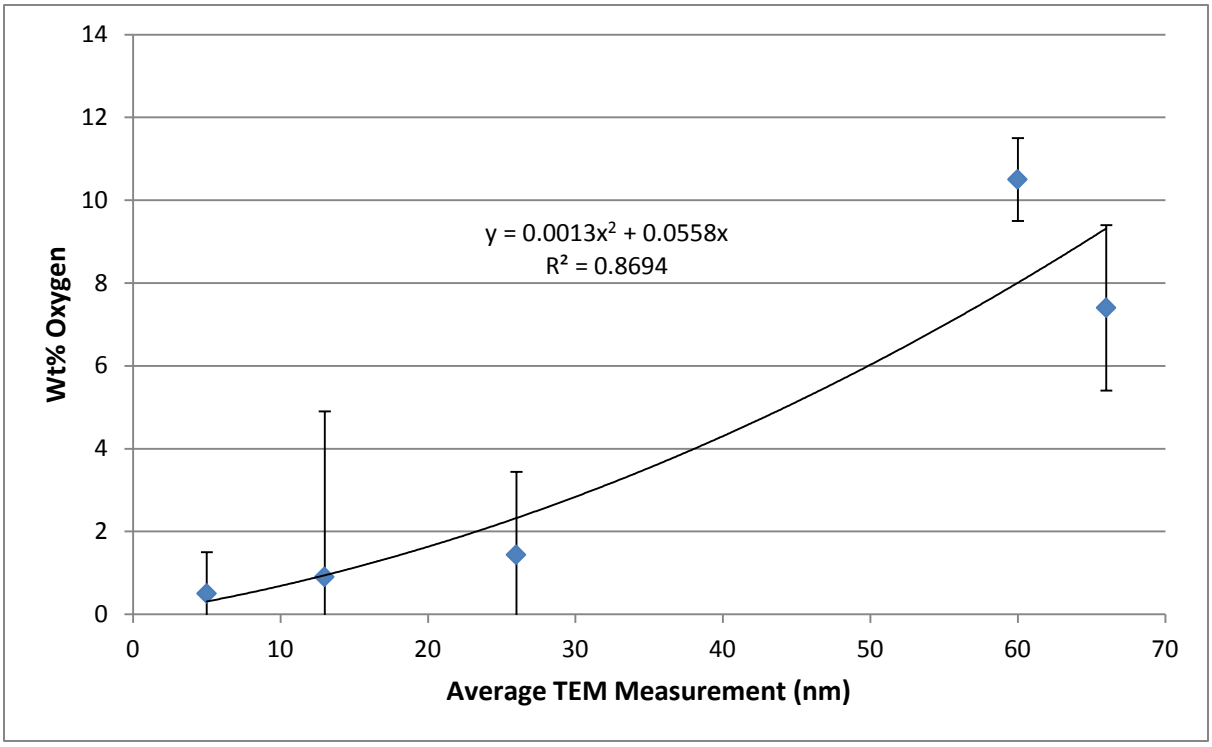

Figure 5-28 - EDX Measured Oxygen versus Measured TEM Thickness of the Clad Region of Oxide Disruption Samples

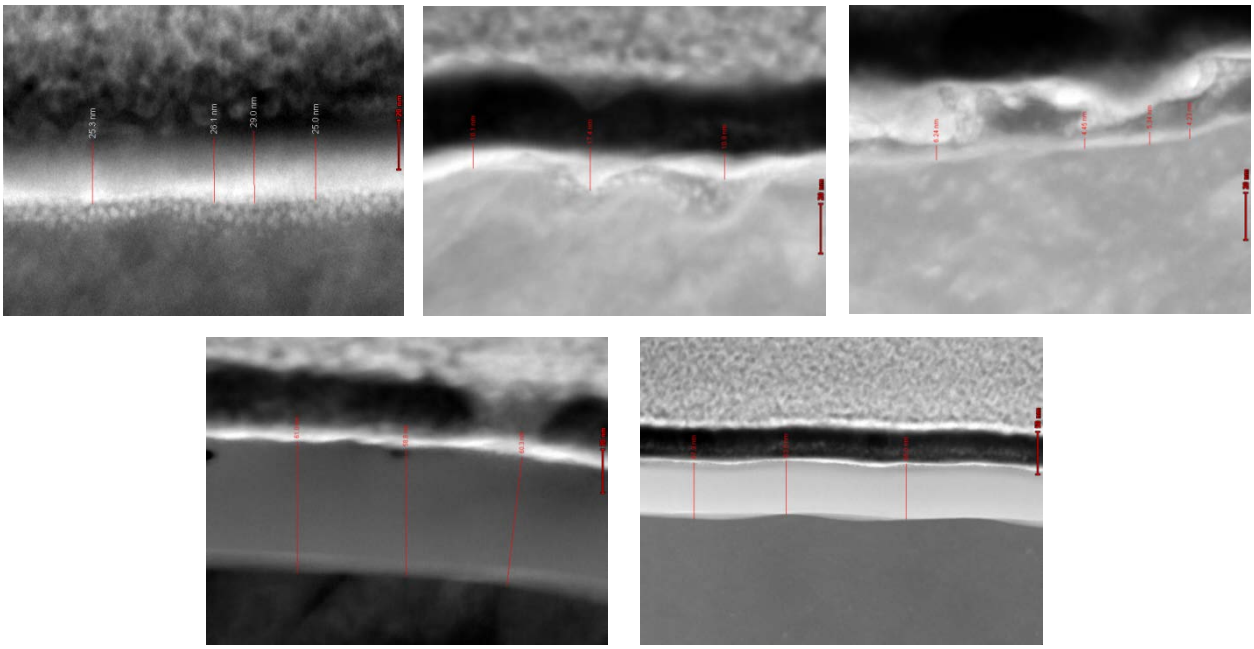

Figure 5-27 - TEM shots of AR, LSP, HSP, LSP40V, and HSP40V, Scale Bar 20nm (Courtesy of Dana Canada)

Previous literature had shown that these accurate TEM measurements could be plotted against the SEM-EDX (WDS in the paper [74]), see Figure 5.26. These curves could then

be used to provide a more cost effective method of measuring oxide thickness in the future [74]. One could simply measure the oxide content under EDX and compare it to the curve for a close approximation of actual oxide thickness for this particular braze sheet, see Figure 5.27. Imaging from the TEM can be seen in Figure 5.28. Samples which had been surface treated (LSP, HSP) appeared to have a rougher, more tumultuous oxide layer when compared to those anodized to forty volts.

5.2.2 Observation and Measurement of Nickel Reaction

DSC testing of samples E-K involved bringing each sample to 590˚C at 10˚C/min prior to cyclic testing alternating between 490˚C and 590˚C described in Figure 5.19. When testing PPV samples, the one-time irreversible Al_3Ni reaction could only occur and be observed on the first pass of 565˚C. Recall that unplated braze sheets which have no nickel interaction melt at the Al-Si eutectic (577˚C) and will show a DSC trace similar to Figure 5.8. Figure 5.29 shows the DSC trace for as received and unsputtered braze sheet.

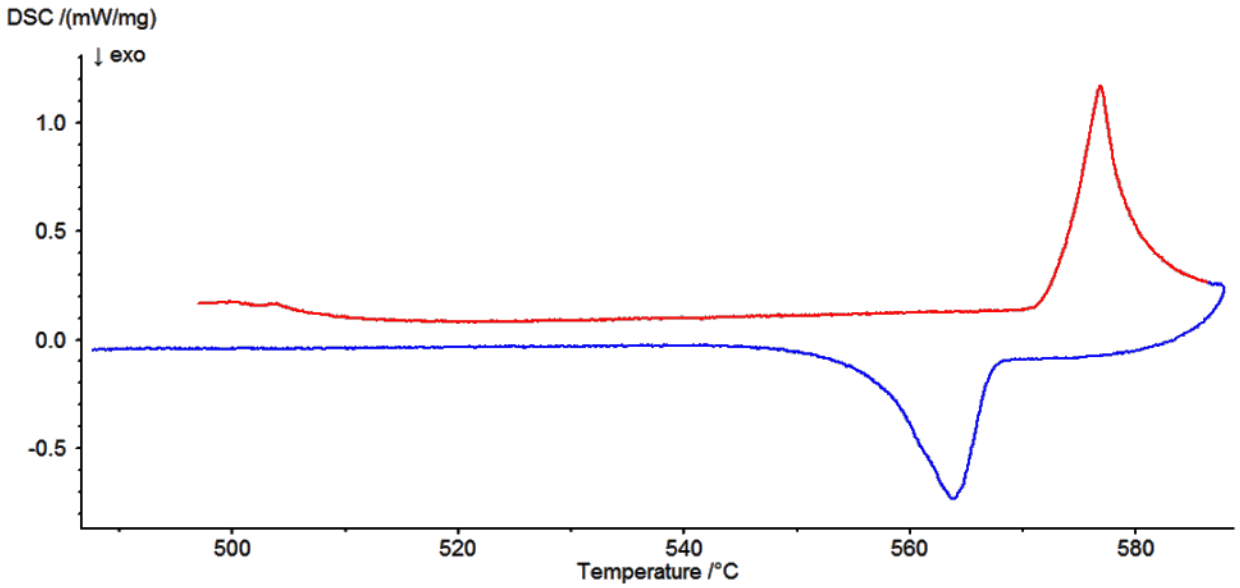

Figure 5-29 - Typical DSC Trace of 0.008", 12% SS, H24, 3003/4045 Aluminum Alloy Braze Sheet

Figure 5.30 shows a typical heating and cooling curve on the first 590˚C pass, in this case for sample LSP sputtered with 0.5µm nickel. The exotherm in all sputtered samples was much more subtle than any previous testing with samples A, B, and C. Here the solid state "pre-reaction" exotherm was evident by a gradual shift in the baseline in the exothermic

direction up until the melting endotherm. The melting endotherm shown here initiates and peaks exactly the same as the Dana samples, only the intermetallic reaction showed any differences. The DSC curves were smoothed for data analysis, however, smoothing was limited to ensure the integrity of the data and the shape of original curve was maintained.

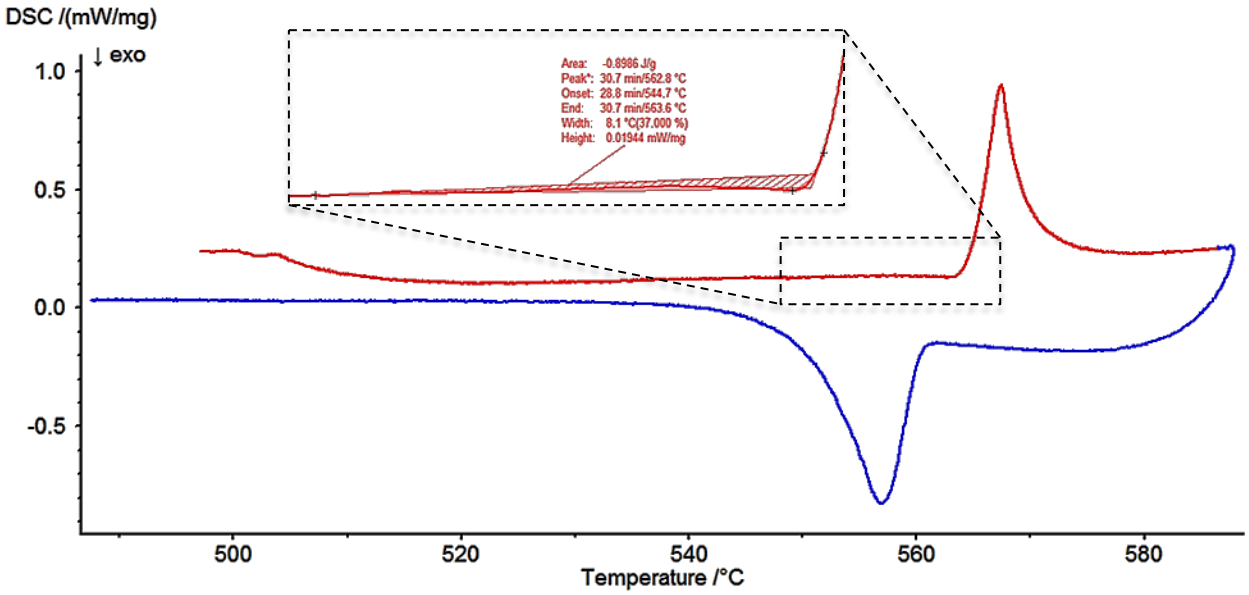

Figure 5-30 - Example Initial DSC Curves for an LSP Sample with 0.5um Nickel Layer

Sample LSP (treated in nitric acid) is an example of a reacting sample, and is in fact one of the best cases of an observable solid state “pre-reaction” exotherm. Other samples would not show an exotherm or even a deviation from the baseline. Several possibilities may be attributed to the absence of this exotherm. It is possible that the aluminum nickel reaction predominantly occurred in solid state, which Corbin et al. has shown to yield no exotherm [67]. The thicker oxide, as a barrier, could inhibit the diffusion of the nickel to the aluminum (or vice versa) from contacting the aluminum and not until after melting and exudation can the nickel react with molten aluminum. There is also the possibility of influences from altered chemistries of the normal surface oxide due to chemical residuals such as boron, nitrogen, and fluorine from the oxide growth procedure.

A proved method for discerning if the braze sheet surface oxide was posing as a barrier to the penetration of nickel was to observe the endotherm and exotherm onsets and peaks. If nickel was to diffuse through this oxide, the melting endotherm and freezing exotherm would deviate to lower temperatures dictated by the Al-Ni-Si ternary diagram. That is, the

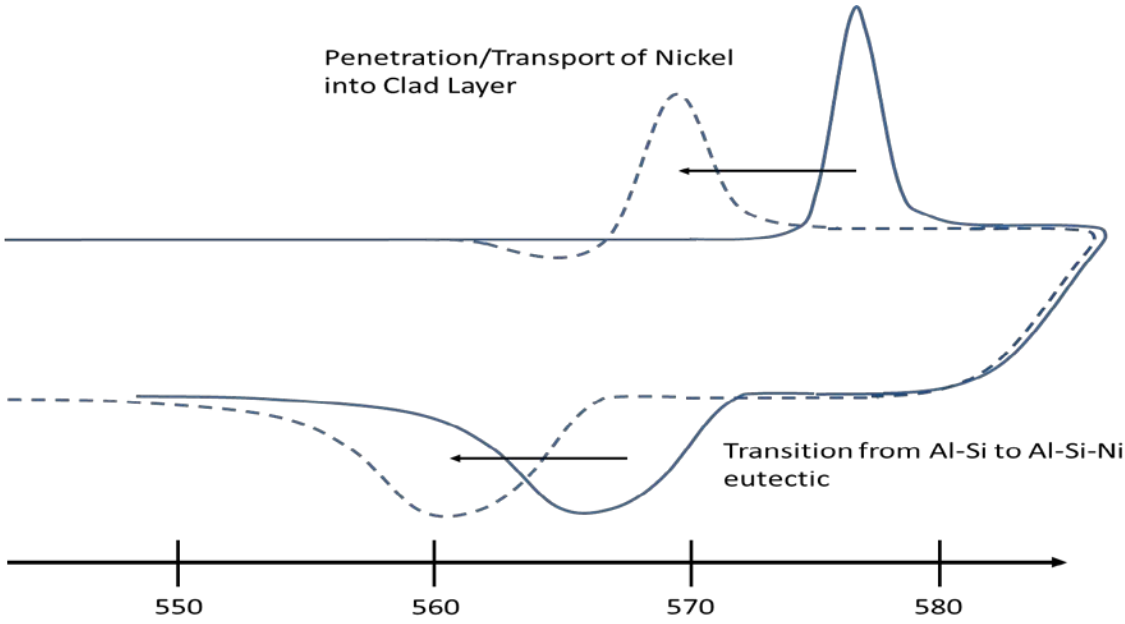

Figure 5-31 - Schematic of Transition from Al-Si Eutectic to Al-Si-Ni Ternary Eutectic under DSC

melting peak position illustrates whether melting is of the Al-Si (577˚C peak) or Al-Ni-Si eutectic (565˚C peak). Figure 5.31 illustrates this concept.

Of interest were samples where the nickel reaction was suppressed entirely, in other words the clad layer formed an Al-Si melt while the nickel layer rested above on the tenacious surface oxide, confirmed in later studies (see section 5.2.3.1). This concept was easy to distinguish under DSC using the aforementioned principle. Figure 5.32 demonstrates this

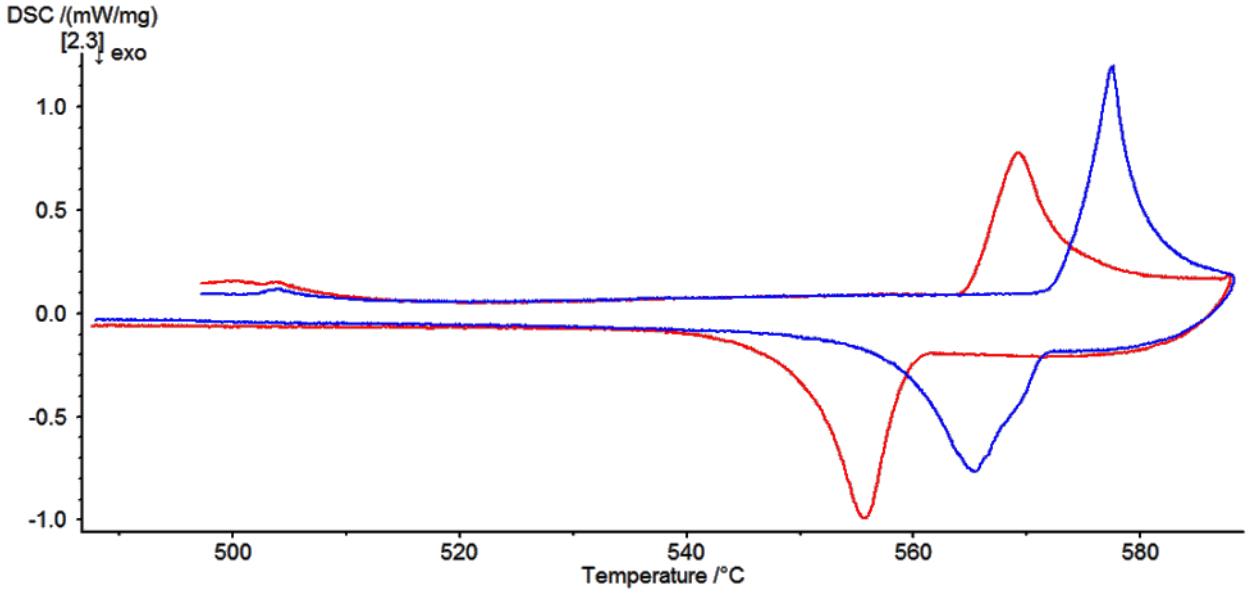

Figure 5-32 - Initial DSC Traces of Sample AR (Red) and LSP 40V (Blue) sputtered to 0.25um Ni

concept in samples AR and LSP 40V sputtered with 0.25µm of nickel. No other sample was more resilient in delaying the nickel reaction than LSP 40V, and this was proven further in cyclical testing which was analyzed to reveal the true exothermic values of the nickel aluminide reaction.

Table 5-8 - Calculated True Enthalpy of Aluminum Nickel Reaction Exotherms for Oxide Disruption Samples

	AR	LSP	HSP		HSP	HSP 10V	HSP 40V		LSP	LSP 10V	LSP 40V
0.5 um	-11.86	-13.8	-7.59		-7.59	-5.64	-2.21		-13.8	-4.99	-5.43
0.25 um	-9.38	-1.29	-7.22		-7.22	-5.25	-3.62		-1.29	-6.44	0
0.1 um	-1.36	0	-0.52		-0.52	-2.79	0		0	-1.78	0

Recall in section 5.1.3 that true enthalpies of melting and exothermic reaction could be calculated from liquid duration testing, due to the parabolic relation of isothermal solidification with time. Table 5.8 outlines the calculated true exotherms (i.e. the exotherm which is convoluted with melting) for all oxide disruption samples following cyclical testing of three samples of each condition. From the results, some trends began to appear. Samples with 0.1µm of nickel showed little to no exotherms, which is expected since Ni is required for the reaction, a reduction of which would lower the magnitude of the exotherm. In fact, in nearly all the cases, for a given surface preparation condition, a reduction in Ni sputtered thickness results in a reduced exothermic reaction. Again sample LSP behaved with the strongest exotherms except for an anomaly occurring for those samples sputtered with 0.25um nickel. This result was especially strange because this particular sample had a larger exotherm by one magnitude over the other LSP samples. HSP samples exhibited the lowest exotherms even though the oxide layer is only an average of 5nm on the surface and the lowest of any surface condition. This is most likely due to the removal of surface silicon making it difficult for the ternary system, (Al) + (Si) + (Al_3Ni), to form and hence for Al_3Ni to form. Thickening the oxide seems to reduce the nickel exotherm for all cases, and in some the effect is an exotherm of zero. Sample LSP40V in particular seemed to be effective at achieving this.

Nickel thickness dictated whether enough nickel was present to withstand oxidation and solid state reaction with the surface clad. Proof of this oxidation will be discussed further in

XPS studies detailed in section 5.2.3.1 Only in certain cases was the oxide impenetrable enough that no nickel could get through prior to melting and typically these were cases of oxide thicknesses above 30nm (samples LSP 10V, LSP 40V, and HSP 40V).These thicker samples (LSP 40V (60nm) and HSP 40V (66nm)) and one surface condition (samples LSP 10V (~35nm)) showed no exotherms for the lowest nickel thickness and only slight exotherms at higher nickel thickness values. Conversely, for samples having thinner oxides, exotherms were always higher and above zero, even at the lowest nickel thickness tested. The overall microstructures for thicker oxide samples show that nickel is being slowed down, or rendered immobile on the surface, at temperatures near to melting of the surface clad. These trends are also observable in the cyclical testing of all samples.

5.2.3 Effect of Oxide Thickness

DSC testing similar to those conducted in section 5.1.4 was done for samples E-K. Samples were heated to 590˚C and then heated between 490˚C and 590˚C at 10˚C/min. These tests were again done in argon at flow rates of 150mL/min. Testing was done on three separate coupons for each sample type for validity. Appendix G outlines the results for 0.1, 0.25, and 0.5µm respectively. Note that for almost all samples the initial endotherm has been depressed suggesting the aluminum nickel reaction has occurred to some effect, even if it does not register as a peak on the DSC traces.

Trends in oxide thickness were most easily observed in the case of 0.5µm sputtered nickel samples. Sufficient nickel was present at the surface that a sample would react if able to do so, see Table 5.8. Samples received different surface preparations and were anodized to two distinct heights as dictated by the supplied voltage. Samples receiving 10V would have an oxide thickness of roughly 30-35nm and at 40V oxide thickness was shown by TEM to be 60-66nm. Recall from section 4.4.3 that all oxides would be largely composed of a barrier type oxide with little to no porosity at its surface.

The time for complete isothermal solidification of the clad layer could not be directly measured, due to an insufficient cycle time in the experiments (i.e. ≈18 minutes). Only the slope and the initial endotherm were recorded as in Table 5.9. Samples were then arranged

into three respective comparisons; surface effects without anodization (SP), Light Surface Prepared (LSP), and Heavy Surface Prepared (HSP). Samples designated LSP and HSP gave insight into the effect of surface preparation but also gave information on the effect of oxide thickness. Unplated in all cases has no sputtered nickel on the surface.

Table 5-9 - Liquid Duration Behaviour of Oxide Disruption Samples Sputtered with 0.25um Nickel

	Average Weight	Slope	Initial Endotherm (J/g)	R^2
Unplated	10.1	-5.96	28.214	0.9984
AR	9.85	-5.53	31.646	0.9933
LSP	10.2	-6.51	31.827	0.9937
LSP 10V	10.2	-5.35	33.337	0.9996
LSP 40V	9.96	-4.98	32.855	0.9974
HSP	9.8	-5.75	26.866	0.9969
HSP 10V	9.9	-5.76	23.277	0.9969
HSP 40V	10.35	-4.88	27.732	0.9928

The unplated condition showed a lower endotherm than most samples run in cyclical testing. It was assumed that this difference was a product of silicon content and clad thickness variance inherent in the post-rolled braze sheet. HSP samples showed the lowest initial endotherms and slopes. This can be attributed to the lowered silicon concentration in the clad layer since the surface silicon has been removed. Whether there was an effect of embedded fluorine in the surface oxide was not determined. LSP samples showed a longer liquid duration than the as received case (Sample AR). Recall that the surface oxide was removed with sodium hydroxide and only a minimal exposure to nitric acid was supplied. This made the oxide thinner than the as received condition.

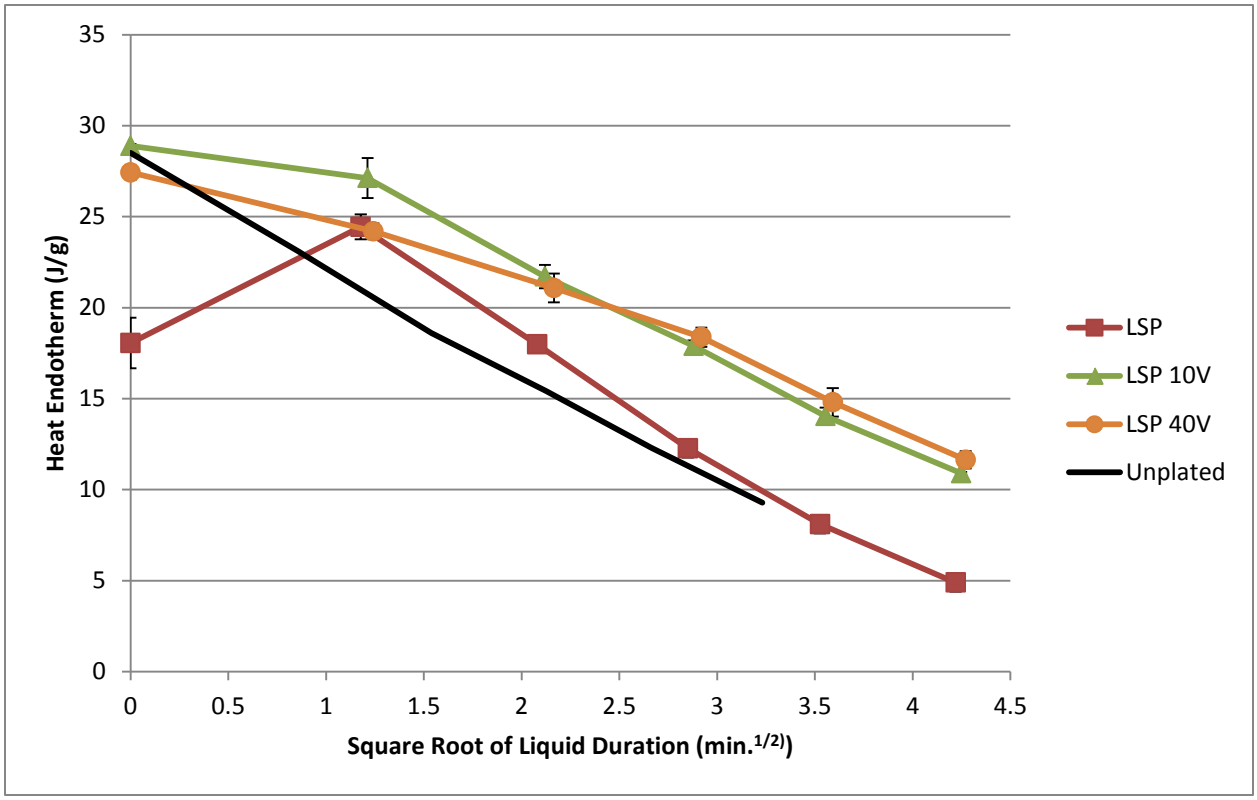

Figure 5-33 - Cyclical Liquid Behaviour for Light Surface Preparation Conditions with 0.5um Sputtered Nickel

Figure 5.33 shows the averaged cyclical behavior of LSP samples sputtered with 0.5um nickel compared to the unplated braze sheet. A depressed initial endothermic value, due to a convoluted exothermic/endothermic event, was observed for all LSP samples, indicating that some interaction with the nickel layer had been achieved. Sample LSP received no anodization, had the thinnest oxide (~13nm) and showed the largest exotherms (i.e. lowest initial endotherm), refer to Table 5.8. The anodized specimens showed only a slight drop in the initial endotherm comparatively. A transition in the slope of sample LSP40V at the fourth data point was observed during this testing. The change in slope showed that the rate of liquid removal in the LSP40V sample was initially slower (i.e. from ≈ 1 to 3 $min^{1/2}$), but obtained a rate similar to the LSP and LSP10V samples at longer hold times. This effect will be discussed in more detail at the end of this section.

The behavior of heavy surface prepared samples (HSP) is shown in Figure 5.34. Again the trends in liquid duration were not immediately clear. The samples anodized to 10V behaved counter to samples held to 40V, showing the lowest liquid duration. This difference could be attributed again to differences in silicon content across braze sheets supplied. The thinnest

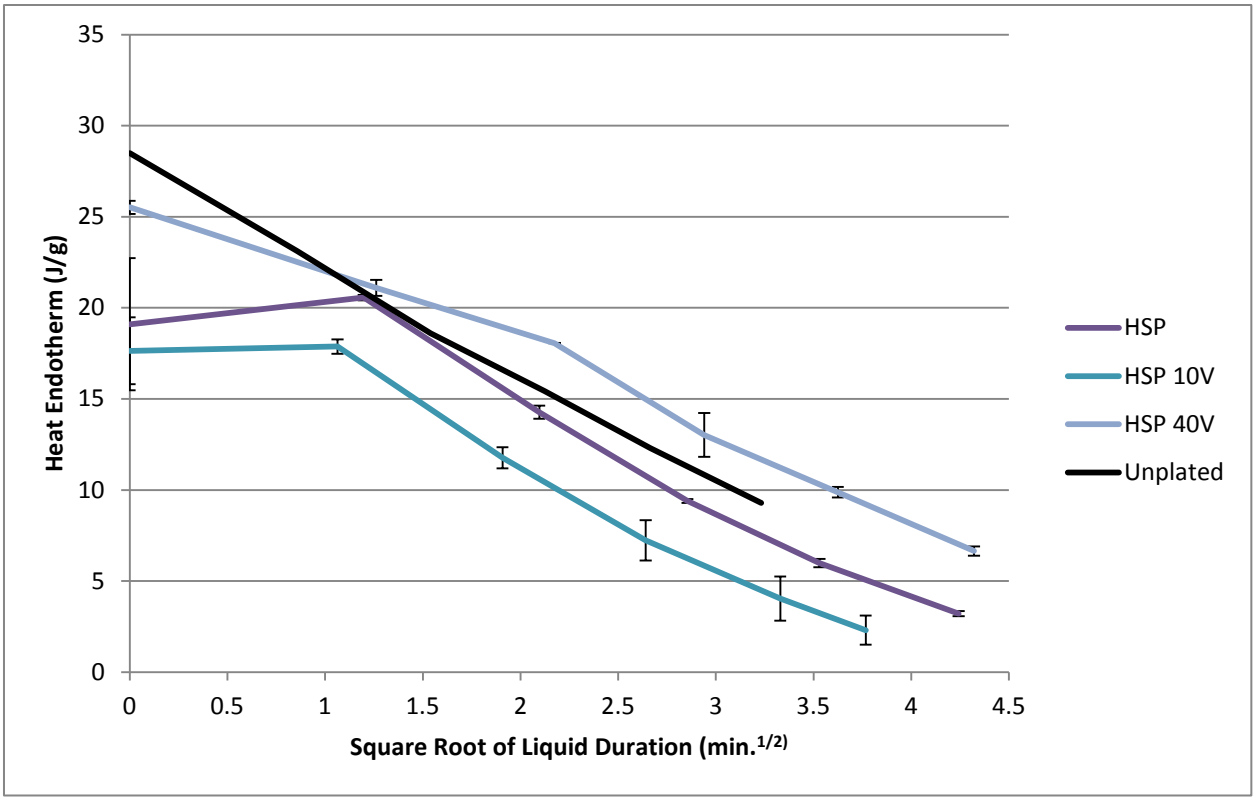

Figure 5-34 - Cyclical Liquid Behaviour for Heavy Surface Preparation Conditions with 0.5um Sputtered Nickel

oxide showed the largest exotherm, however, the 10V sample deviated heavily as well. A similar transition in the slopes of sample HSP40V was seen.

The strange behavior of sample HSP10V and LSP10V was speculated to be due to a critical barrier layer thickness discussed in Grosskreutz et. al, and Choo et. al. [61][75]. In both articles, a critical barrier oxide thickness separates two very different failure mechanisms of the oxide film. In Grosskreutz, this oxide thickness is described to be 500Å, or 50 nm, and in Choo et. al. it is described to be below 30V in ammonium borate solutions,

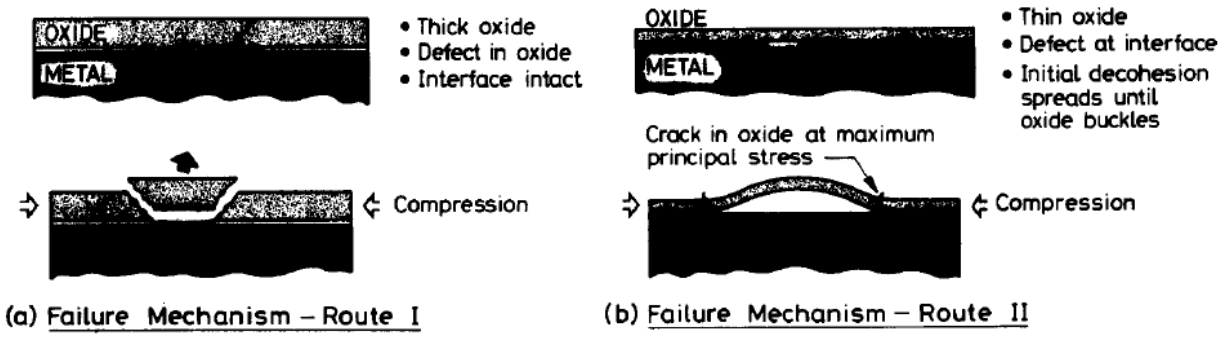

Figure 5-35 - Failure Mechanisms of Thin and Thick Oxide Films [76]

just under the borax/boric acid solution in this study. In section 5.2.1 it was shown through TEM studies that samples LSP 40V (60 nm oxide thickness) and sample HSP 40V (66 nm) are above this thickness, whereas Samples LSP 10V and HSP 10V (≈35 nm) are below. For oxides below this critical thickness, failure was observed to occur in research studies along the substrate slip steps and above, failure occurs normal to the tensile axis (which lies at right angles to the cracks). [61][75]. Evans et. al has also shown that a metal oxide above some critical thickness will fracture and break off whereas a thinner oxide will preferentially delaminate, see Figure 5.35 [76]. It is believed this alternative failure mode for thinner oxides may be breaking the oxide prematurely and promoting liquid flow much more readily than even the as received case.

Another parameter of interest that was discussed in the observation and measurement of the nickel reaction section was the onset of the melting endotherm. This could be projected across the entire liquid duration, see Figure 5.36, which yielded some interesting results. It became clear that nickel was not penetrating into the molten clad layer immediately in some samples. One sample which showed particular resilience in holding back the nickel was

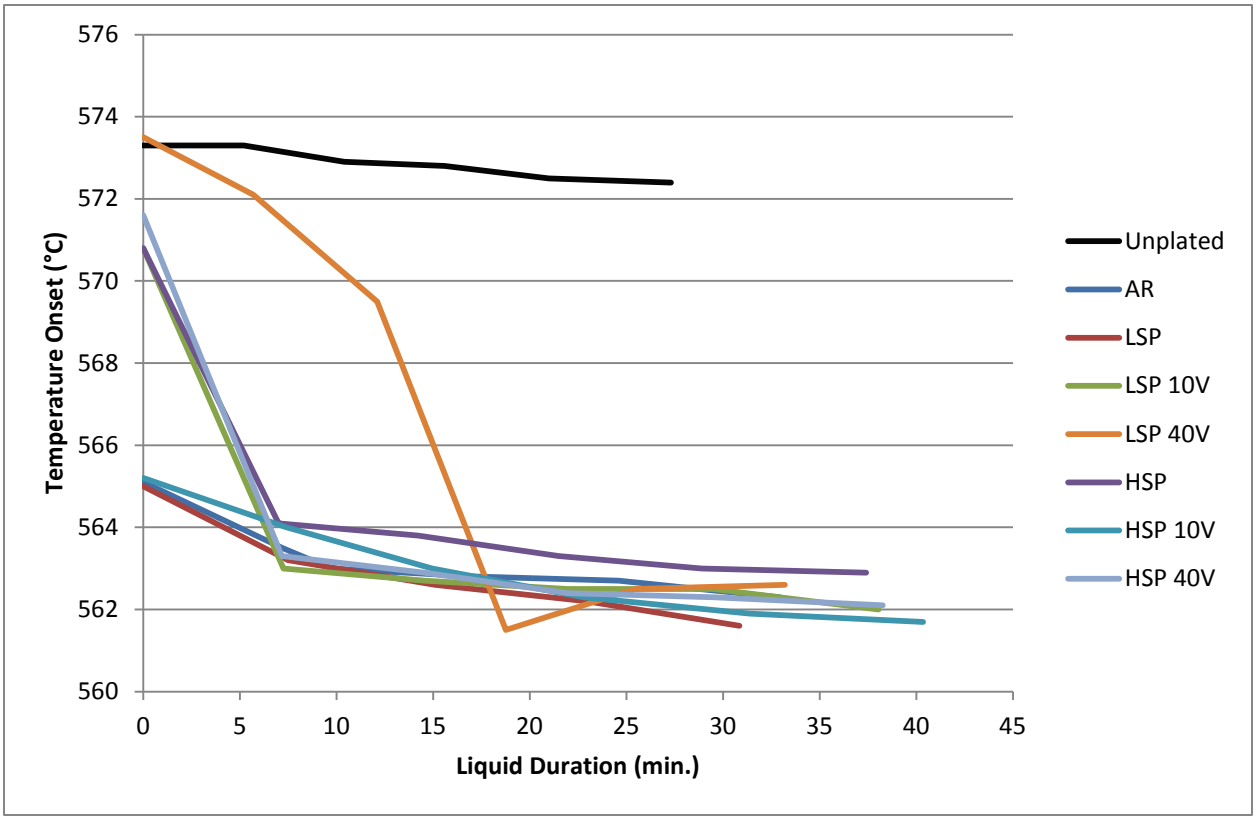

Figure 5-36 - Onset Temperature of Melting Endotherms for all 0.25um Ni Samples

Sample LSP 40V. In the figure, we can see that sample LSP 40V actually melts at the Al-Si eutectic temperature for the first peak of melting. Following onto later peaks, nickel slowly becomes added to Al-Si melt until the Al-Si-Ni ternary melt is achieved at the fourth peak.

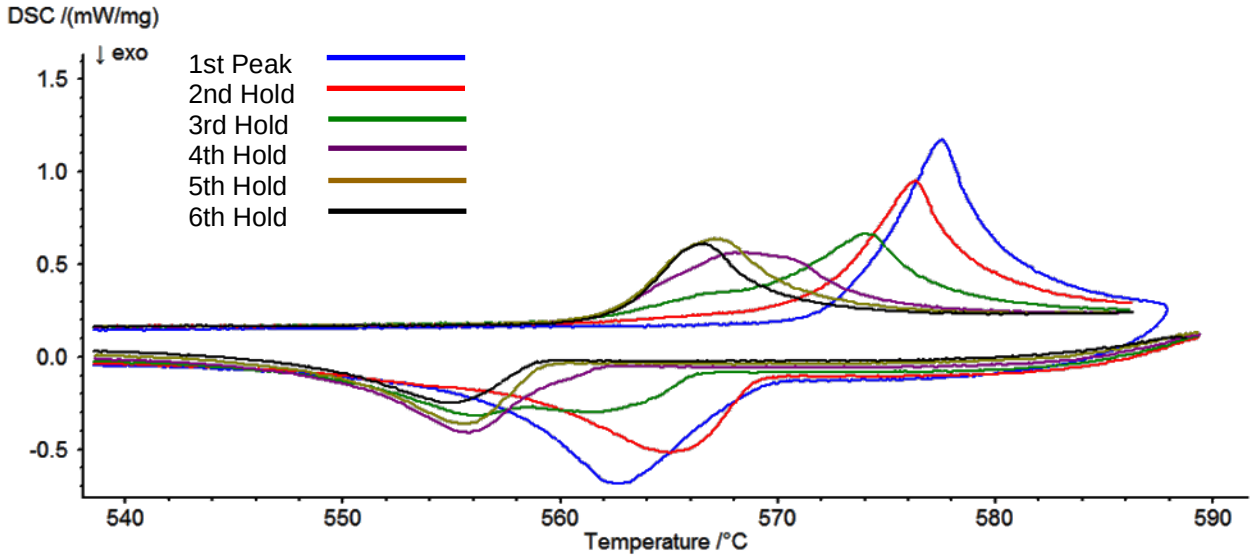

Figure 5-37 - DSC Trace Showing all Cyclical Peaks for LSP40V 0.25um Ni

This progression under DSC is shown in Figure 5.37. It was theorized that Sample LSP40V was actually tracing the line between the Al-Si eutectic and the Al-Si-Ni eutectic on the ternary diagram. Figure 5.38 illustrates this concept showing a magnified view of both the binary Al-Si eutectic (e) and the ternary Al-Si-Ni eutectic (E) located on the Al-Si-Ni ternary diagram constructed by Richter et al [38]. Points are shown along the path from binary to ternary eutectic and projected onto data from the onset temperatures of LSP 40V (shown in

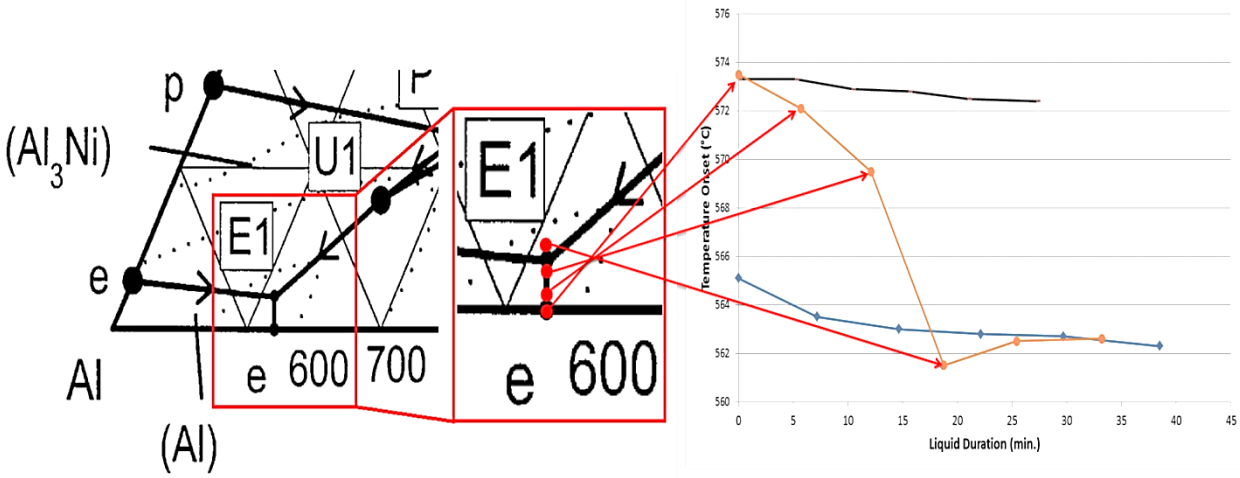

Figure 5-38 - Relationship between Binary/Ternary Eutectic Points and Sample LSP40V Onset Temperatures

between unplated in black and AR in blue). The oxide between both Al-Si and Ni seemed to delay the ability for the ternary system to form for several cyclical passes. It was not confirmed whether the onsets of melting perfectly traced this line on the ternary diagram.

5.2.3.1 XPS Studies of a Critical Oxide Thickness

Sample LSP 40V, 0.25µm nickel, possessed a thick enough oxide layer such that nickel was not immediately transported and reacted with the Al-Si clad layer. To better understand what was occurring during these DSC trials XPS was conducted on the following samples:

- As-Received (Sputtered)
- Heated to 590˚C, and Cooled
- Isothermally Held at 590˚C (10min)
- Two Cyclic Peaks, and Cooled

All samples were punched from close locations on the sputtered sheet and held in the same atmosphere with a two purge evacuation prior to running (except the as-received condition). For the two cyclic peaks testing a sample was heated to 590˚C, cooled to 500˚C, brought again to 590˚C, held for one minute and then cooled. The purpose of this particular test was to see the effect, if any, on a surface that was melting and cooling repeatedly versus holding a constant liquid in the isothermal case. The idea was that perhaps cyclic fatigue may be occurring on the surface oxide through cyclic testing, or that perhaps a maintained liquid surface was more detrimental to the oxide.

Surface scans were done prior to any depth profiling of any of the samples. Elements scanned were Al 2p, C 1s, Ni 2p, O 1s, and Si 2p. During all scans it was found that carbon peaked for the as-received sample but was not prevalent on any other sample. This was most likely grease or dirt which had been on the sample during handling or fabrication. Most interesting for all samples were the Ni 2p and O 1s traces.

Traces for O 1s showed that only the as received sample consisted of a different form of oxide on the surface, see Figure 5.39. All other samples again showed a transition to nickel oxide. The barrier based oxide was detected on the surface suggesting some openings in the nickel layer where the oxide could be observed. It was not possible to discern what the complete makeup of the anodized oxide on the surface was comprised of. The exposed oxide was found to contain aluminum oxide, trihydroxide, and oxide hydroxide as well as hydrated alumina. The one peak does not provide enough information, however, one would expect there to be some level of hydration in the barrier oxide due to exposure to an aqueous environment during modification of the sheet surface.

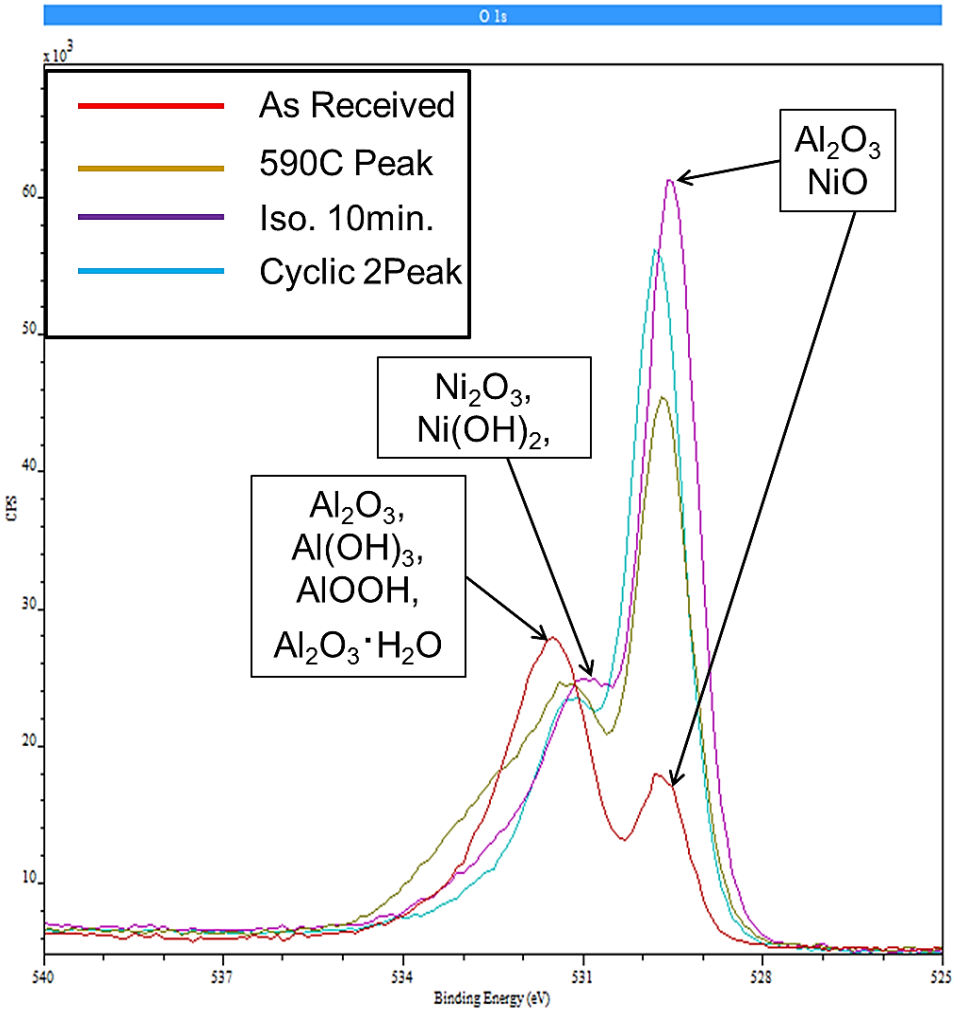

Figure 5-39 - XPS O 1s Traces for Surface Scans of All Samples (see Legend)

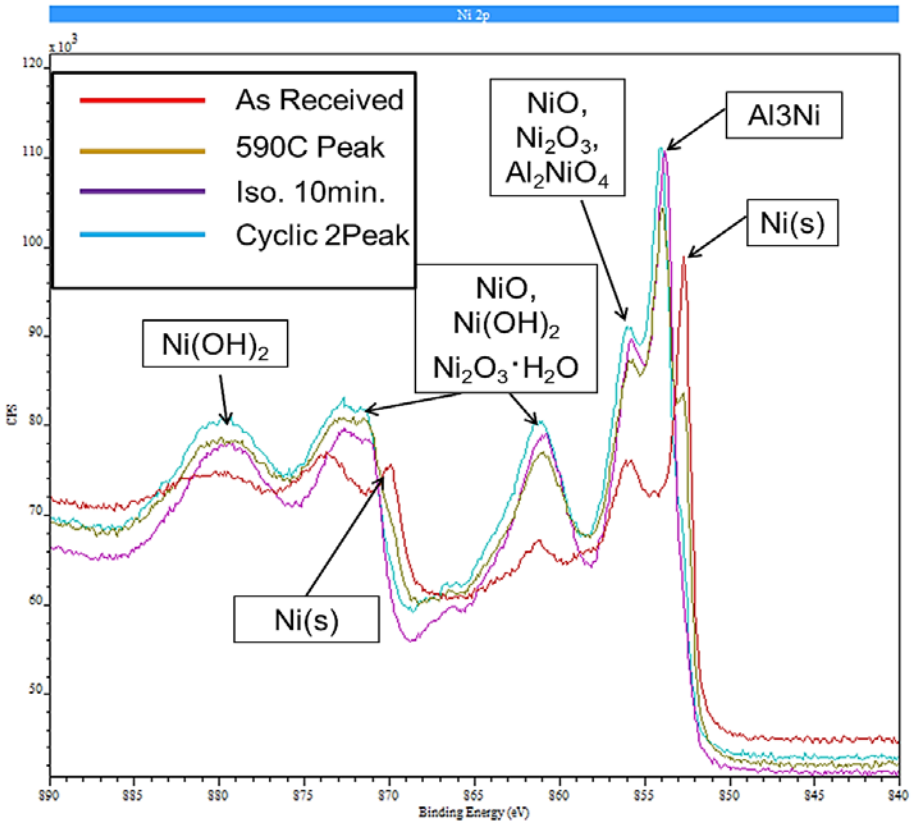

Figure 5-40 - XPS Ni 2p Traces for Surface Scans of All Samples (see Legend)

Figure 5.40 shows the Ni 2p traces for all samples during the surface scans. Of interest, is the change from the as received (AR) condition and the uniformity of that change across all other samples. In the AR samples, we see solid nickel peaking and some peaks for its oxide with no Al_3Ni peaks. In the 590˚C Peak (gold) curve we can see that not all the surface nickel has reacted and a smaller peak remains for Ni(s). The other samples show the reacted intermetallic but also show the presence of some oxides and hydroxides of nickel on the surface. The source of hydration for this oxide could be coming from either the DSC, or the underlying hydrated aluminum oxide.

Surface scans revealed no traces of silicon and showed standard peaks for solid aluminum. Following the surface scans, individual depth profiles were taken for each sample. 3 out of 4 samples were scanned at nine points during testing; these points are shown in Figure 5.42. Using the sputter rates in Figure 5.41, the breakdown of relative distances sputtered away into the sample was determined. In total, assuming predominantly aluminum was removed

from the clad layer during XPS, roughly 500nm of material was scanned and included in the depth profiles. This should situate the final point around the oxide/clad interface.

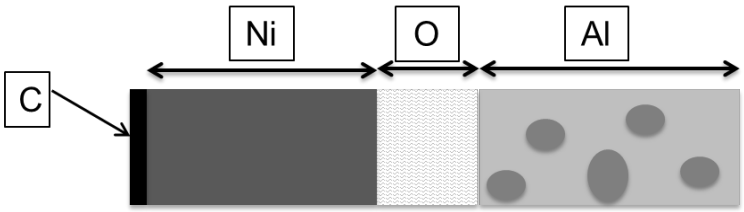

Assumed Sputter Rates (Å/min)	
Al	630
Ni	570
Al_2O_3	129
Si	310
C	40

	Time	C	Ni(250nm)	Al2O3(90nm)	Al	if all Si
Point 1	10s	4-5nm	-	-	-	-
Point 2	30s		30nm	-	-	-
Point 3	90s		90nm	-	-	-
Point 4	180s		175nm	-	-	-
Point 5	270s		260nm		-	-
Point 6	360s			280nm	-	-
Point 7	720s			360nm	-	-
Point 8	780s				420nm	390nm
Point 9	900s				550nm	450nm

Figure 5-42 - Depth Profile Sputter Rates and Distances Relative to Time and Points [77]

For the as received condition, the divide between the nickel layer and the underlying oxide was observed and used to help create 5.42. The presence of silica and silicon peaks was observed in the Si2p region which reinforced the theory that silicon was also being oxidized during nitric acid treatment. The figure shows in the Ni2p image that solid nickel is present until the last, lowest brown trace where we can see a large peak for alumina indicating the anodized oxide layer had been reached. Of interest was the presence of nickel oxide at the

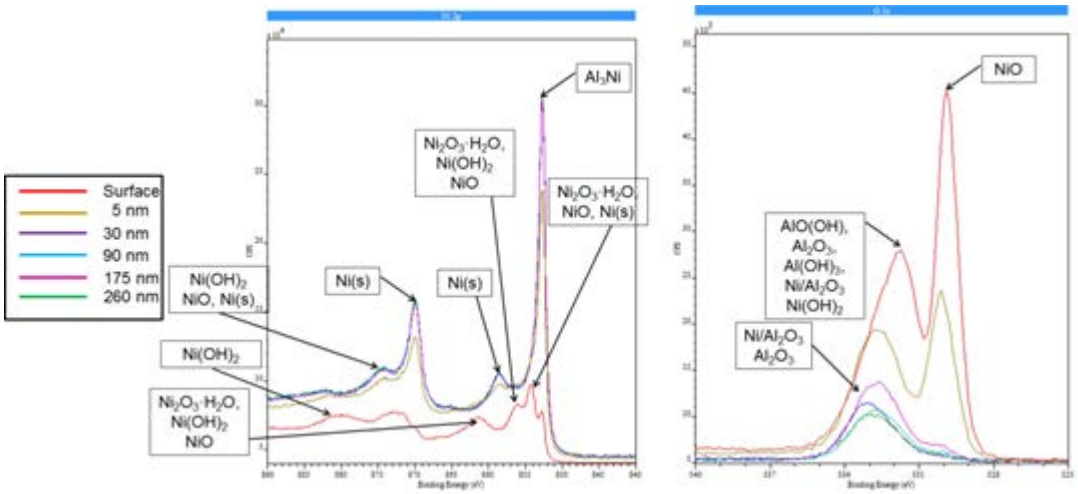

Figure 5-41 - Ni2p and O1s XPS Peaks for Isothermal 10 min. Hold at 590°C and Cooled

surface (red curve) showing that even the as sputtered nickel with no heating had grown a thin oxide layer near the surface exposed to air.

The most significant result for the sample brought to 590˚C was the discovery of solid nickel still present above the oxide, see Figure 5.43. This nickel was found a few points into nickel oxide on the surface and there was also Al_3Ni present as well. More peaks were visible in the Ni 2p region showing an increase in nickel oxide/hydroxide. Finally, some peaks

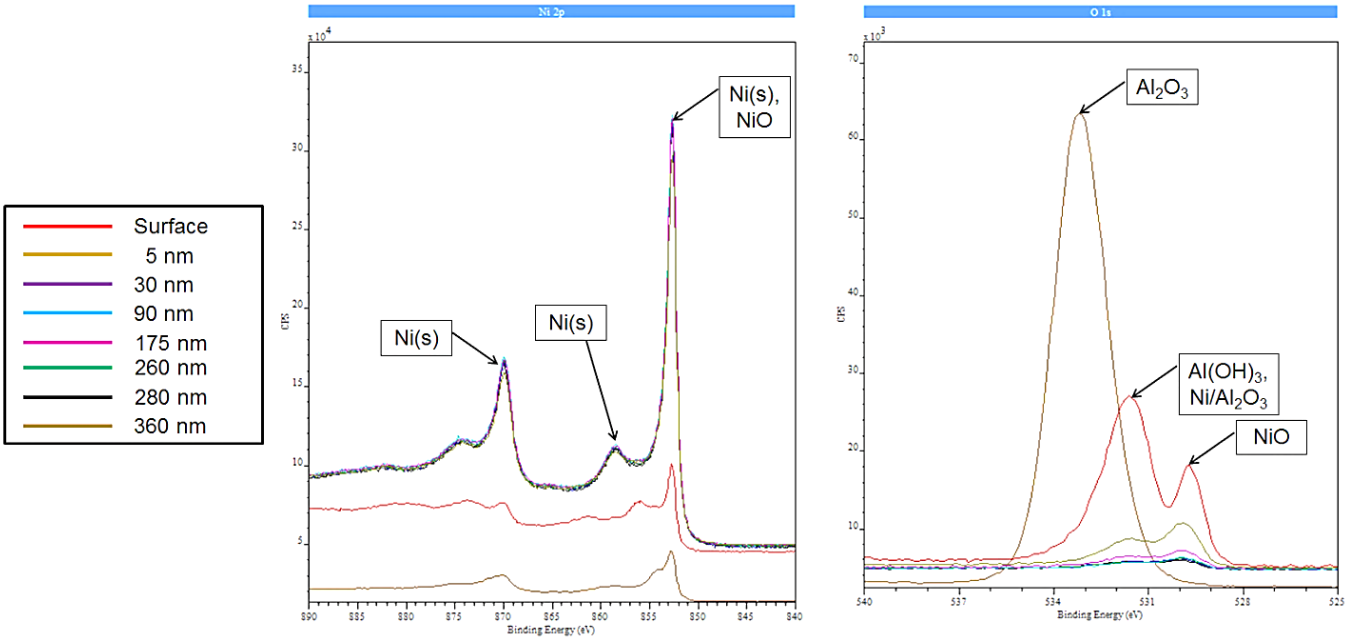

Figure 5-43 - Ni2p and O1s XPS Peaks for As Sputtered

suggested the incorporation of nickel into alumina.

Both the Isothermal 10 minute and Two Peak Cyclic samples showed similar XPS traces (Figure 5.44), suggesting that there was not much difference in the strain/fatigue applied to the oxide by melting and resolidification. The depth profile traces begin at the trace showing nickel hydroxide and proceed upwards until points 8-10 (360-550nm) which trend downwards. Nickel was still visible at the surface of both samples, both of which have more than ten minutes of liquid duration under DSC demonstrating the reluctance of the oxide to allow nickel transport. The nickel layer again incorporates a larger amount of hydration in its oxide layer. The last three traces in the O1s image show that the oxide is still present and largely uniform by the similarity in intensity peaks.

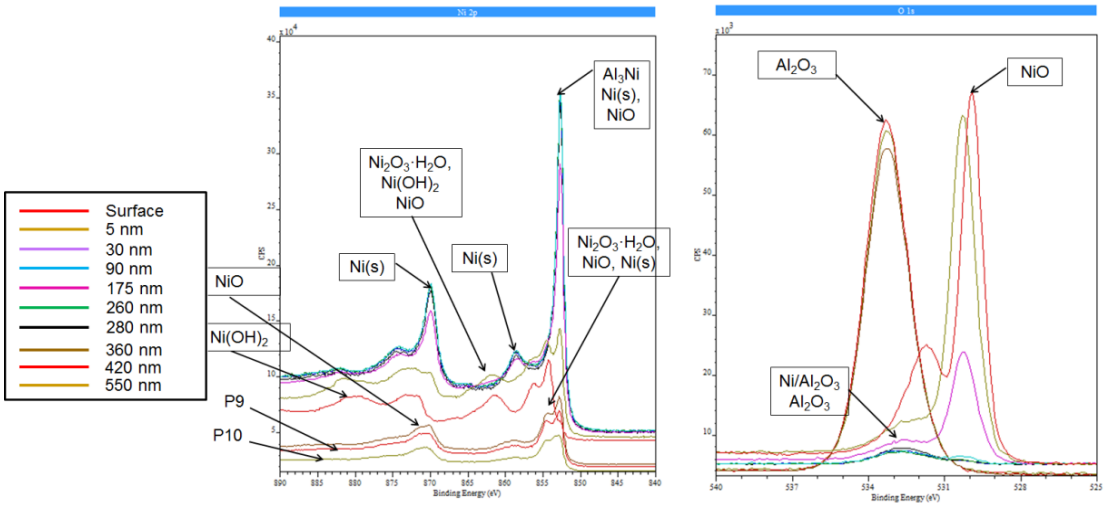

Figure 5-44 - Ni2p and O1s XPS Peaks for LSP40V Brought to 590°C and Cooled

Figure 5.45 shows the optical imaging of each DSC condition after being cooled. These samples were placed in the DSC with the XPS samples. A sample file was run and both the XPS and DSC sample were placed on the sample and reference pans. This was done so that both samples were under the same conditions for the optical study after. The 590°C

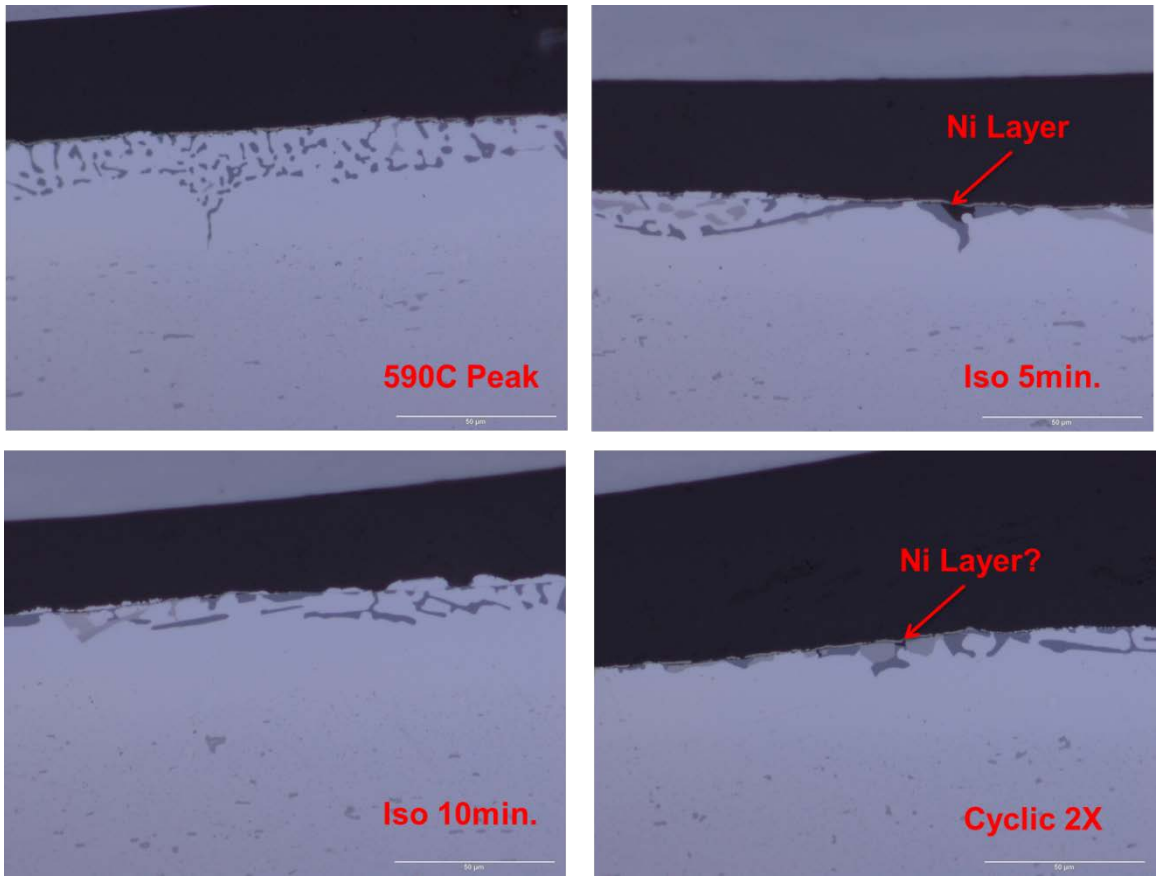

Figure 5-45 - Microstructure of LSP40V DSC Specimens Observed under XPS

Peak samples show only the Al-Si eutectic, and progressively nickel is incorporated more and more in each sample thereafter. Some remnants of the nickel layer do persist even in the cyclic two peak sample and isothermal samples, confirming the XPS results.

5.2.4 Effect of Nickel Thickness

Table 5.10 shows which measurements for the “pre-reaction” solid-state exotherm for all materials as a function of Ni plating thickness. Samples LSP 10V, LSP 40V and HSP 40V showed no measurable exotherms, regardless of the amount of Ni plating. Samples LSP 40V and HSP 40V were both anodized in a barrier type solution and had the thickest oxides. These oxides are thick enough that the aluminum nickel reaction did not occur regardless of nickel thickness, at least in terms of measurable exotherms observed in DSC analysis.

Table 5-10 - Average Aluminum Nickel “Pre-Reaction” Exotherm for all Oxide Disruption Samples

	AR (23nm)	LSP (13nm)	LSP 10V (~35nm)	HSP (5nm)	HSP 10V (~35nm)	LSP 40V (60nm)	HSP 40V (66nm)
0.1 µm	N/A	-0.21 J/g	N/A	N/A	N/A	N/A	N/A
0.25 µm	-0.34 J/g	-4.07 J/g	N/A	N/A	-0.33 J/g	N/A	N/A
0.5 µm	-0.73 J/g	-0.55 J/g	N/A	-0.14 J/g	-0.68 J/g	N/A	N/A

Aside from its influence over the magnitude of pre-reaction, Ni plating thickness also influenced the initial melting behavior of the braze sheets. A demonstration of this effect can be seen in Figure 5.46. This image shows the DSC traces for as received braze sheet that was only cleaned in acetone prior to sputtering and would only possess the native oxide after fabrication (shown to be ~26nm). The red curve heating endotherm shows a double peak and indicates that locally some Al-Ni-Si has been formed and melted but that the bulk liquid at the surface is aluminum and silicon. By adding more nickel to the surface, the entire clad region is able to mix and form the Al-Si-Ni ternary eutectic.

Figure 5.47 shows the effect of nickel thickness on liquid duration and the overall endothermic magnitude for the as received sample. Aside from a single point, the rate of

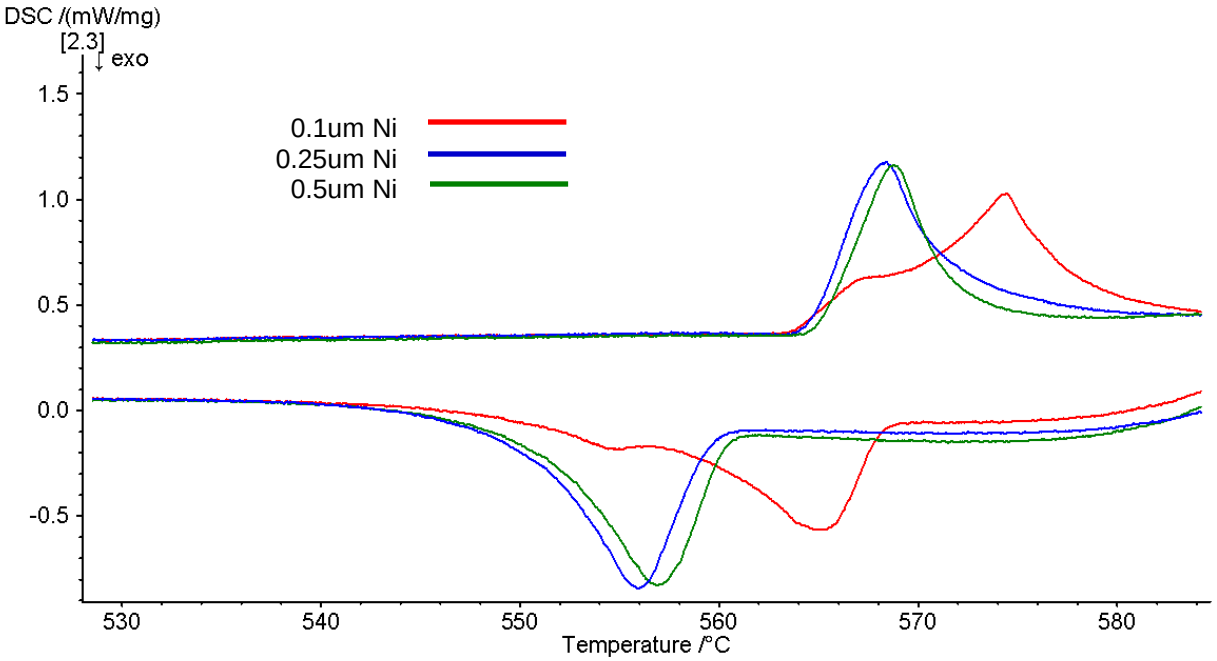

Figure 5-46 - First Heating and Cooling during Cyclic Testing of As Received Braze Sheet Sputtered with 0.1, 0.25, and 0.5um Nickel

isothermal solidification and the amount of liquid present (i.e. magnitude of the endotherm) for all nickel thicknesses were the same. Referring back to Table 5.8 and 5.10, we see that Sample AR exhibits a relatively small “pre-reaction and larger convoluted exotherm. This indicates that disruption of the oxide layer such that Ni reacts with the underlying Al-Si readily occurs, but requires clad melting to be realized. The magnitude of both “pre-reaction” and convoluted exotherms increase with an increase in Ni plating thickness, which makes sense since more available Ni as a reactant allows more intermetallic formation. However, if we consider the effect of solid state reaction, nickel transport and reaction with the solid clad surface, it is possible other surface conditions are letting nickel in even more readily, or are preventing transport resulting in no exotherm.

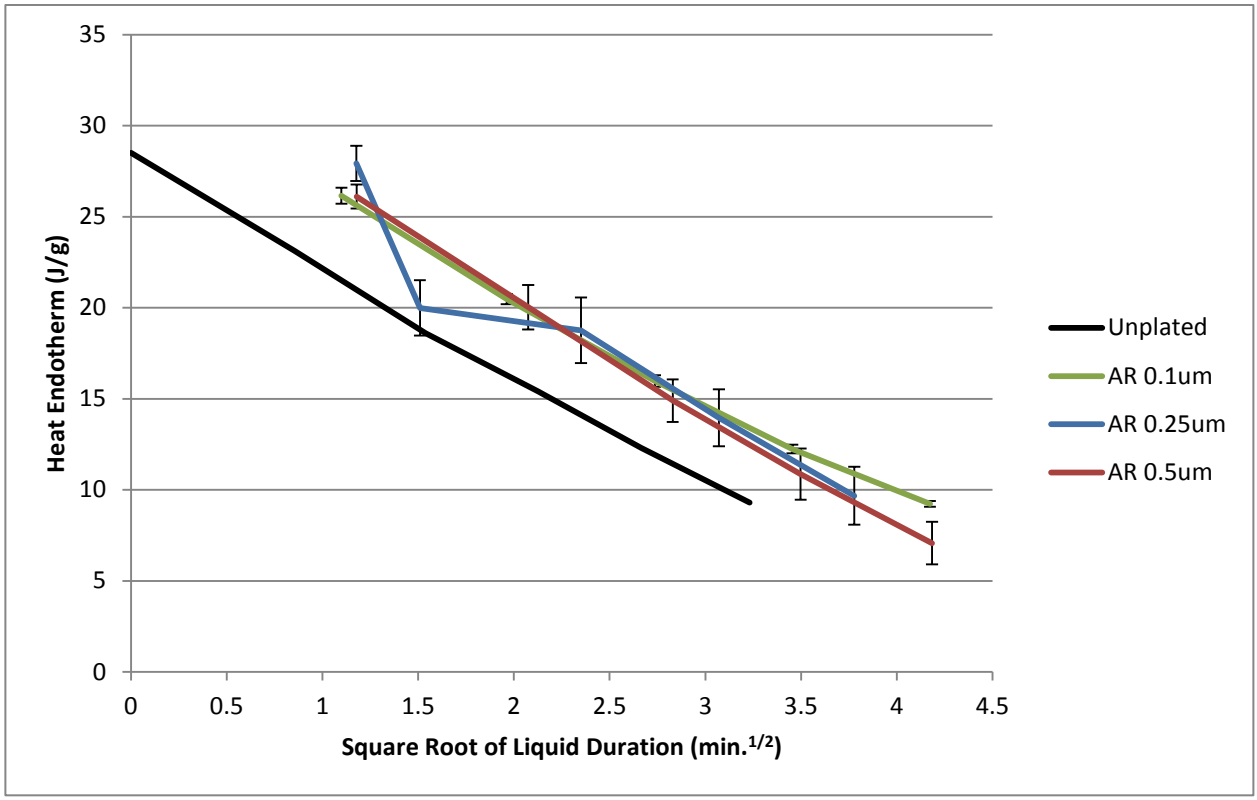

Figure 5-47 - Effect of Nickel Thickness on Sputtered As-Received Braze Sheet

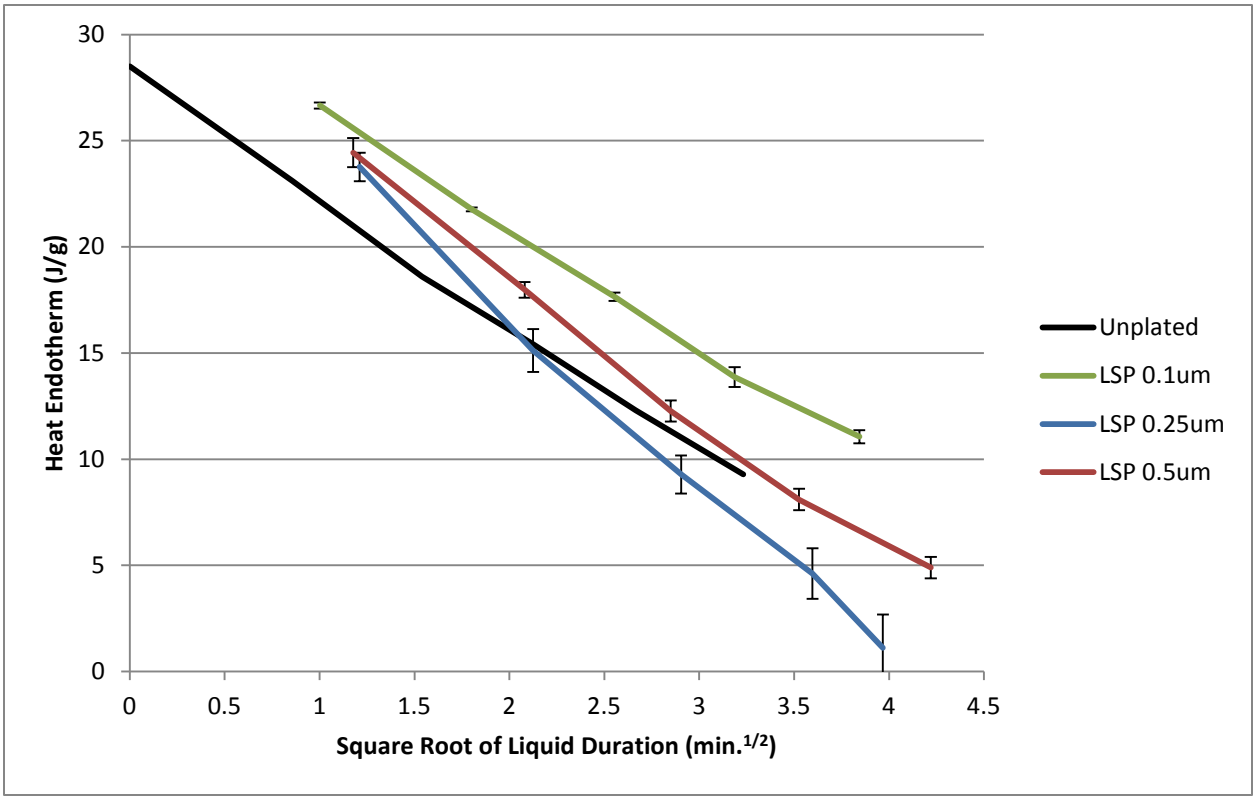

Figure 5-48 - Effect of Nickel Thickness on Sputtered Light Surface Prepared Braze Sheet

An example of this effect would be Figures 5.48 showing cyclical behavior of LSP samples with different nickel thicknesses. The addition of nickel appeared to lower overall liquid duration for samples lightly surface prepared in nitric acid.

The reason for this drop in liquid behavior was not immediately clear and was complicated further by the fact that all surface conditions and their anodized specimens behaved differently, see Figure 5.49. For LSP40V samples, the effect was the opposite and, with more nickel, longer liquid duration was possible. LSP10V samples behaved similar to LSP40V samples but this trend did not hold for all anodized samples. HSP10V and HSP40V samples did not behave in any discernable pattern. Due to this convolution of different surface conditions and oxide thicknesses behaving differently, it was decided that no true pattern emerged from contrasting different cyclical tests of varied nickel thicknesses. The major effect of added nickel thickness seemed to be solely involved in allowing nickel to remain present at braze temperature and not to fully oxidize on the surface.

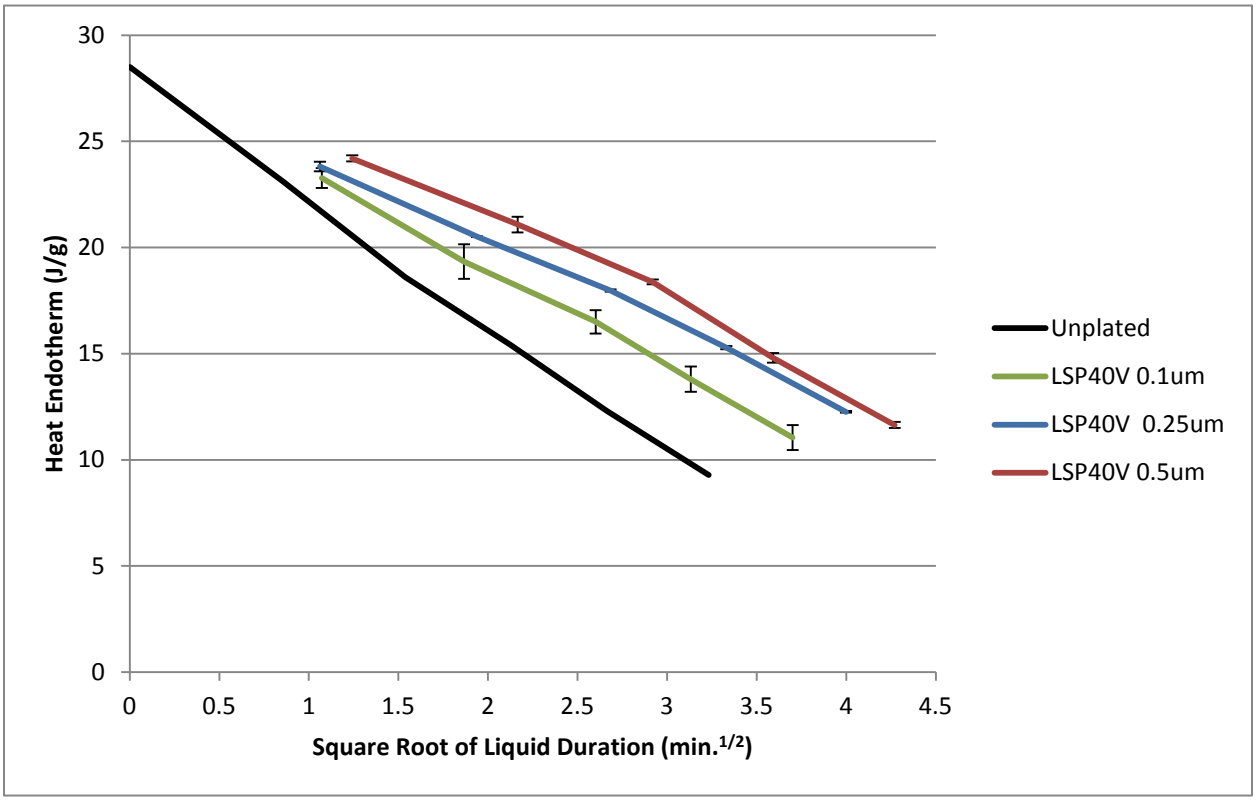

Figure 5-49 - Effect of Nickel Thickness on Sputtered Light Surface Prepared Braze Sheet

5.2.5 Effect of Surface Silicon

The trending of all surface conditions was best observed in the 0.5µm case, where it seemed that enough nickel was available so that clear distinctions could be made. Figure 5.50 shows the effect of surface preparation. Again, the argument of some surface silicon being lost during chemical treatment would help explain why LSP lies below the AR case. HSP had both the sodium hydroxide effect as well as nitric and/or hydrofluoric acid which removed the remainder of the surface silicon. As a result, HSP samples had the lowest endothermic values due to the removal of silicon prior to melting. The ability of surface conditions and varied levels of clad surface silicon to affect the overall rate of silicon diffusion (slopes of the lines) was something that had not been studied before.

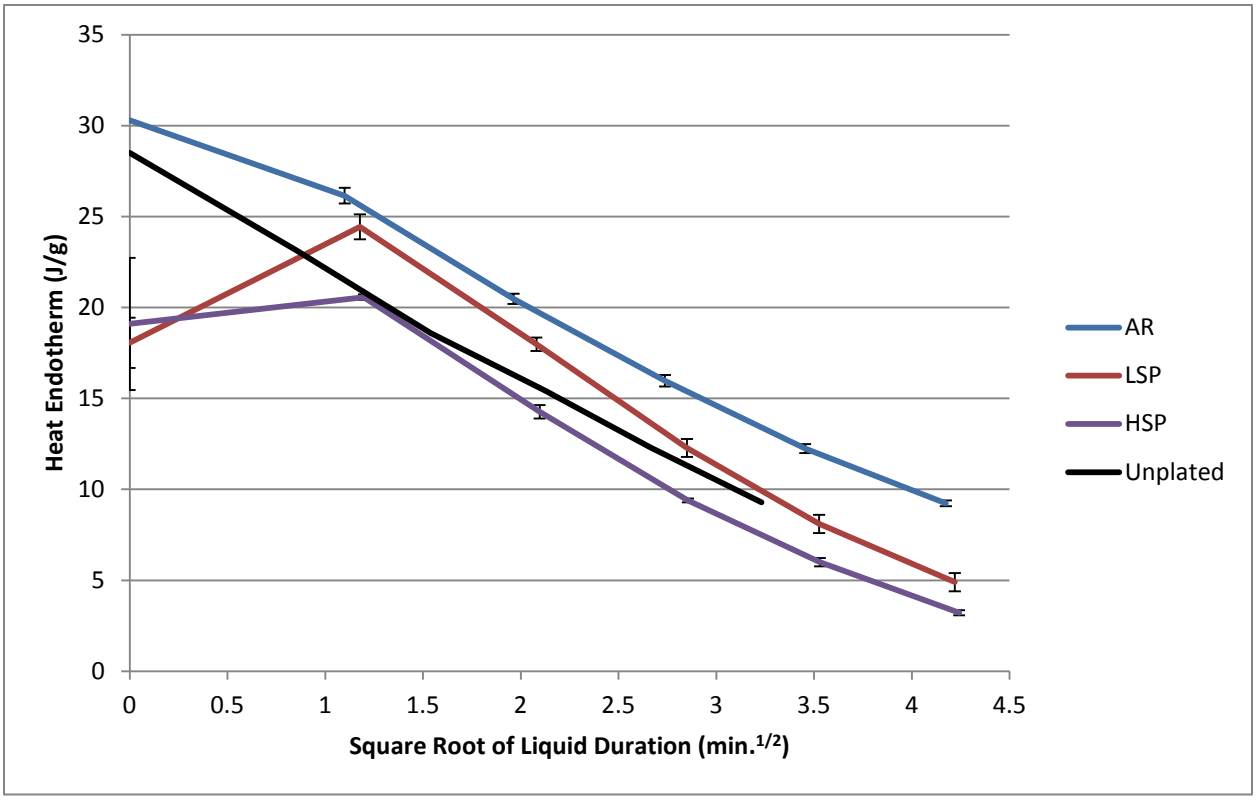

Figure 5-50 - Cyclical Liquid Behaviour across Surface Conditions with 0.5um Sputtered Nickel

These can also be seen in DSC traces of initial heating to 590˚C and subsequent cooling. Figure 5.51 shows the DSC traces of samples AR, LSP, and HSP on the first cycle in a cyclical run. The shifting of all heat endotherms to 565˚C was a clear indicator that the formation of a ternary Al-Si-Ni eutectic mixture had occurred. Samples LSP and HSP showed larger exotherms and convoluted/reduced the initial heat endotherm as well. The

same trends of available liquid shown in Figure 5.51 were observable in the freezing exotherms. The as received samples possessed more available liquid Al-Si then both LSP and HSP, with HSP showing the lowest peak area. All observed exotherms on the DSC traces were minimal but recall that calculated true exotherms have higher values.

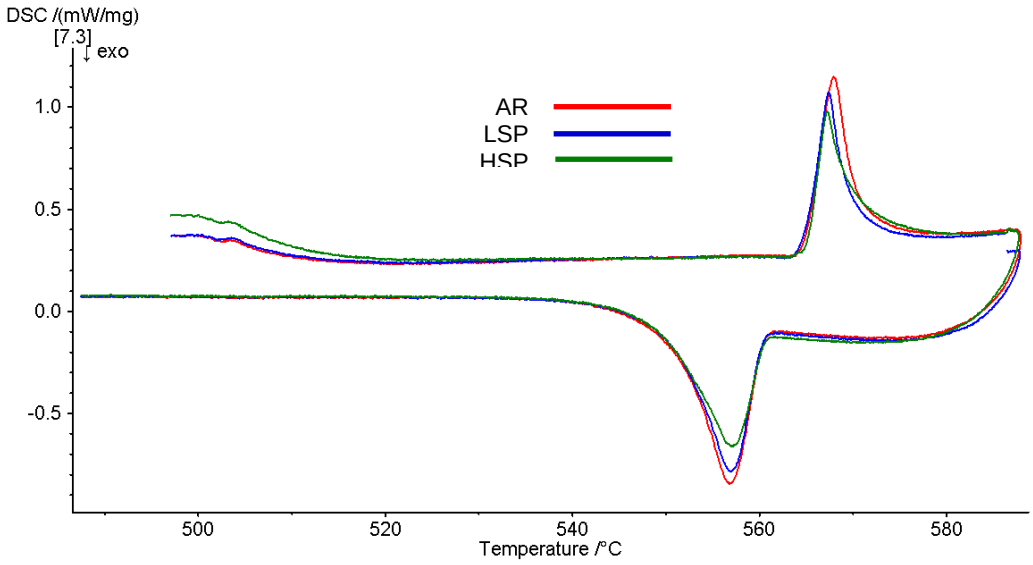

Figure 5-51 - DSC Traces of Initial Heating to 590°C and Cooling for Samples AR, LSP, and HSP Sputtered with 0.5um Nickel

Table 5.11 is a small excerpt of table 5.9, showing all calculated true exotherms for samples AR, LSP, and HSP. The trends for the 0.5um nickel thickness were the most discernible and possible to interpret. LSP samples had the second lowest oxide thickness (~13um) compared to HSP samples which showed thicknesses of 5um. LSP had no augmentation to its surface silicon and interacted the most for the 0.5um nickel case. HSP was not able to react to the same extent despite its thinner barrier to reaction. No explanation was able to attribute for LSP samples poor performance at lower nickel thicknesses where trends between AR and HSP were still quite clear.

Table 5-11 - Calculated True Enthalpy of Aluminum Convoluted Nickel Reaction Exotherms for Surface Varied Samples

	AR	LSP	HSP
0.5 um	-11.86	-13.8	-7.59
0.25 um	-9.38	-1.29	-7.22
0.1 um	-1.36	0	-0.52

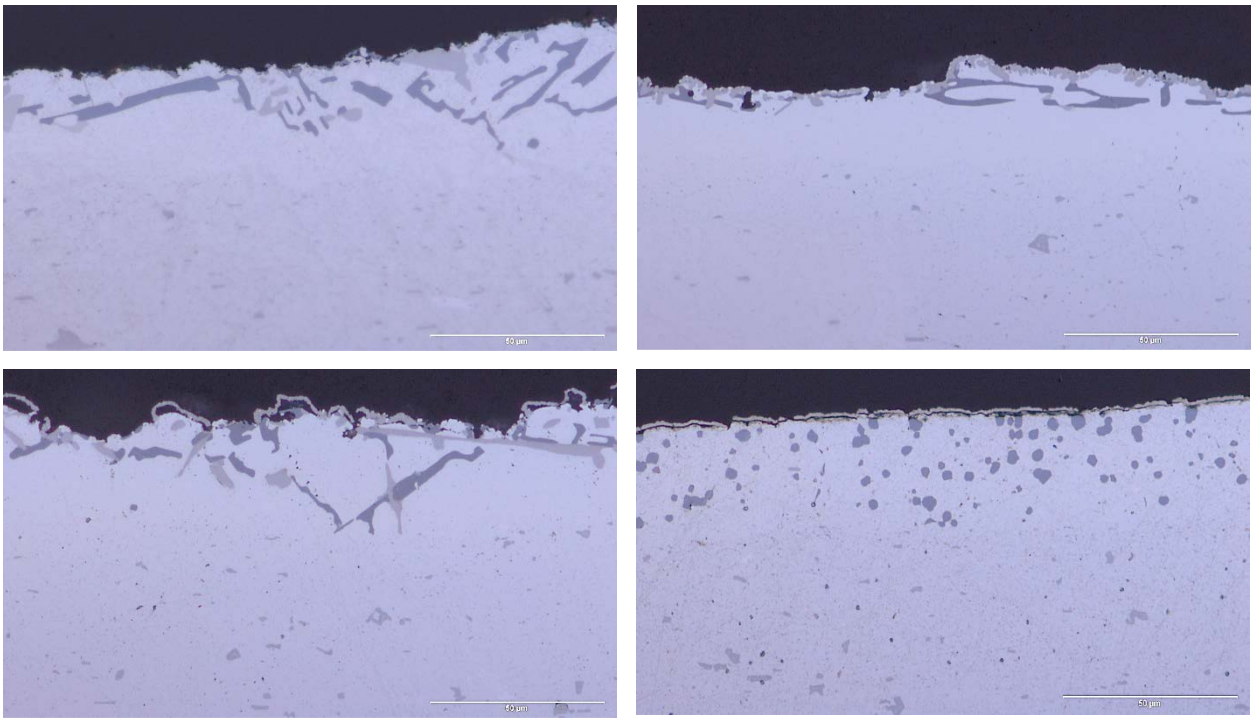

Figure 5-52 - Microstructure of Samples AR (23nm), HSP (5nm), HSP10V (~35nm), LSP40V (60nm) 0.5um Ni heated to 570°C and cooled under Optical Microscopy 50X (Scale Bar 50um)

Microstructure of the samples heated past the ternary reaction at 565˚C varied depending on surface preparation. Figure 5.52 shows the various reaction surfaces that were observed in samples AR, HSP, HSP 10V, and LSP 40V heated up to 570˚C and cooled. Samples AR and LSP shared a similar reaction microstructure to that of the Dana samples, indicating a fully liquated surface with the development of a well-defined ternary eutectic microstructure. Samples HSP and HSP 10V demonstrated a reluctance to fully integrate all nickel, with most of the nickel on sample HSP remaining near the surface. Sample HSP 10V showed a sort of fraying of the nickel layer suggesting certain local areas may have failed first. This relates back to the argument of alternative modes of fracture within the oxide. Sample LSP 40V maintained it's as received microstructure more than any other sample. Here the clad surface has not yet melted at 570˚C demonstrating only aluminum and silicon are present below the surface oxide.

Sample HSP 40V when heated behaved like sample LSP 40V up until melting of the clad layer at 577˚C. Following melting all the surface nickel was able to penetrate and coat the surface eutectic, see Figure 5.53. This microstructure was typical of halted tests where a large portion of nickel had been introduced but not allowed enough time or temperature to

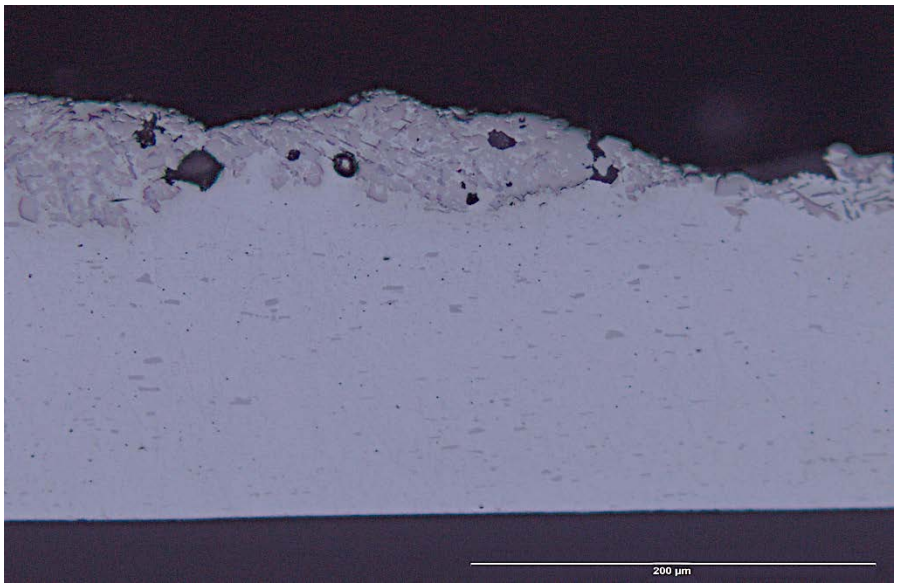

Figure 5-53 - Microstructure of Samples HSP40V (66nm) 0.5um Ni heated to 581°C and cooled under Optical Microscopy 50X (Scale Bar 50um)

mix well [67]. This resulted in large solidified portions of nickel aluminide phases in the ternary eutectic mixture. The nickel aluminide did not abrade away as quickly as the aluminum matrix during grinding.

The images of Figure 5.52 and 5.53 are consistent with the variation in onset temperatures presented in Fig. 5.37, Sample LSP 40V was the only sample that maintained a high onset temperature beyond the first cycle of heating. This indicated the oxide layer on this sample prevented Ni interaction with the underlying braze layer. This is supported by Figure 5-52d. The conclusions from the peak tests was that surface preparation had a minor effect on the outcome of the aluminum nickel reaction only in that lower silicon content lead to less Al-Ni-Si eutectic being present, see sample HSP in Figure 5.52. The lack of silicon near the surface also meant that the nickel formed Al_3Ni at the near surface but could not form the Al-Ni-Si eutectic. As received and light nitric acid treatment yielded similar microstructures and were identical to previous Dana samples (A, B, and C), see Figure 5.8b.

5.2.6 Oxide Disruption Conclusions

In an effort to better understand the method of oxide disruption, pure nickel was sputtered onto seven varied braze sheet surfaces. The surface conditions arose from the need to anodize oxides to different thicknesses, as well as gain a better understanding of nickel transport and the necessity of clad silicon. An effort was made to ensure the oxide would be continuous, amorphous, and otherwise provided an analogue to the native as received surface oxide. The heavy surface preparation proved to have a thin oxide with no exposed surface silicon to interact with the nickel layer. The light surface preparation possessed half the oxide thickness of typical braze sheet and was found to have interacted with surface nickel and showed the exotherm for the aluminum nickel reaction. Heavy surface preparation had the thinnest oxide but, due to removal of surface silicon, the ternary reaction at the surface was impeded.

The clearest result of the work is that the presence of oxide on the surface of the clad layer is a major deterrent to the formation of the Al_3Ni phase. The oxide seems to pose as a direct barrier to this interaction, by which ample time is given for a very thin nickel layer to oxidize whereas thicker nickel layers do not react until they come in contact with molten clad. It would seem that in the time necessary for nickel to diffuse, either most/all of the reaction has occurred or none has circumvented through the oxide layer. It would seem fair to postulate most of this reaction occurs either through the cracking, or inherent cracks present before thermal analysis, of the oxide layer.

The role of nickel thickness was to allow enough time for the above mentioned events to occur and allow aluminum and nickel to be in contact. Thin nickel layers were quickly consumed in solid state, oxidation, or hydration reactions. Thicker nickel layers were more likely to show exotherms, indicating the aluminum nickel reaction. Nickel appeared to have some role in the hindrance of silicon diffusion from the clad layer. This was apparent in the varied liquid behavior of all surface conditions, especially with increased nickel thickness. The ternary reaction, (Al) + (Si) + (Al_3Ni), retains some silicon necessary for the eutectic constituents to form and remain in the clad layer which may account for lower/higher liquid durations.

In terms of observing the aluminum nickel reaction, samples which received light surface preparation showed the strongest exotherms. This sample had the thinnest oxide while still possessing silicon near the surface available for the ternary reaction. Both surface conditions (LSP and HSP) could not be directly compared due to the effect of hydrofluoric acid on surface silicon, however, both conditions provided insight into the nature of the aluminum nickel reaction. Of interest were the varied methods of fracture which were noted in the halted microstructures at 570˚C. The possibility of samples anodized to ten volts exhibiting delamination of the oxide layer, as opposed to a direct fracture and removal inherent of thicker oxide layers, would be an interesting area to continue study.

In terms of the behavior of the liquid clad melt, the effect of nickel interacting with the clad was most clear in sample LSP40V where a direct shift in the rate of isothermal solidification could be observed. Once nickel was introduced, the rate of silicon removal increased on par with samples where nickel entered the molten clad on the first melt peak. In terms of surface conditions, it was found that when enough nickel was present (0.25, 0.5 µm) as received samples possessed the longest liquid duration followed by LSP and then HSP. An alternative oxide fracture mechanism, or delamination in some cases, may explain why samples LSP10V and HSP10V behaved so poorly. An easier avenue for nickel to penetrate may have immobilized some surface silicon for the ternary eutectic.

A critical oxide thickness seems to exist, around 40-66 nm in thickness, where there is a delay in the aluminum nickel reaction due to indirect contact. This is exemplified by sample LSP40V. Sample LSP40V halts the ability for nickel to pass directly to the molten clad, prevents mixture, and supports the idea that nickel must transport through fracture, or molten clad flow upwards, and not by solid state diffusion. XPS studies showed that a large portion of the surface nickel is being oxidized by the ambient DSC environment, and possibly hydrated by the neighboring oxide layer. It was also shown that cyclical testing, when compared to isothermal holds, in no way has an effect of applying fatigue to the oxide layer. It would be interesting to study the anodized ten volt samples to see if fatigue might apply for a thinner oxide.

To summarize, when studying the effect of barrier type oxide layers and their interaction with surface nickel it was found that a critical oxide minimum and maximum exist. At a critical maximum, nickel is delayed from direct introduction to the molten clad layer and experiences further oxidation and hydration. At the minimum, a transitional change of the method of fracture occurs and oxides below this minimum may preferentially delaminate. The presence of any oxide layer has a negative effect on the aluminum nickel reaction, and lack of local silicon inhibits this reaction even further.

6.0 Conclusions

As previously discussed in Chapter 5.0, a primary purpose of the present work was to examine two distinct aspects of Dana Canada's patented fluxless nickel process; i) the influence of varying process parameters on the melting and solidification kinetics of Al braze sheets in Dana's proprietary fluxless nickel brazing process, and ii) the oxide disruption mechanism. This was accomplished through the use of Differential Scanning Calorimetry (DSC) as a thermal investigative technique, as well as other forms of spectroscopic and characterization methods.

From previous work, and also seen in this present body of work, it was known that the nickel aluminide (Al_3Ni) was a one-time reaction occurring at, or near, the temperature for the ternary eutectic reaction of the Al-Ni-Si system. The reaction results in a large exothermic burst visible in the DSC just prior to the melting of the clad layer and the resultant crystal structure is four times the volume of that for nickel or aluminum FCC structures. This leads to a mechanical disruption of the surface oxide layer and potentially allows exudation of the molten clad layer on to the exterior oxide surface. This leads to wetting and the ability to successfully braze adjacent braze sheets in a brazing process.

Examining Dana's process varied samples showed that the height and fraction area coverage of electrolytically deposited nickel was quite uniform and there was little to no effect on the overall nickel reaction. Reactions on samples A, B, and C all occurred at, or near, 565˚C (the ternary eutectic reaction) and resulted in similar microstructures. These microstructures consisted of a roughened surface and formation of nickel aluminide dispersed in the aluminum silicon eutectic.

In order to better understand the conditions for oxide disruption in the fluxless braze sheets, a set of experiments were conducted to observe the role of varied surface oxide layers. This was achieved by varying oxide thickness with anodization and altering the amount of surface silicon through chemical processes. Samples were sputtered such that each coupon for testing received a thin, uniform layer of nickel with heights, or thicknesses, measured to be roughly 0.1, 0.25, and 0.5 microns.

In terms of oxide thickness, the results showed that an oxide layer of any thickness present on the surface is disadvantageous to the nickel aluminide reaction occuring. This was evident in samples which had received a light surface treatment in nitric acid which was confirmed in TEM measurements to have an oxide layer half the thickness of the native braze sheet. The nickel reactions observed under DSC showed very shallow exotherms. Using cyclical data to de-convolute the results showed that in fact larger reactions were occurring but in many cases at a much slower rate. Thicker oxide layers were able to inhibit the nickel aluminum reaction from ever occurring even at temperatures well above the ternary eutectic (600°C)

Microstructures confirm localized sites where nickel was slowly being introduced into the molten aluminum silicon clad layer. This was believed to be through small cracks, or defects, in the oxide surface which were either present upon manufacture, or were created through stresses from the molten layer lying underneath. XPS measurements showed that the nickel layer would remain mostly intact for samples with a thick anodized layer. Only when the clad layer had sufficient time in the liquid phase would the complete formation of Al_3Ni occur. This was independent of a continued isothermal hold or a cyclical hold which did not seem to show much difference in resultant phases and did not display any fatigue like behavior in the oxide layer.

Very thin nickel layers were found to be susceptible to oxidation and hydration when it was heated but unable to react with the aluminum in a timely manner in the DSC thereby suppressing the exothermic thermal signature associated with this reaction. Due to this effect, samples with low levels of nickel (i.e. 0.1 µm sputtered thickness) would show little to no exothermic values prior to the melting of the clad layer. The advantage of a thicker nickel layer was that it provided an adequate reservoir of nickel close to the nickel/oxide interface which could eventually be introduced into the molten clad layer.

It was found that a critical oxide thickness exists where no nickel can pass the thick barrier of the oxide, at least not in the allotted time of a braze cycle. At the same time, a minimum oxide thickness may exist where the mechanism of oxide fracture changes between fracture and removal to delamination which may allow nickel to enter the molten clad more easily.

The presence of any oxide layer has a negative effect on the aluminum nickel reaction, and lack of local silicon inhibits this reaction even further by preventing the formation of the lower melting aluminum nickel silicon ternary.

6.1 Scope for Future Work

Further work into the effect of nickel on the rate of silicon removal would an interesting continuation in terms of cyclical DSC testing. Shifts in the slopes of cyclical testing curves could not be completely explained during testing in both process variation and oxide disruption. It was suggested that the calculation of Al-Si pseudo binary diagrams with increasing levels of nickel may help in such an investigation.

An investigation into these critical oxide thicknesses may yield benefits to the overall braze process. This would help isolate the exact method of oxide disruption whether it is through fracture, or delamination. Whether the native oxide behaves in the same manner as an anodized layer might be an area to investigate as well. A better understanding of this fracture perhaps provide a method by which the oxide could be manipulated.

Finally, the exact method by which nickel passes the oxide layer would be useful as this bypassing allows the aluminum nickel reaction to take place. Throughout this work it was suggested that this was through cracks in the oxide but was never visually confirmed. Again this could be used to improve the overall process efficiency and use of nickel, and yield a better braze if the oxide could be disrupted or circumvented in a more efficient manner.

References

1. Miller, W. S., et al. "Recent Development in Aluminum Alloys for the Automotive Industry." Materials Science and Engineering: A 280.1 (2000): 37-49.
2. ASM Specialty Handbook, “Aluminum and Aluminum Alloys”, Materials Information Society (1996)
3. J. Lacaze, S. Tierce, M.C. Lafont, Y. Thebault, N. Pebere, G. Mankowski, C. Blanc, H. Robidou, D. Vaumousse and D. Daloz, “Study of the Microstructure Resulting From Brazed Aluminium Materials Used In Heat Exchangers”, Mat. Sci. and Eng. A413-414 (2005), 317-321.
4. Dockus, KF, “Fluxless Bonding Method for Aluminium Components, Welding Journal, Vol. 57, 10, 36-42.
5. B.E. Cheadle and K.F. Dockus, International Congress and Exposition , Detroit, Michigan, Feb. 29-Mar. 4, 1988; SAE Technical Paper Series-Inert Atmosphere Fluxless Brazing of Aluminum Heat Exchangers.
6. D.P. Sekulic, “Molten Aluminum Equilibrium Membrane Formed during Controlled Atmosphere Brazing, Int. J. Eng. Sci., 39, (2001), 229-241.
7. Barlow, C. Y., N. Hansen, and Y. L. Liu. "Fine Scale Structures from Deformation of Aluminium Containing Small Alumina Particles." Acta materialia 50.1 (2002): 171-182.
8. Le, H. R., et al. "Surface Oxide Fracture in Cold Aluminium Rolling." Acta Materialia 52.4 (2004): 911-920.
9. Hawksworth, Doug, and Alan Gray. The Influence of Silicon Particle Morphology on the Melting Mechanism of Aluminium Brazing Sheet. No. 2005-01-2043. SAE Technical Paper, 2005.
10. Yoon, J. S., S. H. Lee, and M. S. Kim. "Fabrication and Brazeability of a Three-Layer 4343/3003/4343 Aluminum Clad Sheet by Rolling." Journal of Materials Processing Technology 111.1 (2001): 85-89.
11. Nowicke Jr, Frank, Antonios Zavaliangos, and Harry C. Rogers. "The Effect of Roll and Clad Sheet Geometry on the Necking Instability during Rolling of Clad Sheet Metals." International Journal of Mechanical Sciences 48.8 (2006): 868-877.
12. Dockus, Kostas F. "Method of Brazing Aluminum Parts." U.S. Patent No. 3,970,237. 20 Jul. 1976.

13. Shah, Ramesh K. "Advances in Science and Technology of Compact Heat Exchangers." Heat Transfer Engineering 27.5 (2006): 3-22.
14. D. Sekulic, “Advances in Brazing: Science, Technology and Applications”, Woodhead Publishing (2013)
15. ASM Specialty Handbook, “Brazing”, Materials Information Society (2003)
16. Winkler, S., Dana Canada Corporation, Personal Communication, 2014.
17. Turriff, D. M., S. F. Corbin, and M. Kozdras. "Diffusional Solidification Phenomena in Clad Aluminum Automotive Braze Sheet." Acta Materialia 58.4 (2010): 1332-1341
18. G. Humpston, David M. Jacobson, “Principles of Soldering and Brazing”, ASM International (1993)
19. Sekulic, Dusan P. "Scaling of Molten Metal Brazing Phenomena: Prolegomena for Model Formulation." Progress in Scale Modeling. Springer Netherlands, 2008. 391-402.
20. G.J. Marshall, R.K. Bolingbroke and A. Gray, “Microstructural control in an aluminum core alloy for brazing sheet applications”, Met. Trans. A, 24A, (1993), 1935-1942.
21. Creber, D., Ball, J., and Field, D., "A Mechanistic Study of Aluminum Vacuum Brazing," SAE Technical Paper 870185, 1987
22. D. Apelian, “Aluminum Cast Alloys: Enabling Tools for Improved Performance”, North American Die Casting Association (2009)
23. Narayanan, L. Anantha, F. H. Samuel, and J. E. Gruzleski. "Dissolution of Iron Intermetallics in Al-Si Alloys through Nonequilibrium Heat Treatment." Metallurgical and Materials Transactions A 26.8 (1995): 2161-2174.
24. Zhao, Hui, and Dusan P. Sekulic. "Diffusion-controlled Melting and Re-Solidification of Metal Micro Layers on a Reactive Substrate." Heat and Mass Transfer 42.6 (2006): 464-469.
25. M. Dehmas, R. Valdes, M-C Lafont, J. Lacaze and B. Viguier, “Identification of Intermetallic Precipitates Formed during Re-Solidification of Brazed Aluminium Alloys”, Scripta Met., 55, (2006), 191-194.
26. D.P. Sekulic, P.K. Galenko, M.D. Krivilyov, L. Walker, F. Gao, “Dendritic Growth in Al-Si Alloys during Brazing. Part I: Experimental Evidence and Kinetics”, Int. J. of Heat and Mass Transfer, 48, (2005), 2372-2384.

27. D.P. Sekulic, P.K. Galenko, M.D. Krivilyov, L. Walker, F. Gao, “Dendritic Growth in Al-Si Alloys during Brazing. Part 2: Computational Modelling”, Int. J. of Heat and Mass Transfer, 48, (2005), 2385-2396.
28. ASM Specialty Handbook, “Alloy Phase Diagrams”, ASM International (2003)
29. Norouzi Afshar, F., et al. "The Effect of Brazing Process on Microstructure Evolution And Corrosion Performance of a Modified AA4XXX/AA3XXX Brazing Sheet." Corrosion Science 58 (2012): 242-250.
30. Turriff, D. M., S. F. Corbin, and M. Kozdras. "Diffusional Solidification Phenomena in Clad Aluminum Automotive Braze Sheet." Acta Materialia 58.4 (2010): 1332-1341.
31. D. Wilkinson, “Mass Transport in Solids and Fluids”, Cambridge University Press (2000)
32. Gao, Feng, et al. "Solid State Si Diffusion and Joint Formation Involving Aluminum Brazing Sheet." Materials Science and Engineering: A 337.1 (2002): 228-235.
33. Tierce, S., et al. "Solidification and Phase Transformations in Brazed Aluminium Alloys Used in Automotive Heat Exchangers." International Journal of Cast Metals Research 18.6 (2005): 370-376.
34. Schäuble, “Silica Passivation Layer on Aluminium Brazing Sheets”, University of Köln (2010)
35. Dockus, Kostas F. "Method of Brazing Aluminum Parts." U.S. Patent No. 3,970,237. 20 Jul. 1976.
36. Corbin, Stephen Francis, et al. "In Situ Measurement of the Thermal Contact Resistance of an Al Lap Joint during Braze Processing." Metallurgical and Materials Transactions A 45.2 (2014): 835-842.
37. Chrifi-Alaoui, F. Z., et al. "Enthalpies of Formation of the Al–Ni Intermetallic Compounds." Journal of Alloys and Compounds 364.1 (2004): 121-126.
38. Richter, Klaus W., Karthik Chandrasekaran, and Herbert Ipser. "The Al–Ni–Si Phase Diagram. Part II: Phase Equilibria between 33.3 and 66.7 at% Ni." Intermetallics 12.5 (2004): 545-554.
39. Yilbas, B. S., et al. "Laser Control Melting of Alumina Surfaces and Thermal Stress Analysis." Optics & Laser Technology 43.4 (2011): 858-865.
40. Alcala, G., et al. "Mechanical Properties of Amorphous Anodic Alumina and Tantala Films Using Nanoindentation." Nanotechnology 13.4 (2002): 451.

41. Cubiotti, G., et al. "The Electronic Structure of Al_3Ni." Journal of Physics: Condensed Matter 7.25 (1995): 4865.
42. Qiu, X., and J. Wang. "Experimental Evidence of Two-Stage Formation of Al_3Ni in Reactive Ni/Al Multilayer Foils." Scripta Materialia 56.12 (2007): 1055-1058.
43. Kyriakopolous, A., M. Lynn, and R. Ghomashchi. "Reactive Interaction of Molten Aluminum and Solid Nickel." Journal of Materials Science Letters 20.18 (2001): 1699-1701.
44. Morsi, K. "Review: Reaction Synthesis Processing of Ni–Al Intermetallic Materials." Materials Science and Engineering: A 299.1 (2001): 1-15.
45. D. Jones, Principles and Prevention of Corrosion, 2nd Edition, Prentice Hall (1996)
46. J. Davis, Corrosion of Aluminum and Aluminum Alloys, ASM International (1999)
47. Zähr, J., et al. "Characterization of Oxide and Hydroxide Layers on Technical Aluminum Materials Using XPS." Vacuum 86.9 (2012): 1216-1219.
48. Shirai, Takashi, et al. "Structural Properties and Surface Characteristics on Aluminum Oxide Powders." Ceramics Research Lab 9 (2009): 23-31.
49. Levin, Igor, and David Brandon. "Metastable Alumina Polymorphs: Crystal Structures and Transition Sequences." Journal of the American Ceramic Society 81.8 (1998): 1995-2012.
50. Hunter, M. S., and P. Fowle. "Natural and Thermally Formed Oxide Films on Aluminum." Journal of the Electrochemical Society 103.9 (1956): 482-485.
51. Diggle, J. Wn, Thomas C. Downie, and C. W. Goulding. "Anodic Oxide Films on Aluminum." Chemical Reviews 69.3 (1969): 365-405.
52. Iwata, Takashi, et al. "Fabrication of Al_2O_3/Al Structure by Nitric Acid Oxidation at Room Temperature." Central European Journal of Physics 8.6 (2010): 1015-1020.
53. Beck, A. F., et al. "The Kinetics of the Oxidation of Al in Oxygen at High Temperature." Corrosion science 7.1 (1967): 1-22.
54. Shimizu, K., et al. "On the Nature of “Easy Paths” For the Diffusion of Oxygen in Thermal Oxide Films on Aluminum." Oxidation of Metals 35.5-6 (1991): 427-439.
55. Keller, F., M. S. Hunter, and D. L. Robinson. "Structural Features of Oxide Coatings on Aluminum." Journal of the Electrochemical Society 100.9 (1953): 411-419.
56. Eftekhari, A, “Nanostructured Materials in Electrochemistry”, 2008

57. R. W. Franklin, Conference on Anodizing Aluminium, Nottingham, 1961, Aluminium Development Association
58. Li, Yi, et al. "Formation and Breakdown of Anodic Oxide Films on Aluminum in Boric Acid/Borate Solutions." Journal of the Electrochemical Society 144.3 (1997): 866-876.
59. O'Sullivan, J. P., and G. C. Wood. "The Morphology and Mechanism of Formation of Porous Anodic Films on Aluminium." Proceedings of the Royal Society of London. A. Mathematical and Physical Sciences 317.1531 (1970): 511-543.
60. Mastai, Y. ,"Materials Science – Advanced Topics: Chapter 4: Plasma Electrolytic Oxidation of Valve Metals", InTech Publishing (2013)
61. Choo, Yoon H., and Owen F. Devereux. "Barrier-Type Aluminum Oxide Films Formed under Prolonged Anodizing I. Influence of Anodizing Parameters on Film Morphology." Journal of the Electrochemical Society 122.12 (1975): 1645-1653.
62. Fratila-Apachitei, L. E., et al. "Influence of Substrate Microstructure on the Growth of Anodic Oxide Layers." Electrochimica acta 49.7 (2004): 1127-1140.
63. G. Höhne, W. Hemminger, H. Flammersheim, "Differential Scanning Calorimetry; 2nd Edition", Springer-Veriag Berlin Heidelberg (2003)
64. M. Brown, "Introduction to Thermal Analysis; Techniques and Applications", Kluwer Academic Publishers, (1988)
65. D. Porter, K. Easterling, "Phase Transformations in Metals and Alloys", CRC Press (2004).
66. W. Boettinger, U. Kattner, K. Moon, J. Perepezko "DTA and Heat-flux DSC Measurements of Alloy Melting and Freezing", National Institute of Standards and Technology (2006)
67. Corbin, Stephen Francis, et al. " Analysis of Fluxless, Reactive Brazing of Al Alloys Using Differential Scanning Calorimetry" Metallurgical and Materials Transactions A: 1-9 (2014)
68. Netzsch-Gerätebau GmbH. (2013), "DSC 404 F1/F3 Pegasus: Analyzing and Testing", www.netzsch-thermal-analysis.com
69. Netzsch DSC 404c-Pegasus: Instrument manual: Operating Instructions for DSC Apparatus (1998).

70. Kuntz, M. L., S. F. Corbin, and Y. Zhou. "Quantifying Metallurgical Interactions in Solid/Liquid Diffusion Couples Using Differential Scanning Calorimetry." Acta Materialia 53.10 (2005): 3071-3082.
71. Turriff, D.M. “Process Kinetics of Transient Liquid Phase Sintering in a Binary-Isomorphous Alloy System”, Ph.D. thesis, University of Waterloo (2006).
72. Liang, F., Dana Canada Corporation, Personal Communication, 2014.
73. Colley, L., Dana Canada Corporation, Personal Communication, 2014.
74. M. Shaarbaf, “Measurement of Oxide Thickness on Al-10%Si and Al-10%Si-0.05%Li Alloys By TEM and Electron Microprobe”, Material Characterization, 43 (1999) 279-284.
75. Grosskreutz, J. C. "Mechanical Properties of Metal Oxide Films." Journal of the Electrochemical Society 116.9 (1969): 1232-1237.
76. Evans, H. E. "Cracking and Spalling of Protective Oxide Layers." Materials Science and Engineering: A 120 (1989): 139-146.
77. Specs GmbH, “Useful Information and Facts about the Practice of Sputtering”, http://www.specs.de/cms/upload/PDFs/IQE11-35/sputter-info.pdf, (2000)

APPENDIX A: Associated Phase Diagrams for Ni-Modified Al Braze Sheets

A proper understanding of constituent behavior within the aluminum alloy and on its surface was important in understanding resultant reactants and microstructures. Included in this appendix are the binary phase diagrams for Al-Si, Al-Mg, and Al-Ni systems which were the primary constituents examined. Al-Fe and Al-Mn systems showed to be rather inert or so low in concentration that they were excluded from this section, aside from the importance of manganese in resultant brazed microstructures (see section 2.2.5) [28].

The impact of each constituent is discussed fully in section 2.2. The binary phase diagrams retrieved from the ASM Phase Handbook are included below as Figures A-1, A-2, and A-3.

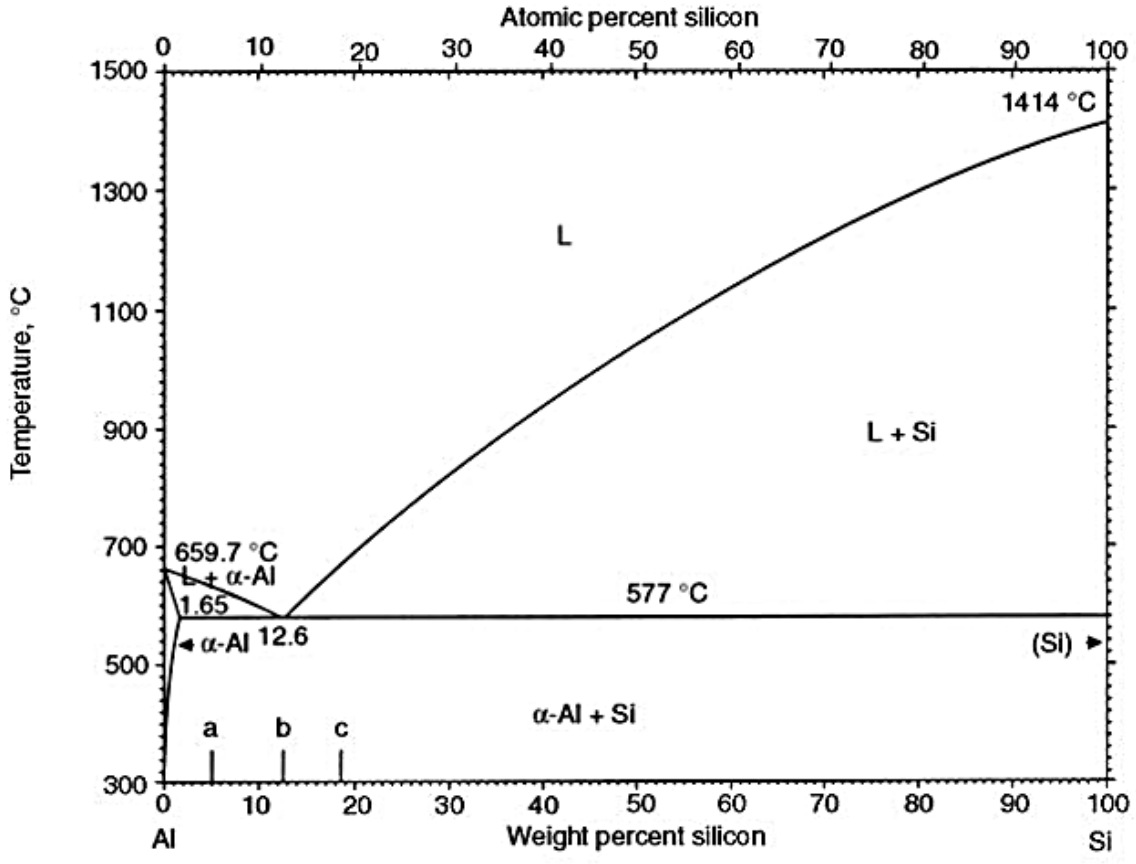

Figure A-1 – Al-SI Binary Phase Diagram [28]

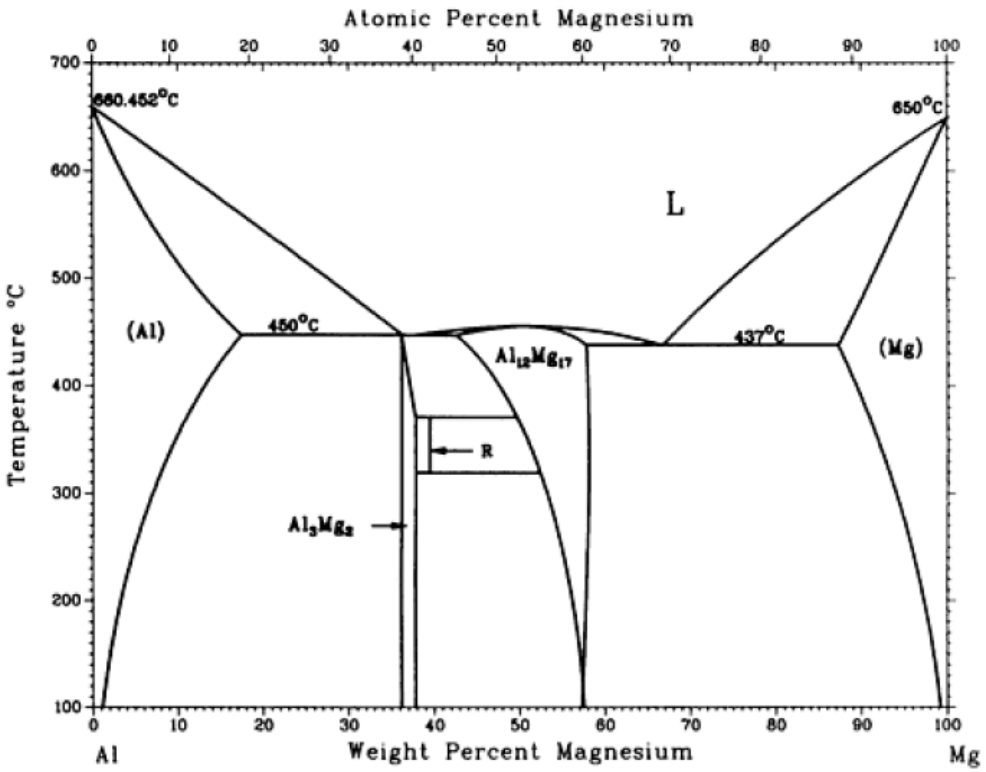

Figure A-2 – Al-Mg Binary Phase Diagram [28]

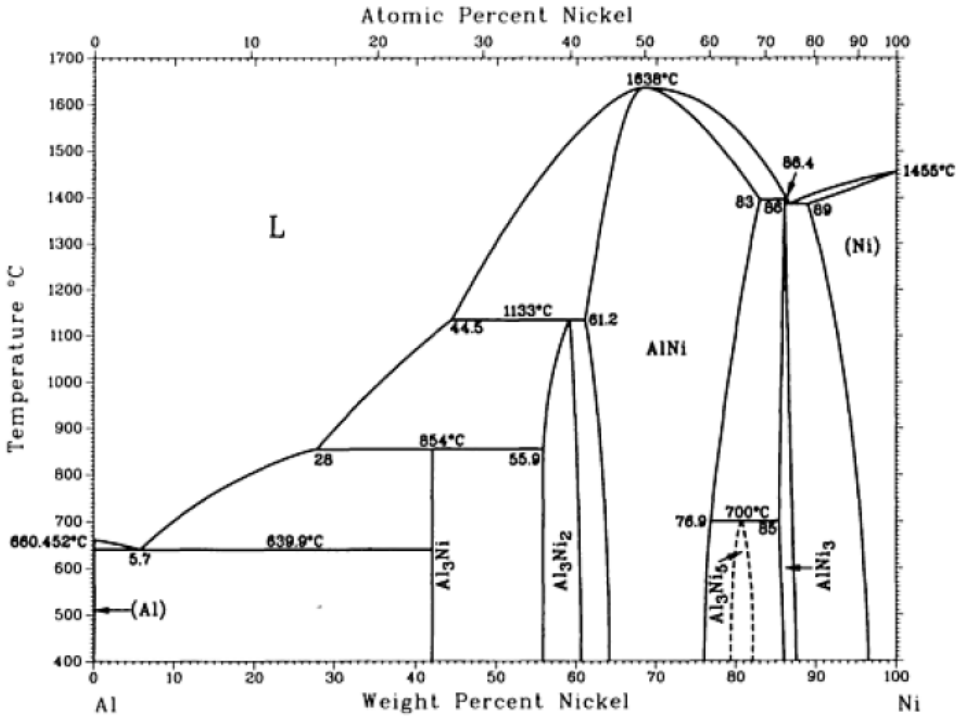

Figure A-3 – Al-Ni Binary Phase Diagram [28]

APPENDIX B: Resultant Microstructures of Ni-Modified Braze Sheets at Different Isothermal Hold Times

Corbin et. al experimented with the effect of nickel thickness and different isothermal hold times to document the nickel reaction during melting (570°C) and after (590°C). The results are shown in Figure B-1. It was found that increasing nickel thickness lead to a greater disruption on the surface which could be seen by the increase in volume fraction of Al_3Ni. Samples with 2 wt% Ni brought to 570°C showed Al_3Ni embedded much further into the resolidified clad. It was found that the amount of nickel present on the surface had less importance following a complete melting event at 590°C than when interrupted at 570°C [67].

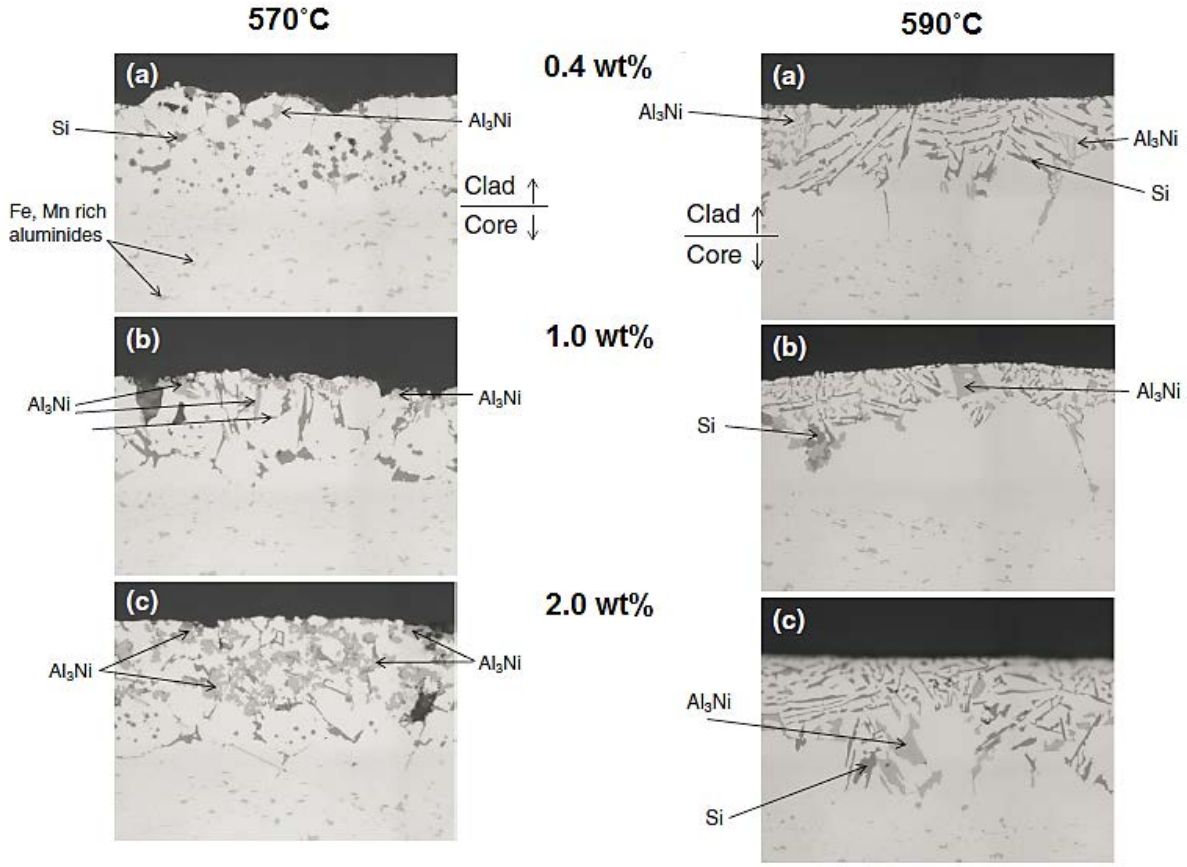

Figure B-1 – Microstructures of Different Nickel Thicknesses at 570°C and 590°C [67]

APPENDIX C: Schematic of DSC Interior

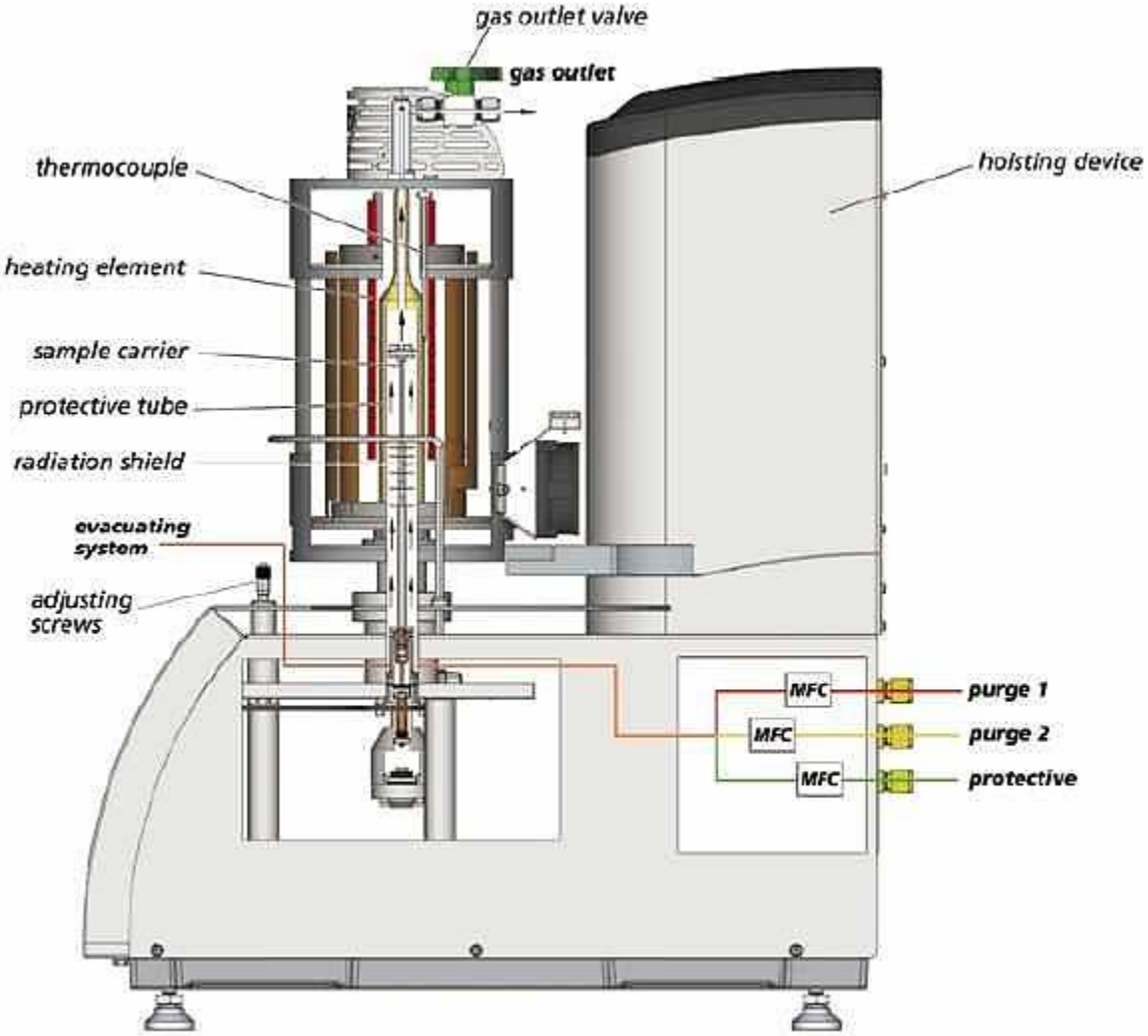

Figure C-1 – Schematic of DSC Interior [68]

APPENDIX D: Initial SEM-EDX Measurements of Oxide Growth Experiments

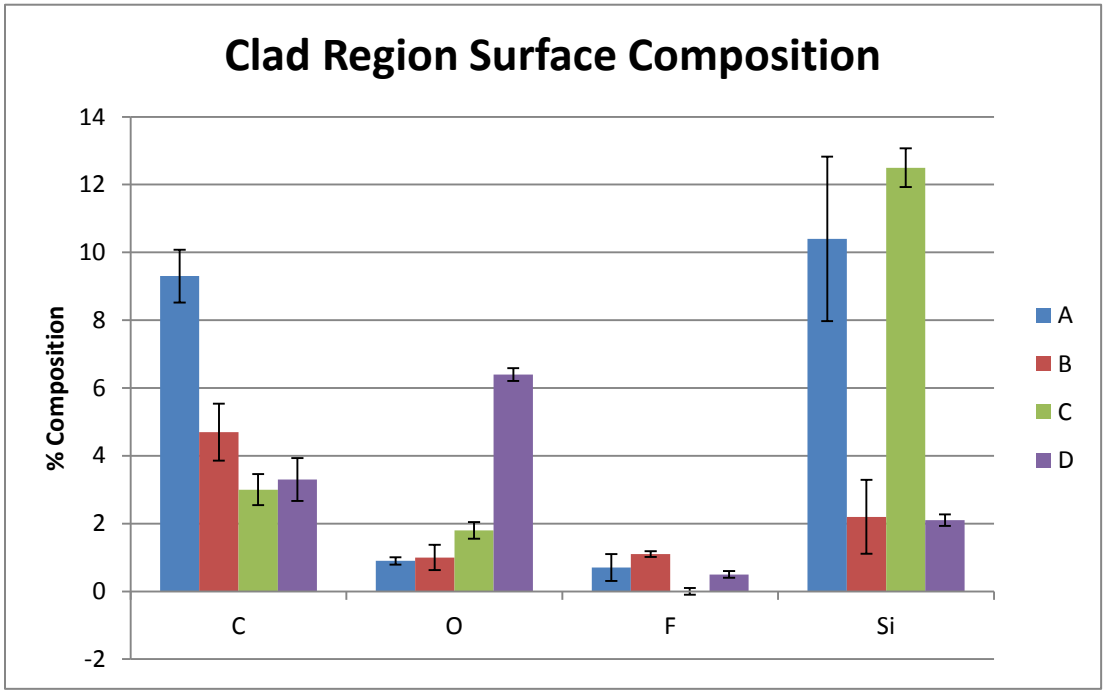

APPENDIX E: FIB-SEM Measurements of Surface Modified Aluminum Alloy Samples

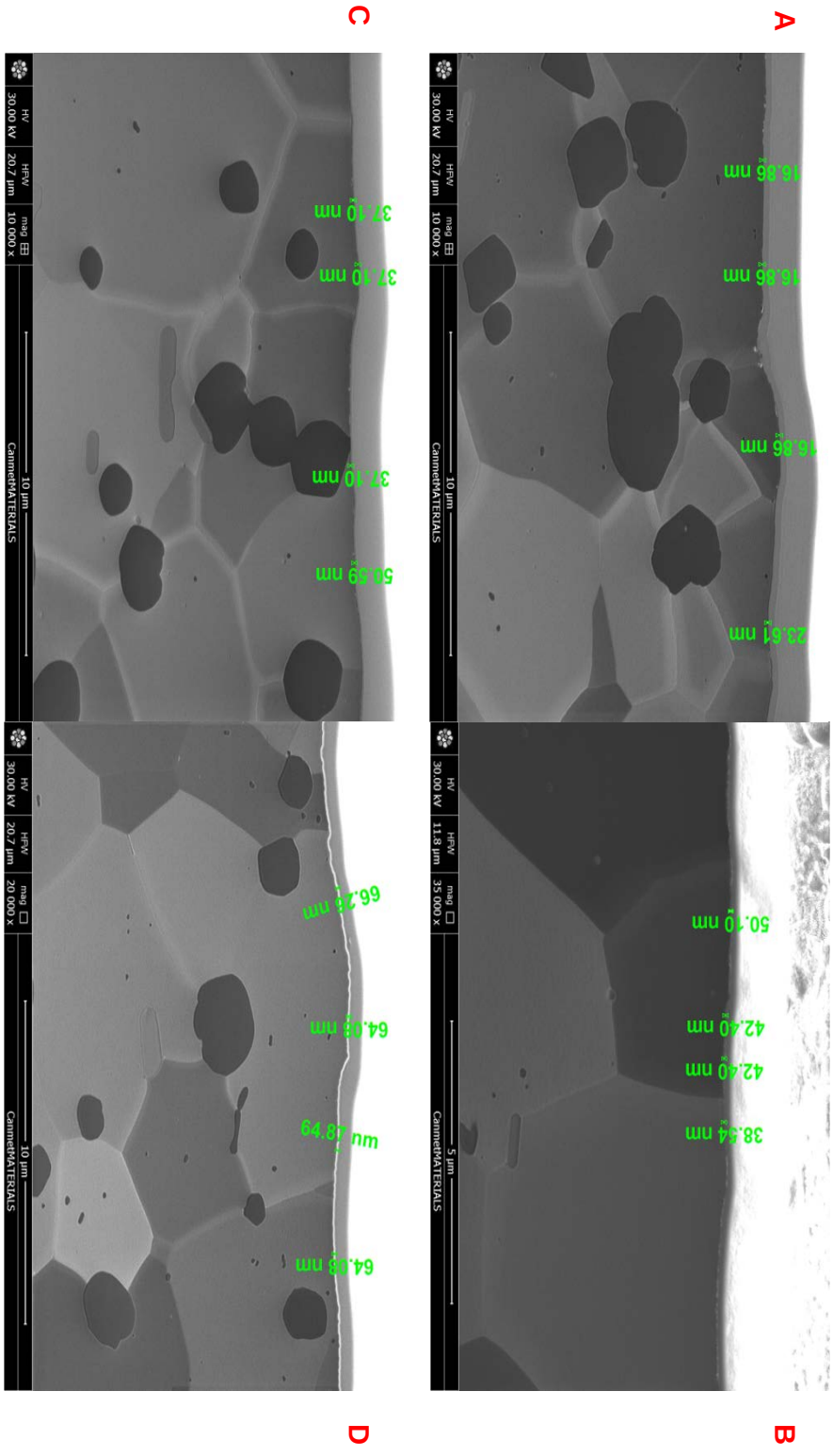

APPENDIX F: Measurement of Sputtered Surface Modified Aluminum Alloy Samples

Following profilometer measurement of sputtered samples, cross sectional imaging of samples were examined under SEM. A JEOL 6460 scanning electron microscope (SEM) was used for high magnification metallographic examination of specimens. A 20kV electron gun acceleration voltage was used. Secondary electron (SE) imaging was used to interpret the morphology and topographical contrast of the sections. Samples were examined under three different magnifications and a conversion factor was created using ImagePro later. The sputtered nickel layer was measured ten times on three of the same type of sample, for example Sample 1. The averages and standard deviations (in µm), as well as scale bar conversion factors, are included in Table F-1.

Table F-1 - SEM Measurement of Sputtered Nickel Thicknesses

	7000X	18000X	35000X
Scale Bar			
pixels	70	90	88
microns	2	1	0.5
Sample 1			
Average	0.240	0.221	-
Standard Dev.	0.022	0.065	-
Sample 2			
Average	0.500	0.478	-
Standard Dev.	0.025	0.011	-
Sample 3			
Average	-	1.513	1.342
Standard Dev.	-	0.314	0.340

APPENDIX G: Cyclical DSC Test Results for Oxide Disruption

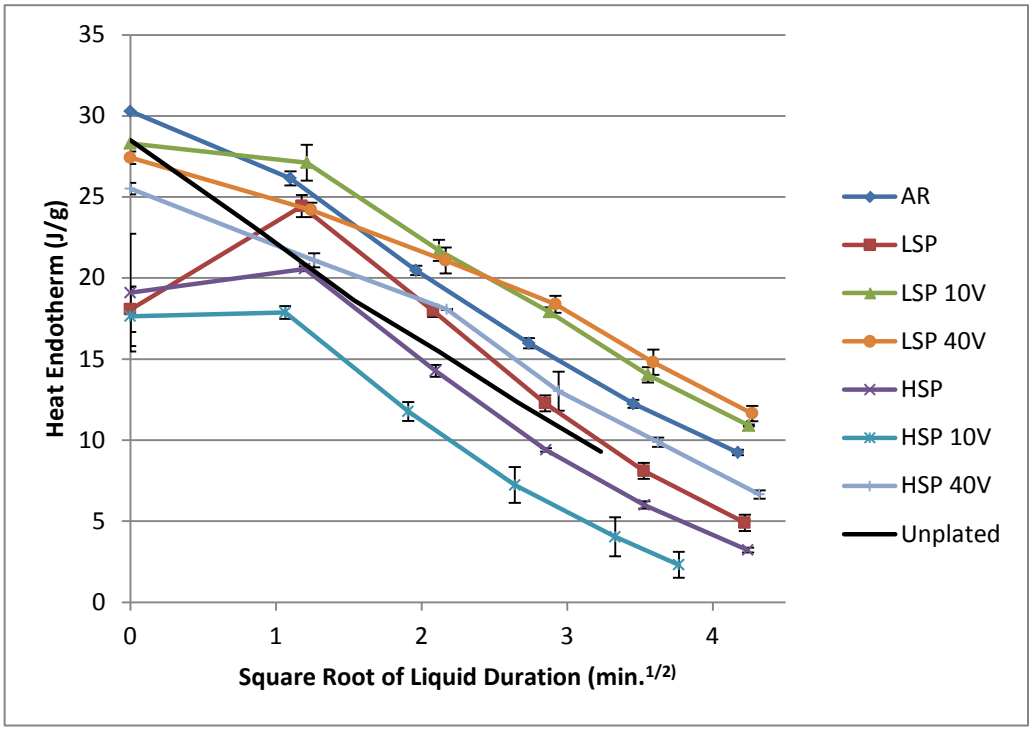

Figure H-1 – Square Root of Liquid Duration of Oxide Disruption Samples with 0.5um Nickel

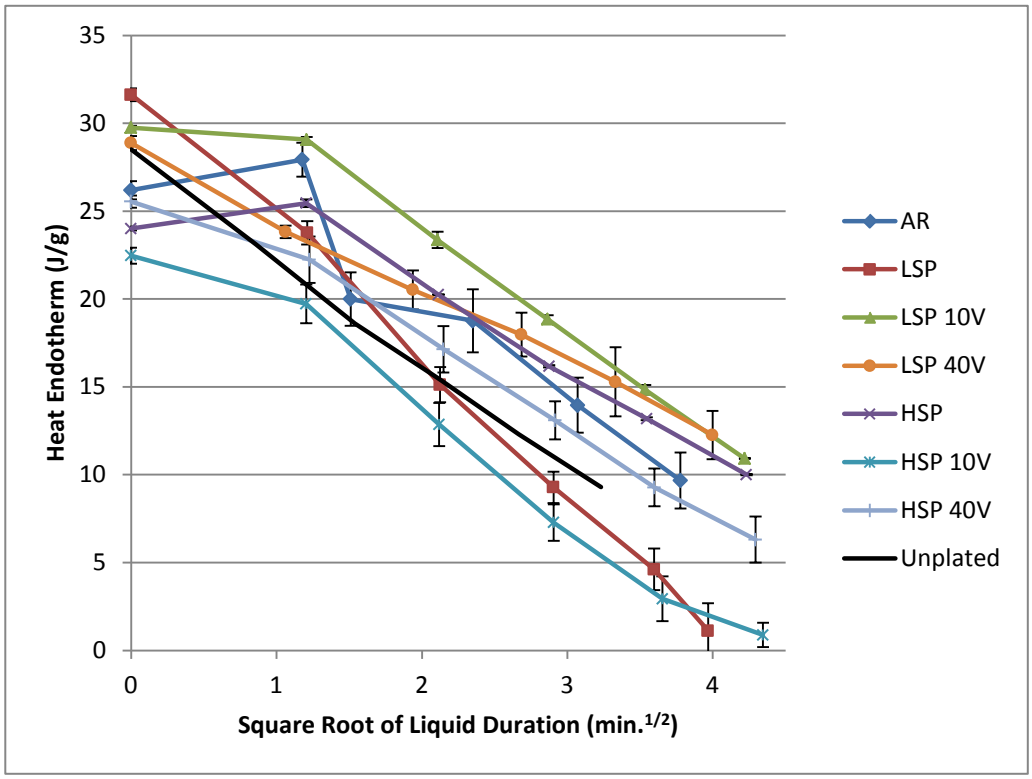

Figure H-2 – Square Root of Liquid Duration of Oxide Disruption Samples with 0.25um Nickel

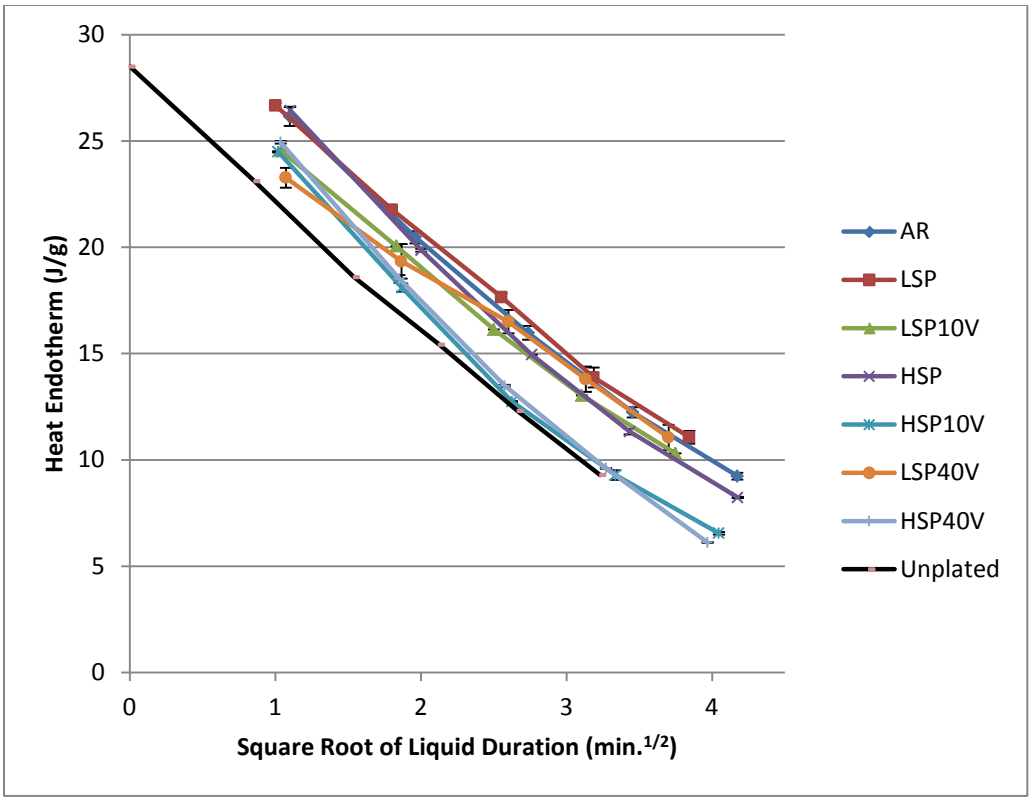

Figure H-3 - Square Root of Liquid Duration of Oxide Disruption Samples with 0.1um Nickel